

Mass Distribution at the Galactic Centre

Inaugural-Dissertation

zur

Erlangung des Doktorgrades
der Mathematisch-Naturwissenschaftlichen Fakultät
der Universität zu Köln

vorgelegt von

Nelly Mouawad

aus Beirut (Libanon)

Köln 2005

Berichterstatter:

Prof. Dr. A. Eckart

Prof. Dr. M. Abd-Elmeguid

Tag der letzten mündlichen Prüfung:

Montag 20 Juni 2005

Contents

1	Introduction	13
1.1	The Complexity of the Central Cluster's Components	14
1.2	Dynamics of the Central Cluster	16
1.2.1	Density distribution of the central stellar cluster	16
1.2.2	Stellar orbits - star S2	17
1.2.3	The dark central mass	18
2	Observational Techniques	21
2.1	Instruments	21
2.1.1	The SHARP/NTT Camera	21
2.1.2	Gemini imaging Data	23
2.1.3	The NAOS/CONICA Camera	23
2.1.4	The AO system on NAOS/CONICA	24
2.2	Brief Results Obtained by SHARP and NACO on the GC	25
2.3	Astrometry	26
2.3.1	Use of the SiO masers to establish an astrometric reference frame	26
2.3.2	Main observing results with NAOS/CONICA	29
3	The Centre of the Milky Way	31
3.1	The Interstellar Medium	31
3.2	The Nuclear Stellar Cluster	32
3.2.1	Embedded objects	35
3.2.2	IR-Excess objects	37
3.2.3	Fast moving stars : The S-stars.	39
3.3	Sagittarius A*	41
4	Density and Mass distribution	45
4.1	Number Density Counts	45
4.2	Enclosed Mass	49
4.2.1	Mass estimators	49
5	A High Accuracy Integrator	55
5.1	The Hermite Integrator: An individual timestep scheme	55

5.1.1	Algorithmic aspects	56
5.1.2	Computational aspects	56
5.2	Development of the Code	58
6	Modelling of the S2 Orbit	61
6.1	Keplerian and Non-Keplerian Orbits	61
6.1.1	Kepler's laws	61
6.1.2	Non-Keplerian motion	62
6.1.3	Orbital elements	63
6.1.4	Determination of orbital elements from positions and velocities	65
6.2	The Method	66
6.2.1	χ^2 minimization scheme	67
6.2.2	A χ^2 criterium	68
6.2.3	Influence of model parameters	68
7	Stellar Orbits	71
7.1	Results on Keplerian Orbits	73
7.2	Results on Non-Keplerian Orbits	75
7.3	Influence of Mass Distribution and Cusp Size	78
7.3.1	Power-Law mass distribution	78
7.3.2	Core Radius of the 'inner cusp'	81
7.4	Relativistic Prograde Peri-astron-shift	81
7.5	Conclusion and Outlook	82
8	Analysis	85
8.1	The K-Luminosity Function	85
8.1.1	Stability of a cluster of low-mass Stars	89
8.2	Is the Cusp Dominated by Dark and Massive Objects?	89
8.2.1	Stability of a cluster of stellar remnants	92
8.2.2	Stability of a cluster of intermediate mass black holes	93
8.3	Brownian Motions of the SMBH	94
8.4	Comparison with Observational Results	95
9	Summary	97
A	List of Abbreviations/Orbital Parameters	101
A.1	List of Abbreviations	101
A.2	Orbital Parameters	101
B	De-projection of the K-band Luminosity Function	105
C	K-band magnitude/Stellar masses	107

List of Figures

1.1	H/Ks/L' three-colour composite of the central $\sim 20''$	14
1.2	Surface mass density fit to number density counts	16
1.3	Keplerian Orbits of 6 S-stars	18
1.4	Superposition of Keplerian and non-Keplerian Orbits of the Star S2	20
2.1	Quality of speckle images	22
2.2	Quality of adaptive optics images	25
2.3	NACO GC K-band image	28
3.1	Ks image of the central $\sim 20''$	33
3.2	Optical depth at the $3.4\mu\text{m}$ versus the $3.48\mu\text{m}$ absorption feature.	36
3.3	Optical depth at the $3.4\mu\text{m}$ versus the $3.0\mu\text{m}$ absorption feature.	36
3.4	ISAAC L-band map combined with the spectra of the central sources	37
3.5	H, Ks, and L' band images of the IRS 13/IRS 2 region	38
3.6	NACO and SINFONI H/K-images of the Sgr A* Cluster - The S-stars	40
3.7	Infrared variability of SgrA*	42
4.1	Surface density of stars vs. distance from Sgr A*	47
4.2	Mass distribution in the central 10 pc of the Galactic Centre	52
6.1	Rosetta-shift orbit	63
6.2	Orbital elements in space	64
6.3	Positions of the central mass	70
7.1	Superposition of two best fitting orbits	72
7.2	Reduced $\tilde{\chi}^2_{tot}$ values vs. separation from the <i>offset</i> position	73
7.3	Three exemplary orbits determined by our fitting	75
7.4	Table of $\tilde{\chi}^2_{tot}$ values	76
7.5	$\tilde{\chi}^2_{tot}$ values vs. the total central mass	77
7.6	Exemplary three non-fitting orbits	78
7.7	Orbits in Power-law and Plummer potentials.	79
7.8	Orbital shifts as a function of R_1	80
8.1	K-band Luminosity Function of the central cusp region	86
8.2	Influence of the M/L on the mass distribution.	90

8.3	Motion of Sgr A* due to gravitational forces of random stellar orbits	94
-----	---	----

List of Tables

2.1	Positions and proper motions of SiO masers within of 15'' of Sgr A*	27
4.1	Parameters of the 'composite model'	48
6.1	Characteristic $\tilde{\chi}^2_{tot}$ of the orbital fits	68
7.1	The lowest obtained $\tilde{\chi}^2_{tot}$ values	74
7.2	Cusp Mass for different $\tilde{\chi}^2_{tot}$ values	83
8.1	Characteristic of a hypothetical inner cluster of main sequence stars	87
8.2	Estimated masses of different stellar types	88
8.3	Mass-to-Light ratios for different cusp mass values	89
A.1	Orbital parameters I	102
A.2	Orbital Parameters II	103
C.1	Stellar masses corresponding to K magnitudes	108

Zusammenfassung

Im Rahmen dieser Doktorarbeit wird die Verteilung ausgedehnter Masse nahe dem supermassiven Schwarzen Loch (SMBH) im Zentrum unserer Galaxie mit Hilfe von Beobachtungsdaten und theoretischer Modellierung untersucht. Der Schwerpunkt liegt auf der Ausarbeitung einer Unterscheidung zwischen dem Anteil der dunklen Masse, der in Form des Schwarzen Loches vorliegt, und dem Anteil, der in ausgedehnter Form existiert. Obwohl Beobachtungen und theoretische Studien in den letzten zehn Jahren einen bedeutenden Fortschritt bezüglich des Verständnisses Schwarzer Löcher gebracht haben, wirft die Entstehung Schwarzer Löcher und ihre Wechselwirkung mit der Wirtsgalaxie noch immer viele Fragen auf. Die hier durchgeführte Arbeit vertieft unser Verständnis der Dynamik in der Nachbarschaft des SMBH. Bereits 1974 wurde vorgeschlagen, dass es sich bei der Radioquelle Sgr A* um ein SMBH handeln könnte. Seitdem haben Beobachtungen gezeigt, dass unsere Galaxie eine dunkle Masse von $\sim 3 \times 10^6 M_{\odot}$ im Zentrum verbirgt. Der bisher stärkste Beweis für die Existenz eines SMBH ergab sich, als es zum ersten Mal möglich wurde, die Bahnen schnell Sgr A* umlaufender Sterne (die sogenannten S-Sterne) zu verfolgen. Dies wurde erreichbar durch neue Instrumente, wie die Nahinfrarot-Speckle-Kamera SHARP auf La Silla in Chile, sowie die Nahinfrarot-Kamera NAOS/CONICA am Very Large Telescope (VLT) auf Paranal in Chile. In Zusammenarbeit mit der Nahinfrarot-Gruppe am Max-Planck-Institut für Extraterrestrische Physik in Garching bei München, benutze ich die bildgebenden Daten vom Galaktischen Zentrum, um die Sternverteilung zu untersuchen, und die Daten über Eigenbewegungen und Radialgeschwindigkeiten, um die Bewegung der S-Sterne zu studieren.

In der hier vorgestellten Analyse der Massenverteilung um das Schwarze Loch werden Sternbahnen modelliert, indem zusätzlich zum Potenzial des Schwarzen Loches ein Potenzial ausgedehnter Masse vorausgesetzt wird. Ich untersuche die Sternbahnen sowohl in keplerschen als auch in nicht-keplerschen Potenzialen. Dies ist *die erste Studie dieser Art*, die Beobachtungsdaten mit theoretischer Modellierung verbindet. Auch zeigt diese Arbeit das erste Mal einen Ansatz, in dem das Masse-Leuchtkraft-Verhältnis (M/L) von den äußeren zu den inneren Regionen variiert. Basierend auf früheren dynamischen Studien zu Galaxienentwicklung wird üblicherweise angenommen, dass das M/L zu den inneren Regionen einer Galaxie hin zunimmt. Dies impliziert, dass eine zusätzliche Menge verborgener Masse nahe dem Zentrum existieren könnte. In dieser Doktorarbeit untersuche ich explizit mögliche Kandidaten für diese verborgene Komponente - schwache massearme Sterne und schwerere kompakte Sternüberreste. In der Praxis ist eine sinnvolle Analyse nur für den Stern S2 möglich, der die kürzeste Bahnperiode und damit die vollständigste Bahn aller S-Sterne aufweist. Ein Hermite-Integrator vierter Ordnung, den ich für diese Studie optimiert habe, wird benutzt, um die S2-Bahn zu modellieren. Eine Gittermethode ist in das Hermite-Schema implementiert worden, um die Positions- und Geschwindigkeitsdaten für die S2-Bahn aus den Jahren 1992 bis 2003 anzupassen. Es ist mir möglich, die Position des Schwarzloch-Kandidaten Sgr A* zu bestätigen. Darüber hinaus kann ich eine obere Grenze für die Gesamtmasse in den zentralen 20 mpc bestimmen. Aus diesen Werten kann eine obere Grenze für das M/L abgeleitet werden. Die Arbeit führt zu dem Ergebnis, dass die gesamte dunkle Masse im Zentrum nicht notwendigerweise

gänzlich auf ein SMBH beschränkt ist. Ein Bruchteil $\lesssim 20\%$ dieser Masse könnte in einer ausgedehnten Verteilung vorhanden sein. Erprobung mehrerer Verteilungen für diese ausgedehnte Massenkomponekte zeigt, dass die vorhandenen Daten nicht ausreichen, um zwischen den verschiedenen Potenzialen zu unterscheiden.

Um die Bestandteile der möglicherweise ausgedehnten dunklen Komponente zu analysieren, untersuche ich die K-Band Leuchtkraftfunktion (KLF) des beobachteten Sternhaufens. Es ergibt sich, dass die ausgedehnte Massenkomponekte nicht nur aus schwachen massearmen Sternen zusammengesetzt sein kann. Stellare Schwarze Löcher und Neutronensterne sind notwendig, um den möglicherweise ausgedehnten Massenanteil zu erklären. Solch ein Haufen aus Sternüberresten erweist sich in einer näherungsweise analytischen Studie als stabil.

Abstract

In the framework of this PhD thesis, the study of the distribution of an extended mass close to the super-massive black hole (SMBH) at the centre of our Galaxy is addressed using observational data and theoretical modelling. The main emphasize is on establishing a distinction between the fraction of dark mass present in the form of a black hole and that in an extended form. Despite the significant observational and theoretical progress in the understanding of SMBHs in the last ten years, the formation of SMBHs and the interplay with their host galaxy are still poorly understood. The work presented here extends our understanding of the dynamics in the vicinity of the SMBH. Already in 1974, it was proposed that the radio source Sgr A* could be a SMBH. With observations during the following years, it became more clear that the centre of our Galaxy hides an amount of dark mass close to $3 \times 10^6 M_{\odot}$. However, the strongest evidence for the existence of a SMBH, was only after it became possible to trace for the first time stellar orbits of fast moving stars, the so-called S-stars, around Sgr A*. This was achievable using the SHARP near-infrared speckle camera at la Silla in Chile as well as the near-infrared camera NAOS/CONICA at the Very Large Telescope (VLT) at Paranal in Chile. In collaboration with the near-infrared group at the Max-Planck-Institut for Extra-terrestrial Physics in Garching by Munich, I used the imaging data on the Galactic Centre to study the stellar distribution, and used proper motion and radial velocity data to study the motion of the S-stars at the Galactic Centre.

In order to investigate the distribution of mass around the black hole, in this work, stellar orbits are modelled assuming an extended mass potential, in addition to the potential of the black hole. I study the orbits in both Keplerian and non-Keplerian potentials. This is *the first study of this kind* combining observational data and theoretical modelling.

This work shows also the first approach where the mass-to-light ratio (M/L) is considered to be varying from the outer regions to the inner regions of the galaxy. From earlier dynamical studies on galaxy evolution, it is widely agreed upon the M/L increasing in the inner regions of a galaxy. This implies that there could exist an additional quantity of hidden mass close to the centre. Here, I study explicitly possible candidates for this hidden component - faint, low-mass stars and heavier compact remnants.

In practice, meaningful analysis is only possible on the star S2 which shows the shortest orbital period and therefore the most complete orbit of all other S-stars. A 4th-order Hermite integrator, which I optimized for this study, is used to model the S2-orbit in response to the SMBH potential as well as an additional extended mass distribution. A grid method is implemented to the Hermite scheme to fit the S2 orbit to the positional and velocity data available from the year 1992 till 2003. I was able to confirm the position of the black hole candidate Sgr A*, to determine an upper limit on the total amount of mass that could be present in the central 20 mpc and extended into the outer regions of the central stellar cluster, as well as to deduce an upper limit on the M/L . This work leads to the results that the total central dark mass is not necessarily confined entirely in a SMBH. A fraction $\lesssim 20\%$ of this mass could be present in an extended distribution. Testing different distributions for this extended mass component, it turned out that the present data do not suffice to discriminate between the different potentials.

In order to study the constituents of the possible extended dark component, I investigate

the K-band luminosity function (KLF) of the observed stellar cluster. The result is that, the extended mass cannot be formed only by faint, low-mass stars. The presence of stellar black holes and neutron stars is required in order to account for the possible extended mass fraction in the centre of the Milky Way. Furthermore, such a cluster of stellar remnants analysed in an approximative analytical form, is found to be stable.

Chapter 1

Introduction

Over the last decade, evidence has built up for the existence of massive black holes (MBH) in the centres of many nearby galaxies. With increasing observational data - 12 MBHs candidates detected until 1995 (Kormendy & Richstone 1995), and more than 37 until 2001 (Kormendy 2001, Ferrarese et al. 2001) - it is argued that most galaxies harbour nuclei dominated by MBHs with masses that range between 10^6 and $10^{9.5}$ solar masses.

Located at a distance of only 8 kpc from the solar system (Reid 1993; Eisenhauer 2003), the Galactic Centre (GC) is the closest available galactic nucleus and therefore best observable object for investigating physical processes in the galactic nucleus of a typical spiral galaxy. It offers a unique "laboratory" for studying stars and gas in the direct vicinity of a super-massive black hole (SMBH) (e.g., Genzel, Hollenbach, & Townes 1994; Morris & Serabyn 1996; Mezger, Duschl, & Zylka 1996; Melia & Falcke 2001), with a degree of detail that cannot be accessed in any other galactic nucleus in the foreseeable future (one arcsecond corresponds to only ~ 0.04 pc). Thus, developing a consistent theoretical picture of the phenomena which are observed there improves not only our understanding of the Galaxy, but also our view of galactic nuclei in general. With the now available high sensitivity and angular resolution, large ground-based telescopes offer the opportunity to obtain an unprecedented view of the Galactic Centre. Initially, with speckle imaging techniques and lately with adaptive optics techniques, high angular resolution images on the Galaxy's central cluster have been obtained. For example, the GC is now known to harbour by far the most evident condensation of dark mass, which is apparently coincident with the radio source Sgr A* (Lo 1985). An overwhelming number of observations were successful in measuring stellar motions on the plane of the sky, yielding estimates of the projected velocities (Eckart & Genzel 1996; Ghez et al. 1998), projected accelerations (Ghez et al. 2000; Eckart et al. 2002a), and three-dimensional orbital motions (Schödel et al. 2002, 2003; Ghez et al. 2003). Each of these steps provided a successively stronger case for a SMBH of $3 - 4 \times 10^6 M_{\odot}$ at the centre of the Milky Way and its association with the unusual radio source Sgr A*. Because of these unique observations and the proximity of Sgr A*, the SMBH paradigm for galactic cores may be strengthened or refuted based on what we learn about the GC.

The region bounded by the inner few parsecs at the GC contains six principal components that coexist with the central deep gravitational potential well of the Milky Way. Apart from

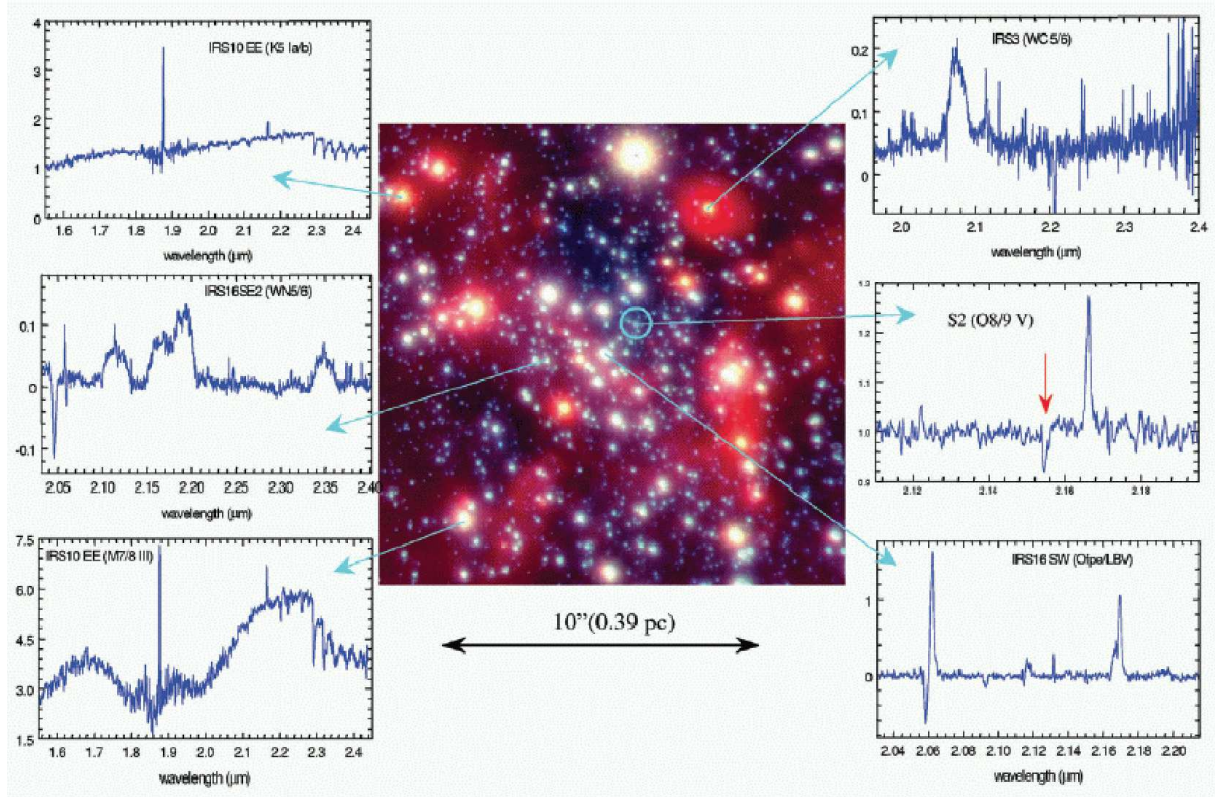


Figure 1.1: **H/Ks/L' three-colour composite of the central $\sim 20''$.** Spectra obtained with an integral field spectrometer (Spiffi, Horrobin et al. 2004), superposed on a NACO H/K/L' colour composite image of the central region. The spectra display the wide range of stellar types found in the cluster, ranging from main sequence O stars (the star S2 near Sgr A*, oval in image), to the luminous blue variables (IRS 16 SW, lower right), early WN (middle left and WC (top right) Wolf-Rayet stars, to red supergiants (the brightest star IRS 7 at the top/middle of the image), bright asymptotic giant branch stars (IRS 9, lower left) and red giants (IRS 10 EE, top left).

the SMBH, these are the surrounding cluster of evolved and young stars known as the central stellar cluster, a molecular dusty ring, ionized gas streamers forming the so-called mini-spiral, diffuse hot gas, and a powerful supernova-like remnant. Many of these phenomena occurring in this complex and unique portion can be explained by the interaction of these components. In chapter 3, I give a detailed explanation of these components, in the following, I only cite the most important phenomena for a consistent introduction of this work.

1.1 The Complexity of the Central Cluster's Components

Infrared imaging and spectroscopy, initially using 4 m class telescopes (Krabbe et al. 1995; Genzel et al. 1996, 1997; Eckart et al. 1995, 1997b, 2000) have yielded a wealth of information on the stellar content inside distances of ~ 1 pc from the super-massive black hole at the Galactic

Centre. This situation has now improved with observations using 10 meter class telescopes, including the Very Large Telescope (VLT) and the W. M. Keck Observatory (Ghez et al. 1998; Gezari et al. 2002; Hornstein et al. 2002; Figier et al. 2003; Genzel et al. 2003; Ghez et al. 2003; Schödel et al. 2003, Eisenhauer et al. 2005, submitted). The black hole is located at the centre of a compact stellar cluster that has been the target of observational surveys for more than a decade (e.g., Krabbe et al. 1995; Figier et al. 2000; Gezari et al. 2002). The stellar cluster in the central parsec has been found to be very complex. It contains several different stellar populations/components (for a review see Genzel 2001). Fig 1.1 shows the diversity of these components. The stellar mass is dominated by an old population of red giants (1 - 10 Gyr), there are indications that the observed giants are limited to the region outside the central ~ 0.5 pc (Eckart et al. 1995, Figier et al. 2003). There exists also a bright ($K \sim 9 - 12$) population of massive blue stars, the HeI emission-line stars; also, a number of bright ($K \sim 10 - 12$) late-type stars classified as asymptotic giant branch stars which belong to an intermediate-mass, intermediate-age stellar population. There is as well a group of dust-embedded stars with nearly featureless near-IR spectra (Becklin et al. 1978; Krabbe et al. 1995; Genzel et al. 1996), many of which are associated with the gaseous mini-spiral (Lo & Claussen 1983). Finally, there exists a group of very intriguing objects at projected distances as close as $1.2''$ from Sgr A*, they form more than one dozen of young O/B (Eisenhauer et al. 2005, submitted) main sequence stars, designated by the Sgr A* cluster. These are fast moving stars, with already observed accelerations, of which the shortest orbital period is of ~ 15 years (Schödel et al. 2002, 2003; Ghez et al. 2003). This group of stars denoted by the 'S-stars' will occupy the central theme of this work.

Each of these stellar components forms an enigmatic part of the GC. A picture is emerging in which the brightest stars in the Sgr A* cluster (≤ 0.03 pc) are young, main-sequence stars with apparent magnitudes $K \geq 14$ and masses $10 - 20M_{\odot}$. The early-type stars outside 0.03 pc appear to be spectroscopically and kinematically distinct. They span a larger range of magnitudes $K \geq 10$ and contain ~ 40 mass-losing lower luminosities Wolf-Rayet stars (Genzel et al. 2003, Paumard et al. 2003, Horrobin et al. 2004, Moultaqa et al 2004). The formation of the observed young stars, with 100 times larger specific binding energies relative to the black hole than that of the nearest observed accumulation of molecular gas (e.g., Jackson et al. 1993) presents a challenge to star formation theories and is a persistent puzzle (e.g., Morris 1993; Ghez et al. 2003). A number of mechanisms for the formation and migration of stars in the tidal field of the massive black hole have been proposed (Gerhard 2001; Gould & Quillen 2003; Hansen & Milosavljevic 2003; Levin & Beloborodov 2003, Levin et al. 2005; Kim & Morris 2003; Milosavljevic & Loeb 2004). While the mechanisms have important implications, they are also each deficient in at least one way.

Among the dust-embedded objects present in the central cluster, some objects were studied by Eckart et al. (2004) and Moultaqa et al. (2004), a description of both works to which I contributed is given in chapter 3. With NIR imaging and spectroscopy observations, Eckart et al. (2004) studied the IRS 13 complex and discovered a new small stellar cluster of compact sources located to the north of IRS 13 complex. Their nature is not clear, they may be a cluster of highly extinguished stars that interact with the local environment of the mini-spiral. Also, with NIR imaging and spectroscopy Moultaqa et al. (2004) performed observations on a group of

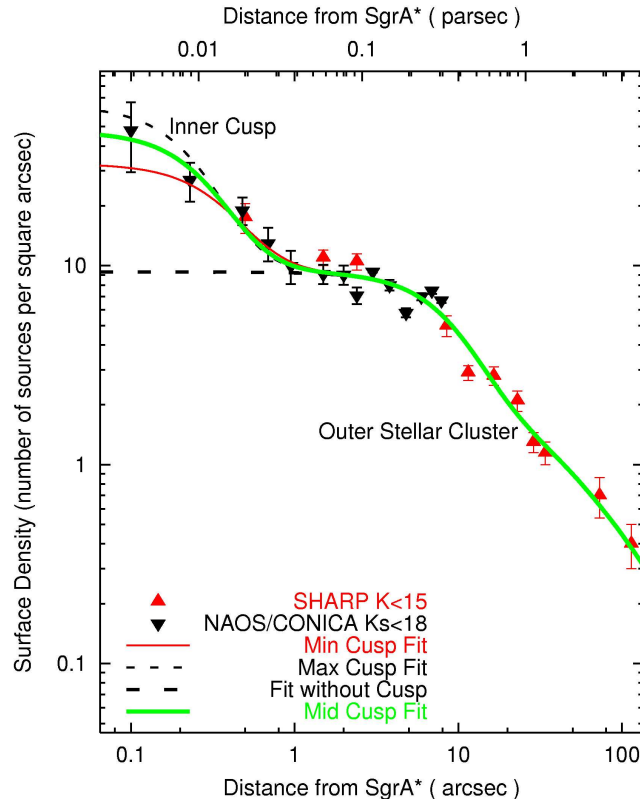


Figure 1.2: **Surface mass density fit to number density counts.** Surface density of stars vs. distance from Sgr A*. The downward pointing triangles represent the NAOS/CONICA data for $K_s \leq 17$, the upward pointing triangles are SHARP/NTT data for $K_s \leq 15$ stars scaled up by a factor of 5 in order to match the fainter NAOS/CONICA counts. The data are taken from Genzel et al. (2000, 2003). Informations on the fitting model and parameters are given in section 4.1.

dust-embedded objects bright in the 2 - 4 μm wavebands. Some sources show consistency with a massive hot star being embedded in the bow-shock created through the interstellar medium in this regions (see also Tanner et al. 2004).

1.2 Dynamics of the Central Cluster

1.2.1 Density distribution of the central stellar cluster

While the measured stellar density profile of the Galactic bulge is consistent with that of a singular isothermal sphere (Sanders & Lowinger 1972), the profile in the central parsec is not well known, especially for the lower-mass stellar population. Within a radius of 10'', the surface brightness continues to increase inward to 1'', but the stellar surface number density at moderately bright magnitudes ($K \leq 15$) flattens out, consistent with a half-peak surface brightness/density (core) radius of $\sim 0.34 \pm 0.2$ pc (Genzel et al. 1996).

Assuming relaxation that is driven by two-body processes, Bahcall & Wolf (1976) showed

that the equilibrium phase space distribution for a population of equal mass stars surrounding a black hole that dominates the gravitational potential is a power law in density $\rho \propto r^{-7/4}$. For a multimass distribution the lighter stars are less centrally concentrated, resulting in a power-law profile that ranges from $r^{-3/2}$ for the least massive species to $r^{-7/4}$ for the most (Bahcall & Wolf 1977; Murphy, Cohn, & Durisen 1991). A coeval family of stars in the central region has reached equilibrium only if it is older than the relaxation time. Since the main sequence lifetime of stars more massive than $\sim 2M_{\odot}$ is shorter than t_{rel} , young massive stars in the GC are not dynamically relaxed; their distribution is primarily a reflection of the conditions under which they formed. While lower mass dwarf stars are sufficiently old to be relaxed in the central potential, their distribution in the innermost region could be affected by an abundance of stellar mass black holes (5 - 10 M_{\odot}). As products of normal stellar evolution, stellar mass black holes sink towards the centre of the stellar cluster surrounding the massive black hole (Morris 1993; Miralda-Escudé & Gould 2000, Freitag et al. 2003) and displace the less massive stars and remnants.

In this work, it is shown that the present data on the centre of the Galaxy can be represented by a localized Plummer model-like core on Sgr A*, superposed on a larger scale, isothermal cluster with a distinct break in between (see Fig 1.2). This indicates that there could exist a compact core, which is denoted by 'inner cusp' throughout this work, of high densities very close to the super-massive black hole. In chapter 6 and chapter 7, it is shown how it is possible to study the existence of such a cusp by modelling orbits of the S-stars of which the dynamics are governed by the SMBH, but also by the potential of the 'inner-cusp'.

1.2.2 Stellar orbits - star S2

More than a decade of high-resolution infrared observations of proper motions in the GC, with the ESO New Technology Telescope (NTT) and the ESO Very Large Telescope (VLT) (Eckart & Genzel 1996; Eckart et al. 2002a; Schödel et al. 2002, 2003), as well as with the Keck telescope (Ghez et al. 1998, 2000, 2003, 2005), have provided milliarcsecond astrometry, enabling the detection of proper motions within the inner 0.5 pc and accelerated proper motions of ~ 10 stars within the inner 0.05 pc. These data have recently allowed the derivation of orbital elements of 6 stars orbiting the centre (Schödel et al. 2002, 2003, Ghez et al. 2003, Eisenhauer et al. 2005 submitted, see Fig 1.3).

A series of observations with the NAOS/CONICA adaptive optics system/near-infrared camera at the ESO VLT unit telescope 4 that covered the peri-centre passage of the star S2 around Sgr A* allowed Schödel et al. (2002) to fit a Keplerian orbit and to measure the enclosed dark mass at separations as close as ~ 0.6 mpc (~ 120 AU) from Sgr A*. With these observations, they could exclude a neutrino ball scenario (Munyanza & Viollier, 2002) as an alternative explanation for the dark mass concentration. They excluded as well a cluster of dark astrophysical objects (Maoz 1998) such as neutron stars, leaving a central super-massive black hole as the most probable explanation. Using the Keck 10 m telescope, Ghez et al. (2003) improved the Schödel et al. (2002) results and reported the first spectroscopic identification and line-of-sight velocity measurement of S2. The first detection of spectral absorption lines by Ghez et al. (2003) (both Br (2.1661 μm) and He I (2.1126 μm)), provided line-of-sight velocity

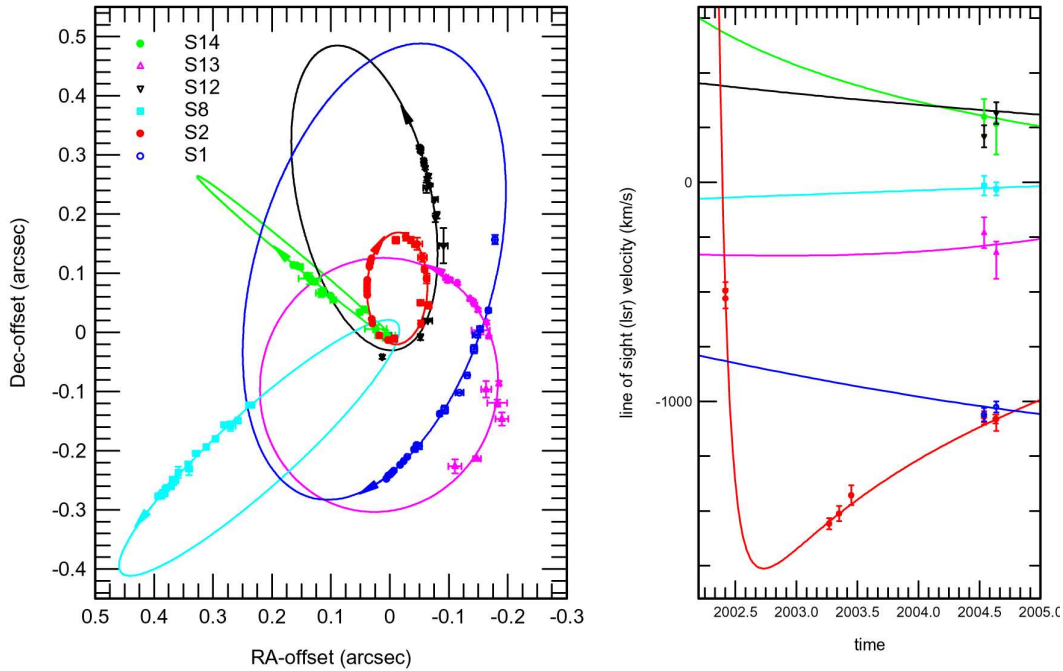


Figure 1.3: **Keplerian Orbits of 6 S-stars.** *Projection on the sky (left inset) and in time/radial velocity (right inset) of the fitted orbits of the 6 S-stars (see also Schödel et al. 2003). The various colour curves are the result of the best global fit to the spatial and radial velocity data of S1, S2, S8, S12, S13 and S14. The assumed distance is 8 kpc (Eisenhauer et al. 2005).*

measurements. These measurements resolved the ambiguity on the inclination of the S2 orbit indicating that its position was behind the black hole when it passed through the peri-centre of its orbit. In addition, stellar rotational velocities suggested that S2 is an O8-B0 dwarf star and thus a massive ($\sim 15 M_{\odot}$) young star (~ 10 Myrs) (Ghez et al. 2003, Eisenhauer et al. 2005). From data taken with NAOS/CONICA and the new NIR integral field spectrometer SPIFFI at the ESO VLT, Eisenhauer et al. (2003) reported new astrometric observations and additional spectroscopic observations of the star S2, reducing the uncertainties on the orbital parameters. They also gave the first geometrical distance measurement to the centre of the Milky Way of 7.94 ± 0.42 kpc, which is in agreement with earlier determinations (see Reid 1993).

1.2.3 The dark central mass

The relatively low intrinsic velocity (corresponding to only $\lesssim 20 \text{ km s}^{-1}$) of the radio source Sgr A*, which is located at the centre of the stellar cluster, can be explained by its physical association with a dark mass at the centre of the Milky Way (Backer & Sramek 1999; Reid et al. 1999). However, the strongest evidence so far for the existence of a massive black hole was provided by the fast orbiting, short orbital period stars. Orbital reconstruction of few of these stars in Keplerian dynamics invokes a mass of the Galactic black hole of $3 - 4 \times 10^6 M_{\odot}$.

(e.g., Eckart et al. 2002a; Ghez et al. 2003, 2005; Schödel et al. 2003; Eisenhauer et al. 2005, submitted).

Additional spectroscopic information on line-of-sight velocities allows for a precise geometric determination of the distance of Sgr A* from the solar system (Eisenhauer et al. 2003). In spite of the quality of elementary data available about the black hole and the bright stellar sources, the matter content in the vicinity of the black hole remains unknown. The observed stellar sources probably represent only a fraction of the total matter content. Close to Sgr A*, due to extreme crowding of sources, faint main-sequence stars cannot be observed. With current observations, low-mass stars with intrinsic magnitude $K \geq 21$ mag, cannot be observed in these dense central regions and the true value of the mass-to-light (M/L) ratio is not known.

Similarly, since the radial diffusion time $\sim 10^{8-9}$ yr is shorter than the age of the bulge, a large number of massive compact remnants (5-10 M_{\odot} black holes), which are undetected with observations, could have segregated towards the centre of the cluster, and may dominate the matter density inside the dynamical sphere of influence of the black hole (Morris 1993; Miralda-Escudé & Gould 2000). This can contribute largely to an increase of the M/L in the central regions of a galaxy. Also, as pointed out by Baumgardt et al. (2003), dynamical evolution of a dense stellar cluster will result in a strong increase of M/L ratio by segregation of stellar evolution remnants to the centre. On the other hand, the approximation that the dynamics in the central region is Keplerian is directly related to the implicit assumption of Eckart et al. (2002a), Schödel et al. (2002, 2003), and Ghez et al. (2005) that the M/L ratio at $2 \mu\text{m}$ in the cusp is as low as in the outer stellar cluster ($M/L = 2M_{\odot}/L_{\odot}$).

Normally the gravitational potential in a Galaxy is determined by the stars and distributed dark matter. But in galactic nuclei possessing massive black holes, the central potential in the inner radius is dominated by the black hole and is hence nearly Keplerian. However, at very small scales of few milliparsecs, the dynamics are still not investigated. Therefore, the short orbital period stars are a key to investigating the potential at these distances. It is of great interest to better understand the evolution of the nuclear star cluster itself. Given the existing evidence for hot, massive stars in the central parsec (e.g. Genzel et al. 1996), this work presents a first study of this kind, of whether a considerable amount of mass, which would be possible to detect in future observations, could be hidden in the very vicinity of the super-massive black hole. This will help to place valuable constraints on models of the cusp structure. For this purpose, the star S2 of which orbital data are best known, plays a key role in exploring the gravitational potential. I show that the present observational data on S2 cannot discriminate between a *Keplerian* and a *non-Keplerian* potential (see Fig 1.4). Subsequently, I study the influence of an extended distribution of dark mass near Sgr A* taking into consideration the constraints set by the measurements of positions and radial velocities along the orbit of S2 as well as the limits set on the total enclosed mass at larger radii.

Chapter 2 is a short introduction on the instruments used to acquire the data needed for this work as well as a brief description of the applied data reduction techniques. An introduction to the components of the central stellar cluster is given in chapter 3 together with results of the two works on some 'dust-embedded' objects published by Eckart et al. (2004) and Moultaqa et al. (2004). Chapter 4 summarizes my modelling of the available data on the central cluster density and mass distribution, chapter 5 describes the code I adopted and developed, in the framework

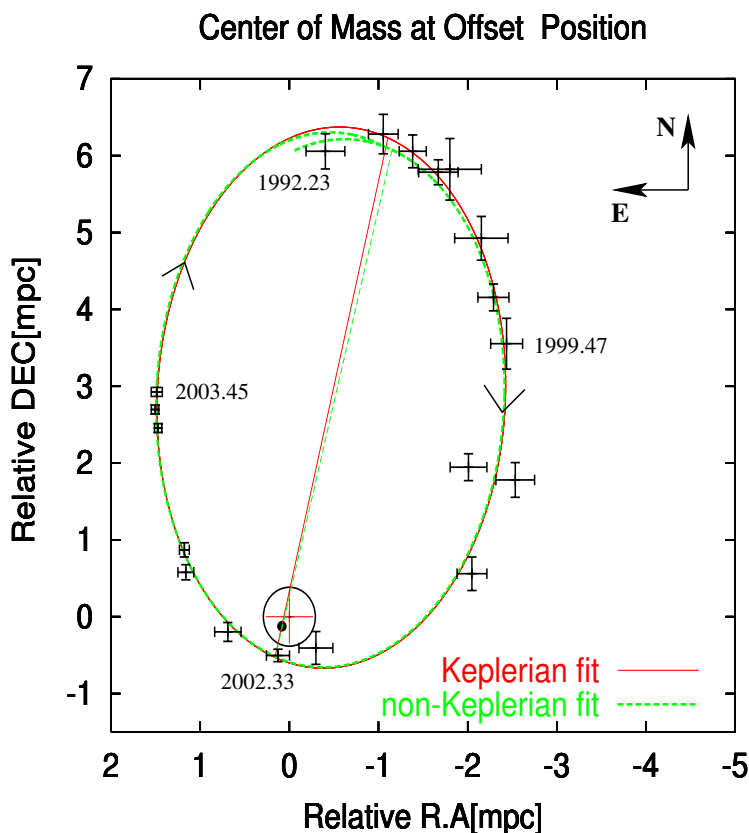


Figure 1.4: **Superposition of Keplerian and non-Keplerian Orbits of the Star S2.** *Superposition of the two best fitting orbits. red solid line: Keplerian orbit with $3.65 \times 10^6 M_{\odot}$ point mass. Green dashed line, non-Keplerian orbits with $4.8 \times 10^6 M_{\odot}$ total mass of which $1.2 \times 10^6 M_{\odot}$ are extended component. Here the central mass is at the offset position, 0.082 mpc east and 0.112 mpc south from the nominal radio position of Sgr A*. The line connecting the peri-centre and the apo-centre is shown for both Keplerian and non-Keplerian case in straight red line and dashed green line respectively.*

of this thesis, to compute stellar trajectories in the vicinity of the SMBH and in the presence of an extended mass distribution. In chapter 6 the method applied to model orbits in Keplerian and non-Keplerian potentials is explained. Results of the possible orbital models for S2 are presented in chapter 7. A discussion of the implications of the limits on the cusp mass derived from the *non-Keplerian* orbital modelling is presented in chapter 8, a summary and conclusions are given in chapter 9.

Chapter 2

Observational Techniques

In this work, data from three instruments SHARP, GEMINI and NAOS were used. With SHARP the near-infrared speckle camera, observations of the Galactic Centre were performed from 1991 till 2002 with a rate of one or two observation runs per year. The last observation run on SHARP took place in July 2002 within the framework of this thesis. I took part in the observing runs, carried out part of the observations and performed data reduction to control the quality of the incoming data. The GC stellar cluster was then observed several times during the commissioning and science verification of the NAOS/CONICA ("NACO") adaptive optic system and near infrared camera at the ESO VLT unit telescope 4 (Yepun) in spring/summer 2002. In 2003, several epochs of regular H, K_S ($2.18 \mu\text{m}$), and L'-band GC imaging observations were obtained with NACO. In this work only the use of the K-band data was necessary. The K - K_S color differences are smaller than the photometric precision accuracy of typically 0.1-0.15 mag that is reached, therefore no distinction is made between both bands throughout this work. In the following two sections, a short description of the three instruments used to observe the Galactic Centre as well as of the data reduction tools is given. The data reduction processes described in this chapter, which was applied to the data used for this thesis, is based on Reid et al. (2003), Genzel et al. (2003), and mainly on Schödel (2004).

2.1 Instruments

2.1.1 The SHARP/NTT Camera

Speckle interferometry

The atmospheric turbulence above the telescope distorts the otherwise planar stellar wavefronts and is responsible for a point spread function (PSF) that varies rapidly with time. This phenomenon is called seeing. For small angular displacements on the sky, the resulting PSF can be considered to be identical. In short exposure images, however, individual bright spots - speckles - are visible. Recording a large number of these short exposure images allows one to compensate for the degrading influences of the turbulent atmosphere and to reconstruct images at the diffraction limit of the telescope (for a detailed description of (infrared) speckle interferometry

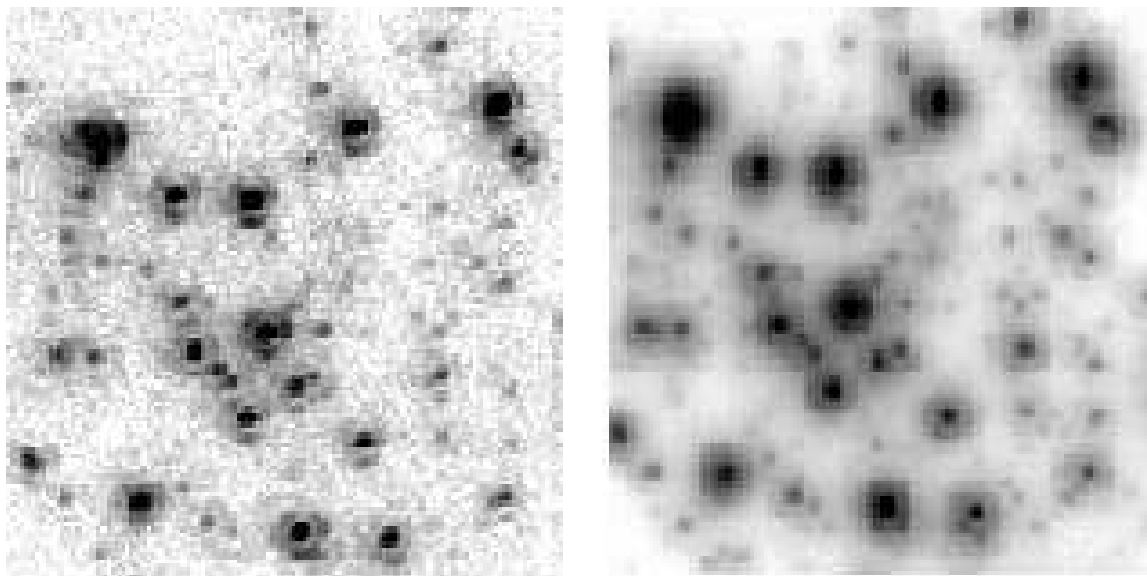


Figure 2.1: **Quality of Speckle images.** *Left: Speckle frame observed under excellent atmospheric conditions. The signal to light ratio (S/N) is high and the image is basically a diffraction limited short exposure with the first diffraction rings clearly visible around the brighter sources. The visible stars have K -magnitudes between about 9 and 14. Right: SSA image of a cube of about 100 high quality speckle frames; Strehl ratio of about 35%. Numerous faint sources, can be well distinguished in this high-quality image.*

and imaging, see Christou 1991 or Dainty 1975, Eckart 1998).

The SHARP/NTT imaging data

The near-infrared speckle camera SHARP was built at MPE for high resolution imaging observations as a guest instrument at the ESO 3.6 m NTT telescope at La Silla, Chile (Hofmann et al., 1995). It was equipped with a 256×256 pixel NICMOS array. It covered a wavelength range from $1 \mu\text{m}$ to $2.5 \mu\text{m}$ and had a pixel scale of about 50 mas per pixel.

The excellent atmospheric conditions and the fact that the GC passes close to zenith in La Silla made it possible to use integration times as long as 1 s and still obtain information at the diffraction limit of the NTT in the images. All SHARP imaging data used for the present work were taken in the K -band (central wavelength $2.2 \mu\text{m}$) with 0.5 s integration time, which was found to be the optimal choice for satisfying the somewhat contrary aims of a high signal-to-noise (S/N) ratio while conserving at the same time information at the diffraction limit of the NTT. The GC stellar cluster was usually imaged in series of 500 or 1000 exposures. The field-of-view (FOV) of SHARP at the NTT was about 13 arcsecs. Applying offsets of a few arcseconds between the imaging series allowed for a 20 arcseconds FOV in the final mosaics. The IRS 16 cluster of bright HeI stars and the Sgr A* cluster were always contained in the FOV.

Co-adding the 500 or 1000 exposures after shifting the position of the brightest speckle in

the seeing cloud of a bright reference object to a common location results in an image containing substantial power at the diffraction limit of the telescope. This is performed by applying the simple shift-and-add algorithm (SSA). However, if only the best speckle frames of a given epoch were selected before applying the SSA algorithm, the Strehl ratio was found to be of the order 30% in the final images, compared to Strehl ratios of the order 10% in SSA images made from speckle data cubes without frame selection, the former method was consequently applied (Schödel 2004). The obtained images still have to be corrected for the SSA point spread function (PSF). For this purpose, the Iterative Blind Deconvolution was applied on the high-quality SSA images. They were cleaned in a final step with a Lucy-Richardson deconvolution. The purpose of the deconvolution is not to enhance resolution, but to remove ('CLEAN') the images from the effects of the PSF. As a result of the two-stage deconvolution, close point sources could be separated better than with just a one stage deconvolution.

2.1.2 Gemini imaging Data

The Gemini North observatory Galactic Center Demonstration Science Data Set with imaging observations from the year 2000 is publicly available. This data set provides observations of the Galactic Center stellar cluster with the Gemini North telescope, the Quirc near infrared camera and the Hokupa'a AO system. A K'-band ($2.12 \mu\text{m}$) image was selected. It is of 750 s total integration time, observed in July 2000. Since the Hokupa'a AO system was designed for a 4m-class telescope, it could only partially provide the correction needed for the 8m-class Gemini telescope. Moreover, the visible guiding star used for the observations is located at $\sim 30''$ from Sgr A*, so the Strehl ratio of the image is rather low. However, the central sources around Sgr A* are clearly resolved at an estimated resolution of 100 mas. PSFs were extracted in an adequate way (for more details, see Schödel, 2004). These were used for a Lucy Richardson (LR) deconvolution of the K'-band image, which was reconvolved to a final map with a Gaussian beam of 100 mas FWHM. In this work, the position of the star S2 is used only in the epoch 2000.

2.1.3 The NAOS/CONICA Camera

What is adaptive optics?

Adaptive Optics (AO) systems provide the astronomer with means of real time compensation of the image degradation from the ground. Throughout the technical developments in building telescopes, two parameters have been particularly important: the light-collecting power or diameter of the telescope (allowing the detection of fainter and more distant objects) and the angular resolution (or image sharpness). For a perfect telescope used in a vacuum, resolution is directly proportional to the inverse of the telescope diameter ($1.22 \frac{\lambda}{D}$, where D is the diameter of the telescope and λ is the wavelength).

A planar wavefront from a distant star (effectively at infinity) would be converted by the telescope into a perfectly spherical wavefront, forming the image, with an angular resolution only limited by light diffraction - called the diffraction limit. In practice, however, turbulence

in the Earth's atmosphere (e.g due to temperature fluctuations) produces inhomogeneities in the air refractive index. This distorts the spherical wavefront, creating phase errors in the image. Even at the best sites, ground-based telescopes observing at visible wavelengths cannot, because of atmospheric turbulence alone, achieve an angular resolution better than telescopes of 10 to 20 cm diameter.

Adaptive optics consists of using an active optical element such a de-formable mirror to correct the wave-front distortions instantaneously and obtain diffraction limited images. Because of the high bandwidth and the small field to which correction can generally be applied, usually a small de-formable mirror with a diameter of 8 to 20 cm is used. It is located behind the focus of the telescope at or near an image of the pupil.

Several steps are carried out to obtain a nearly diffraction limited image. First, one needs a reference star - *a guide star* - to measure the atmospheric distortions. It should be relatively bright and as close as possible to the target. The wave-front sensor - *a high speed camera* - will measure how the light is distorted. It sends the control signals to the de-formable mirror in order to correct the aberrations. Then the corrected focus can be recorded by a camera with an exposure time independent of atmospheric turbulence. This induces sharper images which makes possible the detection of faint stars close to the brighter ones. Furthermore, with AO it becomes possible to do spectroscopy on very small angular scales, and therefore fainter objects can be studied, because less of the night-sky background is included in the light being analyzed.

2.1.4 The AO system on NAOS/CONICA

NAOS/CONICA has an infrared wavefront sensor. For the K-band, this permits wave-front correction on the bright ($K = 6.5$ mag) red supergiant IRS 7 located $5.5''$ north of Sgr A*. All other instruments have to lock on a relatively faint visible star at a distance of about $20''$. Furthermore, the 1K CONICA detector gives a field of view as large as $30''$, resulting in a major improvement in the astrometric analysis of the infrared data (see section 2.3.2). The NACO observations were made in blocks of several tens of short exposures images, with typical integration times of 15s for the K-band observations. The individual images were flat-fielded, sky-subtracted and corrected for detector bias and dead/bad pixels. The final frames were co-added with a simple shift-and-add (SSA) algorithm. Sources brighter than $K=10$ were saturated in all K-band frames with moderate to high image quality. The performance of the NAOS AO system depends strongly on the momentary atmospheric turbulence, especially on coherence time, but Strehl ratios as high as 50 - 70% in K band can be routinely achieved under good conditions. Final long exposure images were produced by co-adding all individual frames with the SSA technique. From the final images, median PSFs were then extracted with StarFinder, which were used for LR or linear deconvolution. In the case of LR deconvolution, final maps were obtained after restoration with a Gaussian beam of 60 mas FWHM in K-band (see Ott et al. 2003 & Schödel et al. 2004 for more informations).

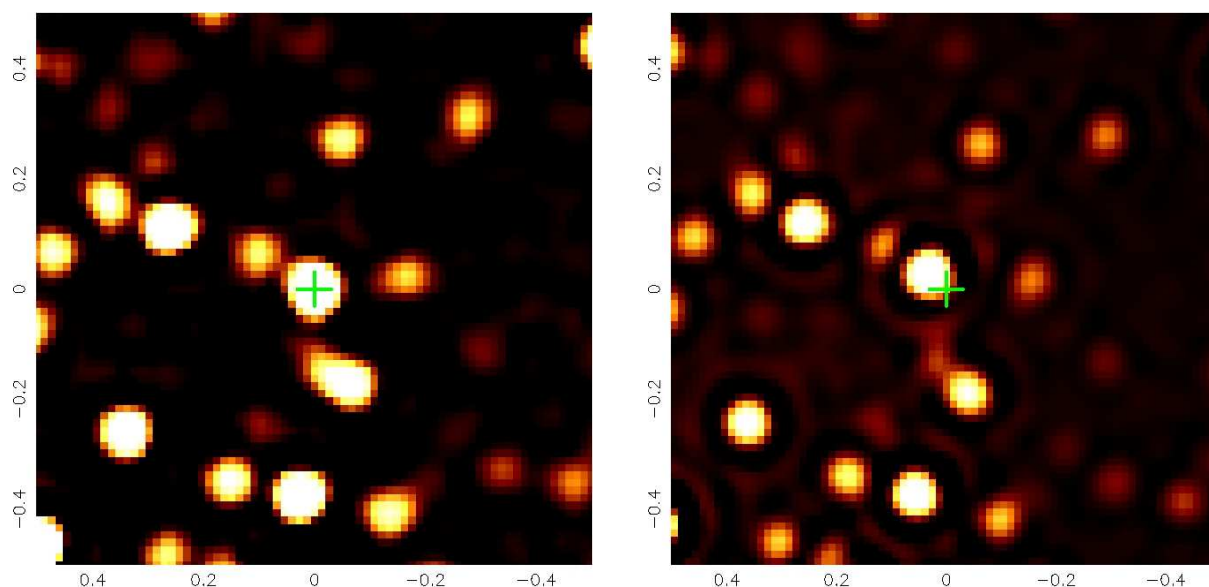


Figure 2.2: **Quality of Adaptive optics images with NACO.** *NACO K-band images of the central $1'' \times 1''$ of the nuclear star cluster for May 2002 and August 2002. The astrometric position of Sgr A* is indicated by a cross of 30 mas. The star next to Sgr A* is S2, which passed close to Sgr A* in spring 2002. Its high proper motion is clearly visible when comparing the images taken just three months apart.*

2.2 Brief Results Obtained by SHARP and NACO on the GC

Here is a summary of the history of the main results obtained with SHARP and NACO during the past 12 years in combination with other data:

- The source at the position of the radio source Sgr A* at the centre of the Galaxy was detected. This extended source found in the first measurements (Eckart et al. 1992), was resolved into a small stellar cluster, referred to, henceforth, as the 'Sgr A* cluster' (Eckart et al. 1995).
- The variation of positions of different stars observed at different epochs, allowed Eckart & Genzel (1996) to measure proper motions of individual stars in the central stellar cluster.
- In 1997, the near-infrared $2.2 \mu\text{m}$ counterpart of Sgr A* was for the first time detected but not confirmed (Genzel et al. 1997).
- The dark mass at the centre was dynamically estimated to be $\sim 3 \times 10^6 M_{\odot}$. It was attributed to a central black hole associated with the compact radio source Sgr A*.
- With speckle spectroscopy, it was possible to derive spectral properties of some of the sources that are in the vicinity of Sgr A*. Later, imaging spectroscopy, using the MPE 3D spectrograph, was carried out at the ESO/MPG 2.2m telescope on La Silla. These

data provided stellar classification and radial velocities for the brightest 100 stars in the GC.

- In 2002, Eckart et al. (2002) confirmed and improved the first measured accelerations by Ghez et al. (1998) of three S-stars. Possible Keplerian orbits were fitted to the stars' trajectories and the first orbital elements could be derived. It could be shown that the star S2 is bound to the central BH
- It is only after the star S2, observed with both SHARP and NACO at different epochs, passed its peri-centre in spring/summer 2002 that the first unique Keplerian orbit was determined (Schödel et al. 2002, and Ghez et al. 2003 with the KECK). Most alternative models to a SMBH (neutrino ball, dense cluster of dark objects) could be excluded, leaving a single SMBH as the most likely explanation for the observed dark mass.
- With NAOS/CONICA in 2003 a greater precision was attained, and our knowledge about the stellar counts and distribution was enhanced (see Fig 3.1). The data reach to K-band ~ 19 , ~ 3 magnitudes deeper than any Galactic Centre image taken before. The combination of the different data from different instruments allowed a wider understanding of the stellar properties.
- With NAOS/CONICA in 2003, the first unambiguous detection of Sgr A* in the infrared waveband was detected (Genzel et al. 2003b). These high-resolution infrared observations of Sgr A* revealed 'quiescent' emission and several flares allowing to study the properties of the SMBH (see section 3.3).

2.3 Astrometry

In order to study the different physical properties of the stellar cluster near the central black hole, Sgr A*, it is very important to establish an accurate astrometric system that enables us to determine a precise position of the stars relative to Sgr A*. Also, when the position of Sgr A* is well constrained relatively to its surrounding stars, it becomes easier to find a near-infrared counterpart of that source.

Hence, positions of the stars for each epoch should be transformed in one frame of reference. The measured positions then have to be transformed to a common coordinate system so they can be compared and allow the determination of proper motions.

2.3.1 Use of the SiO masers to establish an astrometric reference frame

The position of Sgr A* is a priori unknown on NIR images due to the faintness of this source in this wavelength regime. It is however one of the brightest radio sources in the sky. Thus, combining speckle/AO NIR high resolution images with interferometric radio images allowed a higher positional accuracy by more than one magnitude (Menten et al. 1997, Reid et al. 2003, Schödel 2004). This task was possible due the presence of stars which are bright in both wavelengths, and therefore well determined in both frames. It is possible to lock both images

Table 2.1: **Positions and proper motions of SiO masers within of 15'' of Sgr A*.** The data are taken from Reid et. al (2003) and are based on several epochs of observations with the VLA and VLBA. $\Delta\Omega_x$ and $\Delta\Omega_y$ are angular offsets, Δx and Δy are proper motions relative to Sgr A*, toward the east and north respectively, in the J2000 coordinate system.

Star	$\Delta\Omega_x$ (arcsec)		$\Delta\Omega_y$ (arcsec)		Δx (mas y ⁻¹)		Δy (mas y ⁻¹)		Epoch (y)
IRS 9	+5.6531	0.0006	-6.3493	0.0013	+3.60	0.53	+2.40	1.13	1999.24
IRS 7	+0.0364	0.0013	+5.5461	0.0043	-1.57	0.92	-4.54	3.47	1999.55
IRS 12N	-3.2531	0.0003	-6.8853	.0003	-0.82	0.22	-2.81	0.26	1997.77
IRS 28	+10.4694	0.0010	-5.7944	0.0022	-0.37	1.30	-2.95	2.27	2000.44
IRS 10EE	+7.6840	0.0003	+4.2150	0.0003	+0.20	0.16	-2.12	0.20	1998.52
IRS 15NE	+1.2283	0.0003	+11.3249	0.0004	-1.66	0.24	-5.96	0.35	1997.54
IRS 17	+13.1501	0.0026	+5.5651	0.0025		2000.85

on these bright stars and this way match the two NIR and radio images.

Few of such stars exist within 15'' of Sgr A* (see Fig 2.2). These are red, cool giant and supergiant stars that exhibit strong hydroxyl (OH at 1.663 GHz), water (H₂O at 22.235 GHz) and/or silicon monoxide (SiO at 43.122 GHz) maser emission. The SiO masers seem to arise from the innermost regions (~ 4 - 8 AU radius) of the circumstellar envelopes of these stars (Diamond et al. 1994, Miyoshi et al. 1994, Greenhill et al. 1995), while the H₂O maser radiation originates in the stellar atmospheres of many OH/IR stars (infrared bright, short-lived stars in a high mass-loss phase, see, e.g, Winnberg et al. 1985). Thus, by constraining the emitting region from such stars, it became possible, with the help of radio interferometers (VLA and VLBA), to measure the positions and proper motions of 7 SiO stars with an accuracy < 1 mas (Menten et al., 1997; Reid et al., 2003).

K-band observations of the GC star cluster with the S27 camera of NAOS/CONICA in May 2002 (epoch 2002.34) provided high quality AO images of this region with a field-of-view containing all seven SiO masers listed in Table 2.1. Since the Galactic Centre was observed as a mosaic, the complete field covers a region of 20'' × 20''. In May 2002 observations with NAOS/CONICA at the VLT that covered a field of 40'' × 40'' were performed. The final mosaic image from 2003 is shown in Fig. 2.2 as given by Schödel (2004). The SiO masers are marked by circles in this image. By comparing the pixel positions of these maser stars in a NIR image with their offsets in right ascension and declination relative to Sgr A* as measured by radio observations, it is possible to align the NIR and radio positional reference frames relative to each other.

Measuring stellar proper motions

The higher resolution and larger field-of-view of NACO and the longer baseline of the radio data, needed in the alignment process, enabled Reid et al. (2003) to solve for higher order terms, compared to Menten et al. (1997). Therefore they could determine the position of Sgr A* in the NIR frame with an uncertainty of less than 10 mas in comparison to an earlier determination of

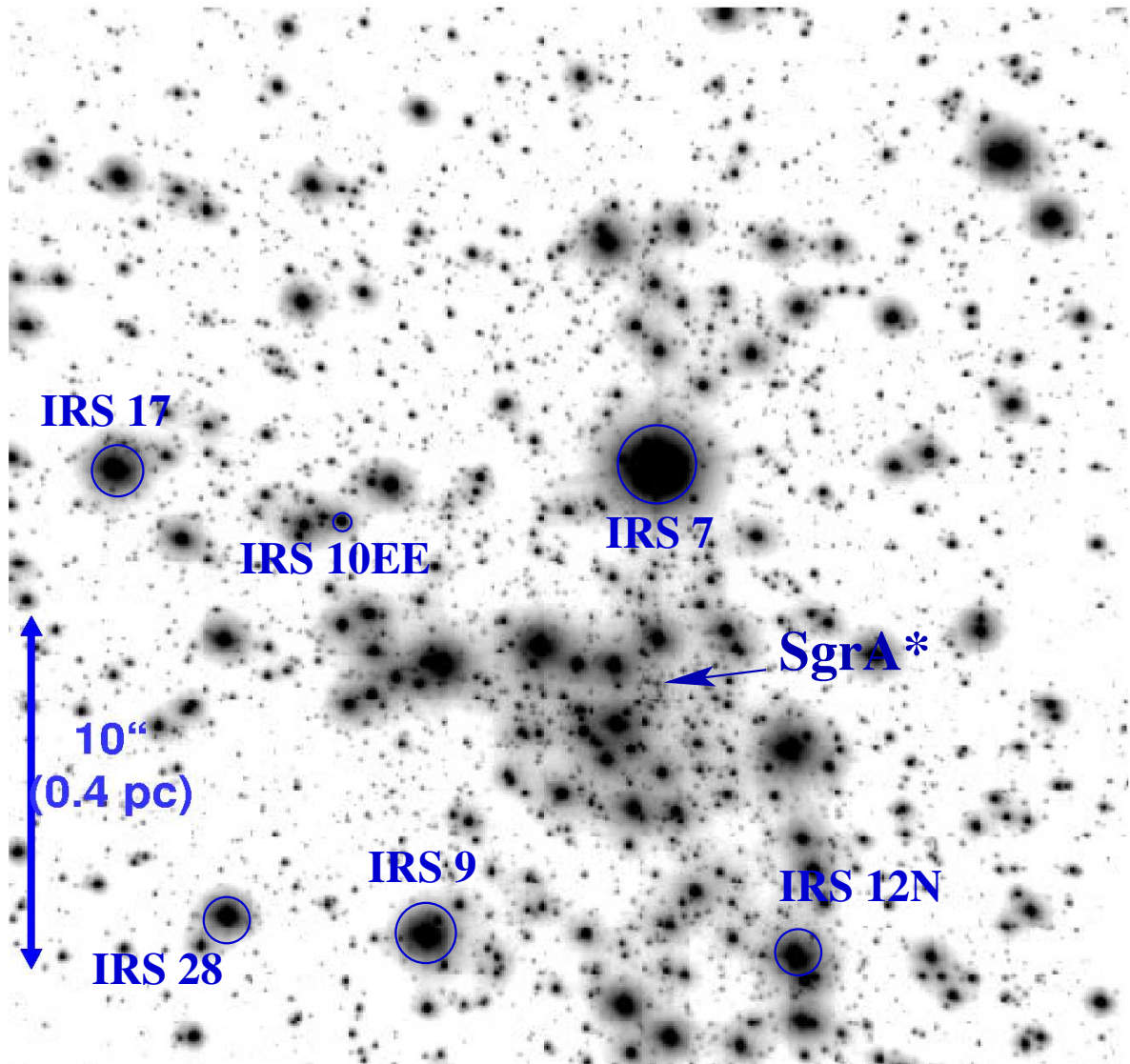


Figure 2.3: NACO GC K-band image. The 7 maser sources in the field-of-view are marked by circles. Their positions and proper motions, measured with radio interferometry, are listed in table 2.1. The position of Sgr A* is marked by an asterisk. Offsets from Sgr A* in arc-seconds are marked on the x and y axes, positive to the north and to the east.

only 30 mas when using the 2 available SiO maser stars on the smaller field-of-view ($\sim 13''$) of SHARP (Menten et al. 1997). The 7 SiO sources were used to calculate the plate constants of the infrared imaging. The transformation between the pixel coordinates (x_i, y_i) of the i_{th} star in an image and the corrected offset coordinates $(\Delta x_i, \Delta y_i)$ from the base position can be written as:

$$x_i = a_0 + a_1 \Delta x_i + a_2 \Delta y_i + a_3 \Delta x_i^2 + a_4 \Delta x_i \Delta y_i + a_5 \Delta y_i^2 \quad (2.1)$$

and

$$y_i = b_0 + b_1 \Delta x_i + b_2 \Delta y_i + b_3 \Delta x_i^2 + b_4 \Delta x_i \Delta y_i + b_5 \Delta y_i^2 \quad (2.2)$$

The 0^{th} order is the base position (a_0, b_0) , the 1^{st} order (proportional to Δx and Δy in each coordinate) relates to a variation in pixel as well as a rotation of the camera, and the 2^{nd} order parameters (proportional to Δx^2 , Δy^2 and $\Delta x \Delta y$ for each coordinate) give the image distortions such as shear. Using the centroid positions in the infrared image of the 7 maser stars, it is possible to solve the system of astrometric equations (eq 2.1 & eq 2.2) up to the 2^{nd} order and therefore determine the value of the parameters $(a_0, b_0, \dots, a_5, b_5)$, hence to align pixel positions in the CONICA image with the SiO radio reference frame. These high-quality NAOS/CONICA data were used to create a first list of stars which serves to re-identify the stars in all other observations. Ott et al. (2003) used about 50 to 200 stars to determine the transformation parameters. Therefore, by solving for an overdetermined system of equations, the transformations between different epochs were of high accuracy. The transformation matrix was applied to all stars in the initial list, resulting in an astrometric (relative to Sgr A*) master-list of stars at the epoch of the CONICA observation. This initial list of stars consists of stellar positions in pixel coordinates of the CONICA reference frame. This was transformed to physical astrometric coordinates (relative to the radio source Sgr A*). Once stellar astrometric positions have been established for several epochs, the proper motions of the stars can be determined, i.e the motions of the stars as they appear projected onto the plane of the sky. With the highest quality data of NAOS/CONICA (and similarly for the Keck data), a baseline as short as 2 years is sufficient to detect proper motions larger than about one hundred kilometers per second.

2.3.2 Main observing results with NAOS/CONICA

On NAOS/CONICA, with integration times of about 20 minutes, the data reach to K-band ~ 19 , ~ 3 magnitudes deeper than any Galactic Centre image taken before. The dynamic range of the images is about 13 magnitudes but bright stars are saturated in the deepest images. The images in Figure 3.1 demonstrate the complexity of the dense stellar environment in the central parsec. Bright blue supergiants (in the IRS16 and IRS13 complexes), as well as red supergiants (IRS 7) and asymptotic giant branch stars (IRS12N, 10EE and 15NE) dominate the H- and K-images. At L' there is an additional group of dusty sources (IRS1, 3, 21). Extended L' emission comes from hot dust in the gaseous 'mini-spiral' streamers comprising the most prominent features of the Sgr A West HII region. The immediate vicinity of Sgr A* lacks bright stars and dust. There is a concentration of moderately bright (K ~ 14) blue stars centered on the radio source (the

‘Sgr A* cluster’). The faintest sources recognizable on the images are equivalent to ~ 2 M A5/F0 main sequence stars. Point sources were then identified. Photometry was carried out with the FIND procedure from the IDL Astrolib library (Schödel 2004). The final source lists comprise between 3200 and 4000 stars, depending on the FIND extraction parameters. To improve the reliability of the photometry, different photometric algorithms were applied and, where possible, results from independent data sets were averaged. The final relative photometric errors are 0.1 mag below $K=18$, but probably twice that for fainter stars. The absolute photometry is uncertain to 0.15 mag in the K-band.

Chapter 3

The Centre of the Milky Way

The solar system is situated at a distance of ~ 8 kpc from the centre of the Galaxy (Reid 1993; Eisenhauer et al. 2003). The Milky Way in its ensemble has an approximate mass of around $7 \times 10^{11} M_{\odot}$. It is classified as a barred spiral galaxy. The centre is dominated by an exceptional concentration of dark mass, which is best explained by the presence of a supermassive black hole (SMBH). The denomination of 'Galactic Centre' is very imprecise: it comprises different scales, from the kiloparsec to the central parsec and even to the milli-parsec scale. In the following, I give an overview of the characteristics of the central regions of the Galaxy concerning the inner parsec and a more detailed description on the scale of the hundredth of the parsec which represents the region of interest in this work. This includes its most peculiar object, the central SMBH Sagittarius A* (Sgr A*). Section 3.2.1 and section 3.2.2 will be a summary of articles to which I contributed concerning the interpretation of embedded objects in the inner parsec. Different review papers were written on the Galactic Centre, the most recent ones are by Morris & Serabyn (1996), Mezger et al. (1996) and Melia & Falcke (2001) as well as books and conference proceedings, the most recent one is by Eckart, Schödel & Straubmeier (2005).

3.1 The Interstellar Medium

There exists, around the central parsec, a dense ($10^4 - 10^7 \text{ cm}^{-3}$), warm (several hundred K) and turbulent ring of molecular and atomic gas which is referred to as the circumnuclear disk (CND). The central source Sgr A* is surrounded by a huge HII region, Sgr A* West with a size of 2.1×2.9 pc. The ionized gas in this region forms a spiral pattern (see e.g. Lo & Claussen 1983; Lacy et al. 1991) and is therefore called the mini-spiral. The western side of this feature represents the inner edge of the CND which, itself, extends from ~ 1.5 to 7 pc from the centre. The total gas mass of the CND is estimated to be $3 \times 10^5 M_{\odot}$ (Shukla et al. 2004), it is very clumpy with an estimated volume filling factor 0.01, the clumps have masses of $\sim 30 M_{\odot}$, sizes of ~ 0.1 pc, and temperatures ≥ 100 K. Inside this inner radius of 1.5 pc, there is a cavity, where only atomic and ionized, but hardly any molecular gas can be found. Several streamers of ionized gas and dust appear to be on infalling trajectories from the inner edge of the CND. They are orbiting the centre and interact with the intense winds emanating from the stars in the nuclear star cluster forming this way the mini-spiral. Parts of the mini-spiral can be seen in

the diffuse emission in the L-band ($3.8\mu\text{m}$) image of the central parsec (see Fig 3.2). Vollmer & Duschl (2000) localized 3 different planes. It is now clear that the mini-spiral connects the CNB to the central stellar cluster. They found that most of the dust and gas, mainly present in one plane containing the northern arm and the eastern bar, is connected to the inner edge of the CNB. A more detailed structure of it, largely consistent with the model of Vollmer & Duschl (2000), identifies nine different patterns (Paumard et al. 2003). More details on the interstellar medium in the GC can be found in the reviews by Genzel, Hollenbach, & Townes (1994), Morris & Serabyn (1996), and Yusef-Zadeh et al. (2000).

3.2 The Nuclear Stellar Cluster

At the centre of the Galaxy, it was possible to detect all red and most blue super-giants, all red giants and all main sequence stars down to about $2 M_{\odot}$. At a distance of 8 kpc this corresponds to a magnitude limit of $\sim 18^m$ in the K-band. This was achieved with high-resolution near infrared (NIR) speckle imaging observations at the NTT and Keck telescopes, and lately with adaptive optics observations at 8m class telescopes. Several thousands of stars have been sampled in the central few arcseconds of the GC stellar, nevertheless, our knowledge on the stellar cluster is based on just around 0.1% of the total observed stellar content of the cluster (Genzel et al. 2003, Schödel et al. 2004). The distribution of stars at distances ≥ 0.5 pc from the Galactic Centre, follows that of a near-isothermal cluster. Direct number density counts indicate that the stellar volume density increases with a power law of R^{-2} from projected radii of $100''$ (4 pc) up to about $10''$ (0.4 pc) (Catchpole, Whitelock & Glass, 1990; Genzel et al., 1996, 2003). However, Scoville et al. (2003) find a much shallower radial density distribution ($R^{-0.5}$). The reason for the differences are still unclear. Inside $\sim 10''$, the stars follow a shallower power-law density distribution, (Genzel et al., 1996, 2000, 2003). This is consistent with the prediction of theoretical models on the formation of a cusp of stars surrounding a massive central black hole. The distribution of the different stellar populations in the centre is inhomogeneous. There are indications that the stellar properties change significantly from the outer cluster ($\leq 9''$) to the dense innermost region ($\leq 1.5''$) around the black hole. The outer cluster seems to be formed of an old, metal-rich stellar population with a contribution from young, early, and late-type stars. In contrast, inside a distance of $1.5''$ from Sgr A*, it appears as if old, low-mass, horizontal-branch/red-clump stars are lacking (Genzel et al. 2003).

The most important components of the GC stellar cluster are indicated in Fig 3.1 and are briefly described in the following:

- About $6''$ north of SgrA *, IRS 7 is the brightest source in the central parsec. It is a long period variable red supergiant (class M1, $T_{eff} \sim 3500\text{K}$), with an apparent average magnitude in K-band of ~ 6.5 (Blum, Sellgren, & DePoy, 1996; Ott et al., 1999). The stellar mass and the near-IR light at $K > 13$ is dominated by red giants in the old component (1 - 10 Gyr) of the nuclear cluster.

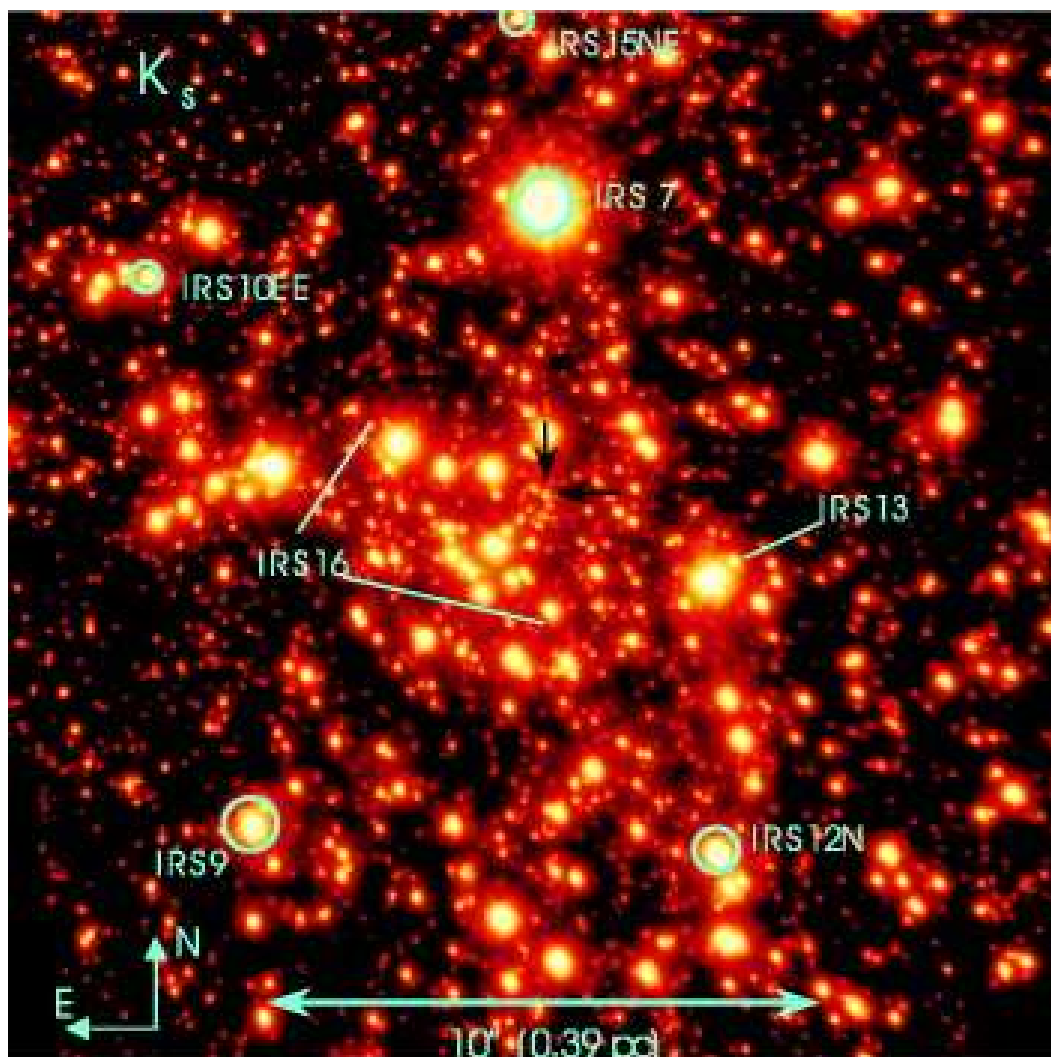


Figure 3.1: **K_s image of the central $\sim 20''$.** NAOS/CONICA SSA image of the central $20''$, taken in 2002 August (55 mas FWHM resolution; Strehl ratio $\sim 50\%$). A logarithmic color scale is used. East is to the left, and north is up. The brightest star, IRS 7 (6.7 mag), was used for infrared wave front sensing. The faintest stars visible on the image are $K_s \sim 19$. The five encircled stars (of seven in the central $30''$) are also radio SiO masers and were used for establishing the selected orientations of the infrared camera and to put the infrared data in the radio astrometric reference frame (rms ± 10 mas; Reid et al. 2003). In addition, the IRS 16 and IRS 13 complexes of emission-line stars are marked. The two arrows denote the position of Sgr A*.

- In the central few arcseconds, the luminosity is dominated by more than two dozen hot, massive, bright ($K \sim 9 - 12$), blue stars, which are characterized by strong H I/He I emission lines. Indeed, the near-IR light distribution peaks on the IRS 16 complex, which, together with IRS 13 complex, holds the highest concentration of the He I stars. IRS 16 SW a component of the IRS 16 cluster is classified as an eclipsing binary (period of 9.72 days) with a mass of $\leq 104 M_{\odot}$ (Ott et al. 1999). The He I stars are early-type stars with surface temperatures of 20000 - 30000 K and are massive sources ($30-100 M_{\odot}$) of intense stellar winds. The properties of these bright emission-line stars are essentially identical to the massive stars in the Quintuplet and Arches clusters, 30-50 pc away from Sgr A*, in much lower density environments (Figer et al. 1998; Cotera et al. 1999; Figer 2003). They are not dynamically relaxed, a characteristic that is not consistent with theoretical prediction of the formation of a steady state cusp. They might be witnesses of a star formation episode between 2 and 7 million years ago (Eckart et al., 1995; Allen, D. A., Hyland, A. R., & Hillier, D. J., 1990; Krabbe et al., 1995; Najarro et al., 1994, 1997). They display a coherent rotation pattern with a direction opposite (counter) to that of the overall Galactic rotation, and seem to reside in two rotating disks with different angles and inclinations (Levin & Beloborodov 2003; Genzel et al, 2003). The two disks are at large angles relative to each other and effectively counter-rotate but do share a common projection of their rotation vectors that are opposite to that of Galactic rotation (Genzel et al., 2003). This could be interpreted as a remnant of the angular momentum of the original gas cloud from which these stars have formed (Genzel et al., 2000, Gerhard, 2001).
- At projected distances $p \leq 10''$ (~ 0.4 pc), there is a second component dominating NIR images of the GC stellar cluster. That is a group of intermediate bright ($K \sim 10 - 13$), late-type stars. These stars have been identified as stars at the top of the asymptotic giant branch (AGB), which give testimony of another star formation episode about 100 million years ago. The strength of the CO absorption feature decreases in the central few arcseconds around Sgr A*. This may be due to an actual lack of late-type giants there because their envelopes are destroyed by collisions in the dense stellar cluster (Sellgren et al., 1990; Genzel et al., 1996; Alexander, 1999). Alternatively, the presence of luminous, blue stars (the "He I-stars") in the central few arcseconds might dilute the CO absorption feature (Sellgren et al., 1990; Eckart et al., 1995; Krabbe et al., 1995; Genzel et al., 1996; Haller et al., 1996; Blum, Sellgren, & DePoy, 1996). Recently, Figer et al. (2003) measured the radial velocities of 85 cool, normal giant stars with projected distances from the central region between 0.1 pc and 1 pc. They find a nearly complete deficiency of giants with large radial velocities ($V_{rad} > 200$ km/s). Since a star in a circular orbit at a distance of 0.1 pc from the black hole has a velocity of approximately 400 km/s, the absence of any such stars with comparable radial velocities indicates that the observed giants are indeed limited to the region outside the central ~ 0.4 pc ($\sim 10''$). While the integrated light measurements might suffer from dilution by the light of young stars, the dynamical evidence does not suffer from such a bias.

3.2.1 Embedded objects

There exists in the central 0.5 pc of the GC stellar cluster a population of stars, which are very red, dust embedded sources with featureless K-band spectra. These are bright $10\mu\text{m}$ sources such as IRS 21, IRS 1W, IRS 10W or IRS 3 (e.g. Genzel et al. 1996; Tanner et al. 2003, Pott et al. 2005). These sources are resolved in high-resolution imaging observations, i.e. they are not point sources (Krabbe et al., 1995; Ott et al., 1999; Tanner et al., 2003). With the latest high angular resolution observations, the most supported interpretation is that, these are mass-losing young, massive stars, such as those in the IRS 16 complex, that blow through the interstellar gas and dust of the mini-spiral. The motion of these hot and windy stars through the dense medium will create bow shocks and appear as extended sources. Numerous examples of bow shock source can be found, the best evidence are IRS 21 (Tanner et al. 2003) and IRS 8 (Rigaut et al. 2003). Therefore, the earlier interpretation of such objects as young stellar objects (YSOs) has become very unlikely.

A dozen of these stellar sources are bright in the 2-4 μm wavelength domain. Using *L*-band spectroscopic observation and with the help of *K*-band spectroscopic data, Moultaqa et al. (2004) were able to derive optical depth spectra of these sources after fitting their continuum with a single reddened black body continuum. The visual extinction towards prominent sources within the central stellar cluster range between 29 and 37 magnitudes (Scoville et al. 2003). By means of MIR *L*-band low resolution ($R=600$) spectroscopy obtained at the ESO VLT unit telescope UT1 with ISAAC instrument as well as *K*-band previously published data (Ott et al. 1999), Moultaqa et al. (2004) have derived a detailed picture of the ISM in the half central parsec of the Galaxy.

Optical Depth Towards the Central Parsec

The optical depth spectra of the central parsec bright sources have been derived after performing simultaneous fits of the *K*- and *L*-band spectra with a reddened Blackbody ($3 \leq A_K \leq 4$). The resulting spectra reveal four absorption features:

- The water ice absorption feature at $3.0\mu\text{m}$ observed in molecular clouds.
- The $3.4\mu\text{m}$ and $3.48\mu\text{m}$ features due to aliphatic hydrocarbons which are characterized by their CH₂ and CH₃ stretching modes. These features have been observed toward many Galactic sources (Chiar et al. 2002) and are known to arise in the diffuse ISM.
- A non-identified feature at $3.3\mu\text{m}$ also observed in the Galactic Centre by Chiar et al. (2002).
- The shape of the $3.0\mu\text{m}$ feature is consistent with a 40K ice temperature and a maximum mantle thickness of $0.85\mu\text{m}$ assuming the simple model of core-mantle grains (Bohren et al. 1983) and the hypothesis of a variable mantle thickness (Smith et al. 1993).

The optical depths at the different absorption features have been measured for the most luminous sources of the central half parsec. These measurements reveal a high correlation between

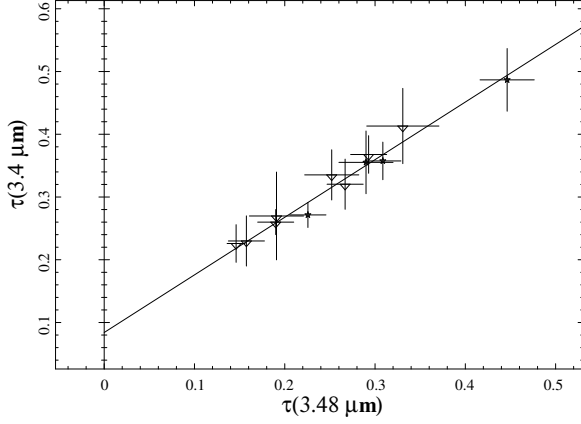


Figure 3.2: **Optical depth at the 3.4 μm versus the 3.48 μm absorption feature.** *Optical depth of the hydrocarbon absorption at the 3.4 μm versus the 3.48 μm absorption feature.*

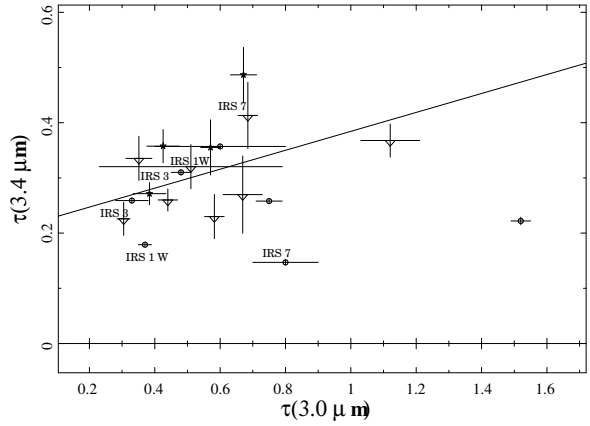


Figure 3.3: **Optical depth at the 3.4 μm versus the 3.48 μm absorption feature.** *Optical depth of the hydrocarbon absorption at the 3.4 μm versus the 3.0 μm absorption feature For all observed Galactic Centre sources (the IRS 16 sources are represented by stars and the remaining sources by triangles). The values obtained by Chiar *et al.* (2002) are also shown (in circles) but are not considered in the linear regression fit.*

the optical depths at 3.4 μm and 3.48 μm (Fig 3.2) which is foreseeable since both features arise from the same functional groups. There is as well a trend of correlation between the optical depth of the 3.0 μm and the 3.48 μm features suggesting that the ISM in the central region is a mixture of diffuse and dense material. A significant offset from the origin of the coordinate system is detected in the correlations between the 3.4 μm and the 3.48 μm (Fig 3.2) and the 3.4 μm versus 3.0 μm (Fig 3.3). It suggests that a certain amount in (and therefore in the corresponding column density) of the 3.4 μm line absorption is due to the diffuse ISM along the line of sight to the Galactic Centre.

The temperatures obtained for each source by the fitting procedure are consistent with the known nature of the sources, this result implies that the K-band absorption magnitude toward the Galactic Centre doesn't vary of more than $A_K = \pm 0.5$ mag.

Calibration of the Extinction Along the Line of Sight

The slit positions adopted for our observations run through a late-type star located well off the mini-spiral emission. The K-band spectrum of this star shows clear 2.3 μm CO absorption bandheads and no excess emission at wavelengths of 3.0 μm or longer are distinguished in its L-band spectrum. Therefore, it was assumed that the emission is mostly affected by the line of sight extinction along the 8 kpc towards the Galactic Centre and that the L-band spectrum of this star can be represented by a 3600K blackbody spectrum. Dividing the spectrum of the previous late-type star by the blackbody continuum provides a measurement of the wavelength

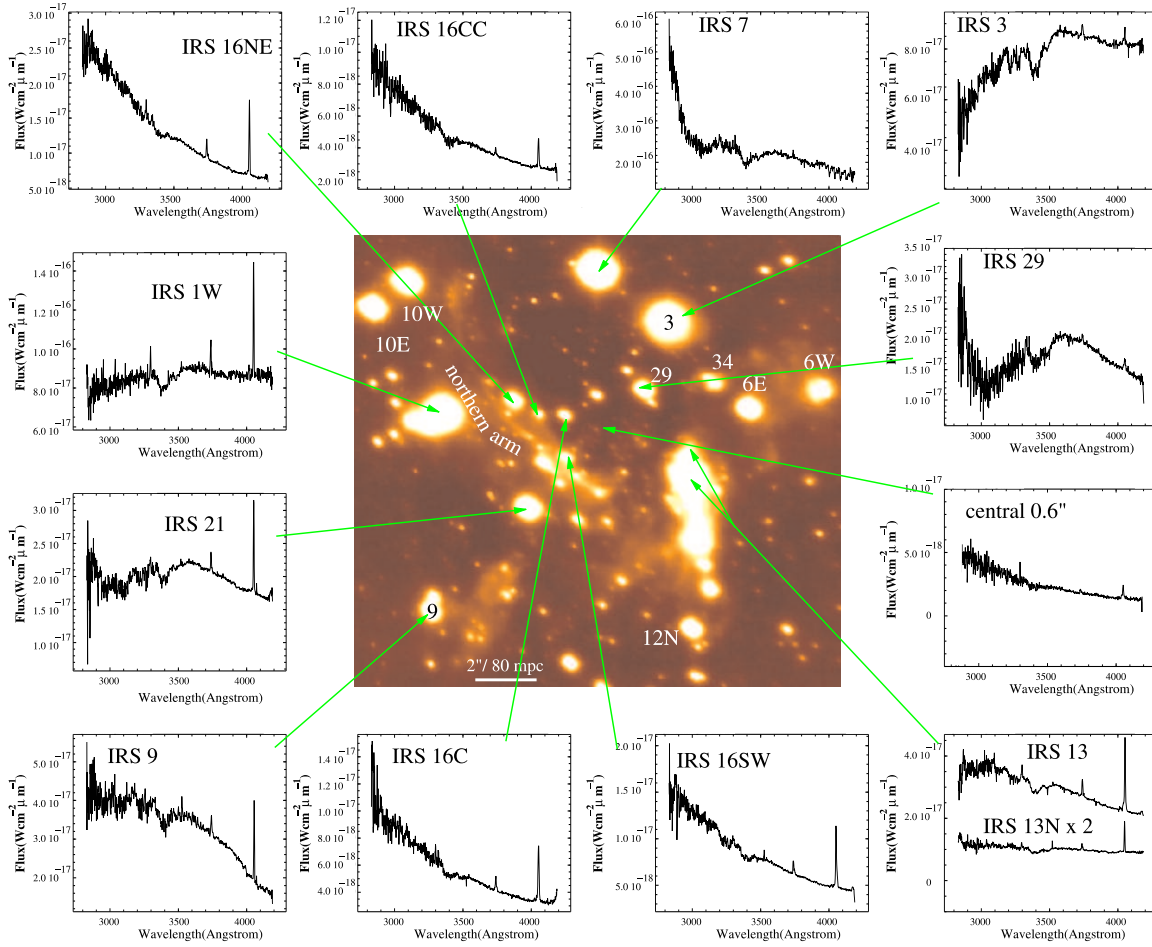


Figure 3.4: ISAAC L-band map combined with the spectra of the central sources. L-band image as obtained with ISAAC on the VLT UT1 combined with the spectra of the most luminous sources in the central parsec, corrected for the line of sight extinction (Moutaka et al., 2004).

dependent L-band absorption due to the ISM along the line of sight. The corrected spectra for extinction along the line of sight of the bright sources are then derived by means of this spectrum and shown in Fig 3.4. The integrated spectrum of a region located $0.5''$ north of IRS 13 complex shows that the IR excess found in this region (Eckart et al. 2004a) is due to the contribution of warm dust $T=500-1000\text{K}$. The IR excess is possibly due to the presence of very young objects in this region.

3.2.2 IR-Excess objects

The IRS 13 complex is a small (diameter $\sim 1''$), luminous cluster of stars located at about $3.5''$ WSW of Sgr A*. It contains one of the brightest hot stars in the entire central parsec (Najarro et al. 1997) and it was recently resolved into 4 bright infrared components (Paumard et al. 2001; Maillard et al. 2003; Eckart et al. 2004a). With the first diffraction-limited images at 1.6, 2.1

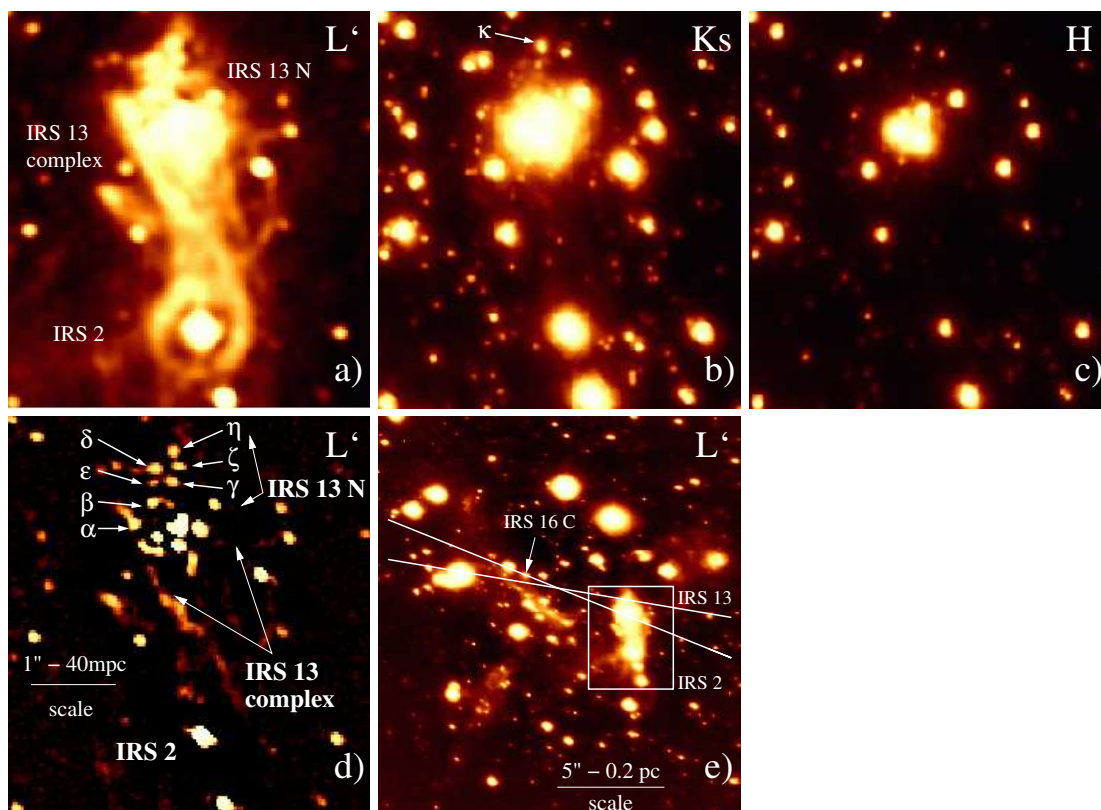


Figure 3.5: H, Ks, and L' band images of the IRS 13/IRS 2 region. The image scales of panels (a-d) are given in (d). Ring structures around the brighter stars are artifacts of the deconvolution algorithm. Panel (d) is a high pass filtered L'-image that shows the locations of individual stars, including the newly discovered L'-band excess sources α through η . (b) Source κ is located between ζ and δ . (e) An overview of the region is shown; the box indicates the area shown in panels (a-d), (Eckart et al. 2004a).

and $3.8\mu\text{m}$ with the adaptive optics camera NAOS/CONICA at the ESO VLT, as well as $3\text{-}4\mu\text{m}$ low-resolution spectroscopy, Eckart et al. (2004a) discovered a small cluster of strong infrared excess sources due to $T \geq 500\text{ K}$ dust, located about $0.5''$ North of IRS 13. The cluster named by IRS 13N has a diameter ≤ 0.13 light years, the individual sources are 10-15 times less luminous than the dusty source IRS 21, compact with angular sizes of less than $0.09''$. These are labeled α through η in Fig 3.5. Stellar proper motions (Genzel et al. 2003; Maillard et al. 2003) provide evidence that the entire IRS 13/IRS 13N complex is moving together with the gas of the mini-spiral, and indicate an orbital time scale of the order of $\sim 10^4$ years for the combined motion of the entire complex and the mini-spiral gas. The IRS 13 sources are well embedded in the bulk of the ionized gas. They dominate the flux density of a weak northern extinction of a region emitting a continuum of radiation due to the dust associated with the compact IRS 13 cluster. All the objects of the IRS 13N are red with regard to the other sources of the field, except κ and η . Due to high stellar density in that cluster, it is difficult to determine flux densities of the stars in the cluster. On a HKL colour-colour diagram, these stars are localized close to the hot and

massive stars near the main sequence stars. The overall spectrum of the IRS 13N presented by Eckart et al. (2004a) is redder than that of the IRS 13 complex, which suggests that the strong L-band excess is most likely due to continuum emission of warm $T > 500$ K dust.

The IRS 13N sources may be low-luminosity counterparts of bow-shock stars such as IRS 21, or - a very intriguing possibility - dust-enshrouded young stellar objects. Another very exciting characteristic of the IRS 13 cluster is the finding of 2 additional sources in the IRS 13 east by Maillard et al. (2004). By using radial velocities of two stars (Maillard et al. 2004) indicate that there could exist in the centre of the IRS 13E cluster an intermediate mass black hole (IMBH) of about $1000 M_{\odot}$. By using proper motions of the stars (Schödel et al. 2005, submitted), however, found that such an IMBH should have a mass of an order of magnitude higher, which makes its presence in the IRS 13E unlikely. They also argue that there is absence of a non-thermal radio source and an X-ray source at this position, therefore, there exists no compelling evidence for the presence of such an IMBH.

3.2.3 Fast moving stars : The S-stars.

There exists a specific concentration of $K \sim 14 - 15$, early-type (S-) stars in the Sgr A* cluster at projected separations of $p \leq 0.5''$ from Sgr A*. A detailed analysis on the angular momentum of the Sgr A* stars shows an excess of radial orbits (Genzel et al. 2000, 2003; Schödel et al. 2003). Fifty-four percent ($\pm 14\%$) of the 35 observed stars in the Sgr A* cluster are on radial orbits (Genzel et al. 2003). These stars are probably observed near the apo-apse of their orbit (roughly twice the semi-major axis), where they spend most of their time. It is therefore likely that the radial stars are tightly bound to the black hole, with semi-major axes of order 20 mpc. Several of them have proper motion velocities (i.e. velocities projected on the sky) in excess of 1000 km s^{-1} , and some of them even show accelerated motion (Eckart & Genzel, 1996, 1997; Ghez et al., 1998, 2000, 2003; Eckart et al., 2002a, Schödel et al. 2002, 2003). Very recent near-IR imaging spectroscopy taken with the new adaptive optics assisted, integral field spectrometer SINFONI on the ESO-VLT (Eisenhauer et al. 2005, submitted), showed that 10 of 11 stars with $K \leq 16$ within $0.5''$ of Sgr A* are early-type stars (see Fig 3.6). Their spectral properties are in excellent agreement with normal, main sequence B0-B7 stars with moderate rotational velocities. This bringing more ambiguity to the 'paradox of youth' (Ghez et al. 2003).

Five of the six innermost stars are on highly elliptical ($e > 0.8$) orbits (see Fig 1.6 in the Introduction), (Ghez et al. 2003, Schödel et al. 2003, Eisenhauer et al. 2005, submitted). The orbit of the star S2 is the one which has been covered almost completely by more than 10 years of observations, it shows the shortest orbit among the S-stars. A series of NIR observations covered the peri-centre passage of the star S2 around Sgr A* allowing Schödel et al. (2002) to approximate a Keplerian orbit and to measure the enclosed dark mass down to a distance of ~ 0.6 mpc from Sgr A*, leaving the SMBH as the only plausible explanation. Also, the high radial velocity of the star S1 indicates that it must be on an $e \sim 0.97$ orbit with a semi-major axis exceeding $1''$. The findings by Ghez et al. (2003) and Schödel et al. (2003) suggested that some S-stars originally formed in one of the two starburst rings/disks at $1-5''$ from Sgr A* and were subsequently driven into highly elliptical orbits connecting to the innermost regions of the Galaxy (Cuadra, J. 2003, Subr & Karas 2005).

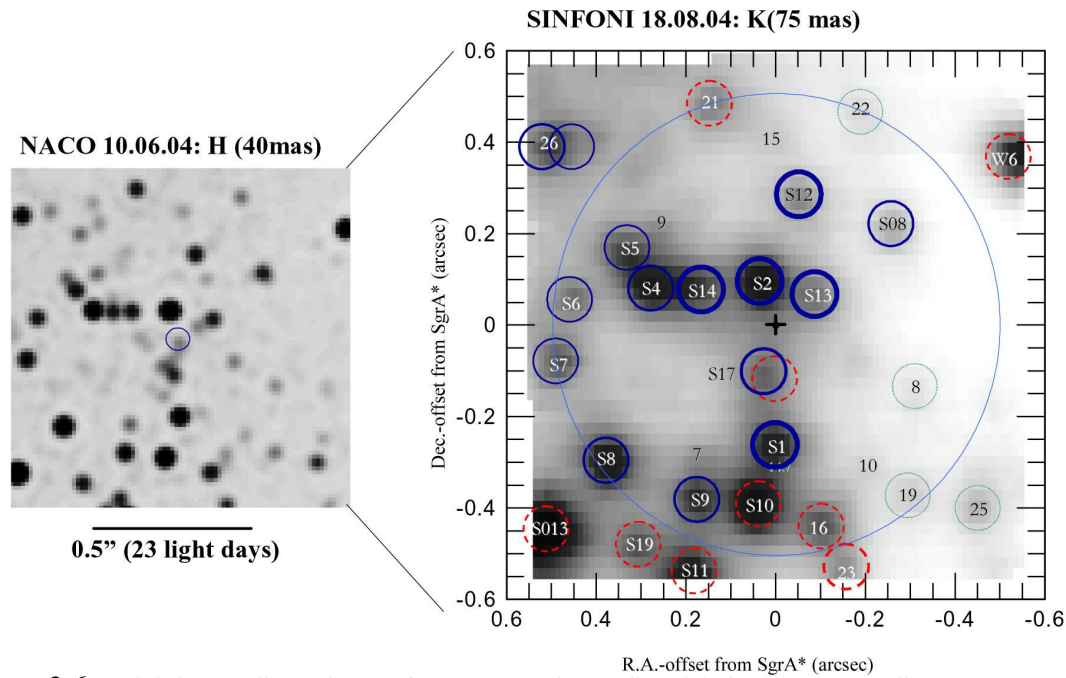


Figure 3.6: **NACO and SINFONI H/K-images of The Sgr A* Cluster - The S-stars** Left: NACO H-band image (Lucy cleaned and re-convolved to 40 mas resolution) taken on June 10th, 2004. The color scale is logarithmic. The magnitude difference between the faintest and brightest stars in the image is about 4.4 mag and the faintest stars in the image have $K \sim 17.8$. The position of the SgrA* is indicated by a circle. Right: K-band image constructed from all of the SINFONI data from August 18/19th, 2004 by collapsing the data cube in spectral dimension (grey scale is logarithmic). The spatial resolution of the SINFONI images is 75 mas FWHM and the Strehl ratio is about 10%. All $K < 17$ stars visible in the SINFONI image (and the NACO image) are marked by a circle, along with their identification (Schödel et al. 2003). The form and thickness of each circle encodes the spectral identification (continuous: early type, dashed: late type, thin dotted: uncertain but not late type) and proper motion velocity. Early and late type stars with proper motions $> 1000 \text{ km s}^{-1}$ are marked by thick circles, stars with proper motions between 500 and 1000 km s^{-1} by medium thick circles and stars with proper motions $< 500 \text{ km s}^{-1}$ by thin circles (Eisenhauer et al. 2005).

The statistical inference mentioned above, together with the direct derivation of semi major axes of less than 10 mpc for the six stars in the inner cusp whose orbits were solved (Ghez et al. 2003, Schödel et al. 2003), suggests that the Sgr A* cluster as a whole is tightly bound to the black hole. The orbital planes of those stars, as far as they are constrained by the current data, are significantly different from the two disk planes of the early-type stars (see section 3.2). For instance, S2 has a clockwise angular momentum, but its orbital plane is 70 off the plane of the clockwise early-type stars. Levin & Beloborodov (2003) have commented that such large offsets may be explained by relativistic Lense-Thirring precession of a star originally in the same plane as the stars farther out.

3.3 Sagittarius A*

The investigation of the dynamics of stars within the central cluster is a key for the investigation of the mass distribution in that area. Over the last decade, these investigations, as mentioned in section 3.2.3, have provided compelling evidence for the existence of a super-massive black hole (SMBH) at the centre of the Milky Way (Eckart & Genzel 1996, Genzel et al. 1997, 2000, Ghez et al. 1998, 2000, 2003, 2003b, Eckart et al. 2002a, Schödel et al. 2002, 2003). The central, compact, non-thermal radio source Sgr A* was initially discovered by Balick & Brown (1974). Its spectrum is only well known at radio to submm wavelengths and is remarkably faint in all other wavebands. Although there appears to be plenty of interstellar gas and dust available for accretion at the GC, Sgr A* radiates far below its Eddington luminosity (10^{-8} of the Eddington rate). It is unclear whether the feeble emission is due to a low accretion rate, inefficient angular momentum transport, low radiation efficiency, or a combination of these. The first unambiguous detection of Sgr A* at infrared wavelengths was only in 2003 (Genzel et al., 2003b). This pushed the understanding of the properties of Sgr A* towards theories of accretion of hot plasma onto a massive black hole, or alternatively ejection of plasma in a jet. Indeed, modelling the radio emission of Sgr A* showed that it must be produced by compressed, hot plasma in a steep potential well (see e.g. Melia & Falcke, 2001).

The observation of variable emission from Sgr A* is also a key element for the understanding of this compact object. The recently discovered X-ray flares of Sgr A* (Baganoff et al., 2001) are consistent with the origin of this hard radiation within about 10 Schwarzschild radii of a 3 - 4 million solar mass black hole (the Schwarzschild radius of a black hole of $4 \times 10^6 M_{\odot}$ is slightly less than 0.08 AU). Very long baseline interferometry (VLBA) showed, that Sgr A* is very compact, with an upper limit on its size of the order 1 AU (Krichbaum et al., 1998; Doleman et al., 2001). On the other hand, the absence of interstellar scintillation at 0.8 and 1.3 mm infer a lower limit of ~ 0.1 AU (Gwinn et al., 1991). A major result was also the discovery of interim-quiescent and flare activity from that position both in the X-ray and recently in the near-infrared wavelength domain (Baganoff et al. 2001, 2003, Eckart et al. 2003b, 2004b, Porquet et al. 2003, Goldwurm et al. 2003, Genzel et al. 2003b, Ghez et al. 2004). In particular, the discovery (Genzel et al. 2003b) of powerful NIR flares from Sgr A* improved the studies of the emission mechanisms. The IR flares occurred at the remarkable rate of 4 (± 2) times a day, at least twice the rate of X-ray flares detected by Chandra and XMM-Newton between 2000 and 2002. However, a remarkable property discovered in two of the brightest K-band flares is a quasi-periodic substructure with a period of 17 minutes. If this periodicity is a fundamental property of all flares, it most likely arises from the relativistic modulation of gas emission orbiting just outside the event horizon. In that case, the inevitable conclusion is that the Galactic Centre black hole has at least half of the maximum (Kerr) spin.

Eckart et al. (2004b) have recently reported on the first successful simultaneous NIR/X-ray campaign using NACO and Chandra as well as quasi-simultaneous mm-data from BIMA. Coincident with the peak of the about 6×10^{33} erg/s X-ray flare, a fading NIR flare of Sgr A* with > 2 times the interim-quiescent flux was detected. The event implies that the NIR/X-ray flare emission was coupled with a time lag not larger than 15 min and probably originated from the same ensemble of electrons. Compared to 8 h before the flare a 10% increased mm-flux density

Sagittarius A* Flare

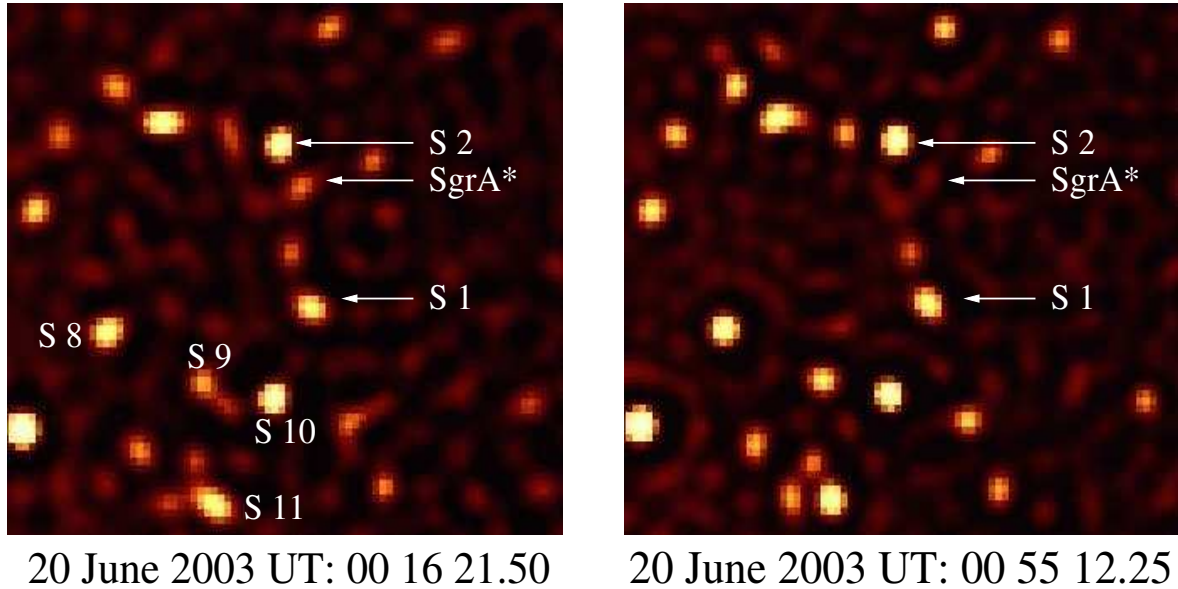


Figure 3.7: **Infrared variability of Sgr A***. Two characteristic images that demonstrate the infrared variability event described in Eckart et al. (2004b). This event was the first one to be detected simultaneously in the X-ray domain using Chandra. Shown is the average of eight Lucy-Richardson deconvolved and beam restored images taken at two different intervals. The universal times of the first image in each series are indicated in the panels. Sgr A* can be seen as a flaring source in the left panel. The field of view is $1.43''$ (72 light days) times $0.85''$ (43 light days).

was measured about 8 h after the event. The X-ray flares have similar durations as the IR-flares and some also do show minute-scale substructure. The reanalysis of the two most powerful ones in the framework of disk modes indicates high spin parameters as well (Aschenbach et al. 2003, 2004). The observational data obtained with NACO and Chandra in July 2004 is very much consistent with the previously obtained results.

Recently, Reid et al. (2004) improved earlier works by Backer & Sramek (1999) and Reid et al. (1999) on measurements of the proper motion, i.e. the motion projected onto the plane of the sky, of Sgr A* compared to extragalactic sources. They found that the motion of Sgr A* is consistent with the projection of the rotation of the sun around the GC. The intrinsic velocity of Sgr A* was found to be $18 \pm 7 \text{ km s}^{-1}$; it is, however, unclear whether or not the estimate of this component of the peculiar motion of Sgr A* differs significantly from zero and, if so, if this indicates a difference between the global and local measures of the angular rotation rate of the Galaxy. They also estimated the intrinsic motion of Sgr A* out of the plane of the Galaxy to be $-0.4 \pm 0.9 \text{ km s}^{-1}$ toward the north Galactic pole. Direct simulations of the motion of Sgr A*, owing to the gravitational forces of stars in random orbits within 2 pc of the Galactic centre yields a lower limit for the mass of Sgr A* of $4 \times 10^5 M_{\odot}$, Reid et al. (2004) adding

considerable weight to the claim that this object must be a massive black hole. More about such estimates applied on the 'inner cusp' region, which is the focus of this work, will be discussed in chapter 8.

Stars are ideal tracer particles for determining the shape of the gravitational potential in the GC because they are only subject to gravity but not to other large scale forces, such as forces produced by interstellar magnetic fields or winds. With high-resolution NIR speckle imaging observations, it became possible to measure, at the GC, stellar positions to within a few milli-arcseconds. Stellar proper motion velocities and accelerations were derived for the nuclear cluster (Eckart & Genzel, 1996, 1997; Ghez et al., 1998; Genzel et al., 2000; Ghez et al., 2000). This showed that the velocity dispersion varies with separation R from Sgr A* as $R^{-1/2}$, such as it is expected for particles on Keplerian orbits in the potential field of a point mass. This is in agreement with spectroscopic observations of line-of-sight velocities (e.g. Sellgren et al., 1990; Krabbe et al., 1995; Genzel et al., 1996). Measurements from gas and stellar dynamics showed that the enclosed dark mass is constant from distances of 1 pc down to 0.01 pc from Sgr A*. The location of the dark mass was determined using the observed accelerations of the innermost stars (Ghez et al., 2000; Eckart et al., 2002a). These dynamical measurements gave additional evidence that Sgr A* is a super-massive black hole of about $3 \times 10^6 M_{\odot}$. The possibility that the observed dark mass could be due to a compact cluster of dark astrophysical objects such as neutron stars or stellar mass black holes was excluded. This will be discussed in more details in chapter 4.

Chapter 4

Density and Mass distribution of the Central Stellar Cluster

The overall structure of the central stellar cluster can best be derived from diffraction limited NIR maps. Earlier, with lower spatial resolution and sensitivity, it was only possible to determine the structure of the cluster using the radial distribution of the light, the individual stellar components being undetectable separately. This led to wrong deductions. The strongest concentration of light being at the bright IRS16 complex, it was considered that Sgr A* could not be a super-massive black hole (Allen & Sanders 1986). However soon afterwards with the first high resolution speckle imaging techniques, (Eckart et al. 1992, Genzel et al. 2000) and later on with adaptive optics techniques (Genzel et al. 2003), it became evident that the highest stellar concentration is indeed around the super-massive black hole Sgr A*. Initial attempts of deriving the stellar distribution did not take into account that the cluster luminosity is completely dominated by a few dozen bright supergiants, which represent one component of an inhomogeneous distribution of various stellar populations. Therefore, for a better understanding of the structure of the stellar cluster, it is more appropriate to investigate the distribution of stars via their number density counts, assuming that the observed stars in the GC cluster can be used as tracers for the underlying fainter stellar components (Mouawad et al, 2004, 2005).

In this section it is described how with the present NIR imaging data described in chapter 2, it is possible to model the mass distribution function as close as a few milli-parsecs from Sgr A*. A surface density profile is fitted to number density counts and used, together with dynamical mass estimators, to deduce the 3 dimensional mass distribution function.

4.1 Number Density Counts

First coarse stellar number density counts were presented in Eckart et al. (1992). The data presented by Eckart et al. (1995) suggested an excess of stars above a flat core near Sgr A*. Another analysis based on three different data sets led to similar conclusions - a stellar cusp could be present around Sgr A* (Alexander et al. 1999) - this still remained somewhat inconclusive.

The most complete catalogue of stars in the central parsec was compiled by Genzel et al. (2000, 2003) and Schödel et al. (2003). Their sample included data from imaging with NACO at the VLT in 2002 which were two to three magnitude deeper than any previous image. Using these data, Genzel et al. (2003, see their Fig 7) obtained completeness corrected number density counts of stars in the central parsec by counting the sources in annuli with increasing radius around Sgr A*. They inferred a spatial number density of $n(r) \propto r^{-1.4}$ over the radial range $0.004 < r < 0.4$ pc. Their sample was 50% complete for stars brighter than $K \sim 18$, where completeness is defined as the percentage of stars in the field of view that are detectable and thus included in the sample. Expressed in terms of stellar mass, the sample is 50% complete for masses $m \gtrsim 3M_{\odot}$, assuming stars on the main sequence, a distance to the GC of 8.0 kpc (Reid 1993), and K-band extinction of 3.3 mag (Rieke & Paul 1989).

Presence of a stellar cusp

Here, I use the same K-band counts ($K \leq 18$) together with the earlier SHARP/NTT counts ($K \leq 15$), without taking into account in our study their H-band counts ($H \leq 19$). In contrast to the H-band counts carried out 'by-eye', the K-band counts, were determined by an automated procedure, they are therefore possibly less biased, and cover the whole range of the cluster, not only the central arc-second. Figure 4.1 shows the completeness corrected, binned stellar surface number density distribution for stars brighter than $m_K = 17$ as a function of projected distance from Sgr A*. Towards larger radii the NAOS/CONICA data was expanded with shallower ($K \leq 15$) number density counts of SHARP/NTT (see Genzel et al. 2000) that covers fields at larger distances from Sgr A*. In the overlap regions these counts were scaled for the best match with the deeper NAOS/CONICA data. Within ~ 2 arc-seconds of Sgr A*, these data indicate an excess of faint stars above the counts expected in a cluster with a flat core, as it had been already suggested earlier (Eckart et al. 1995; Alexander 1999).

The purpose of my work presented here is to study the distribution of mass that could be present in the vicinity of the central black hole using the orbital data available on the star S2. This task can be relatively much time consuming when integrating a considerable number of stellar orbits in the potential of the black hole and the stellar cusp. Therefore, in order to minimize this necessary computational time, the stellar density is fitted with an integrable model, which is in this case the Plummer model. The Plummer model resembles actual clusters with compact cores and an extended outer envelope (Spitzer 1975). While this model is not the one predicted by theoretical studies to form a stable configuration around a super-massive black hole - these predict the formation of power-law distributions which show a singularity at the centre - it, nevertheless, fits the data quite well and gives, within the uncertainties of the observations, equivalent characteristics as another power-law distribution fit to the data (see next paragraph).

In a Plummer model potential, the 3-dimensional radial density distribution $\rho(r)$ and the

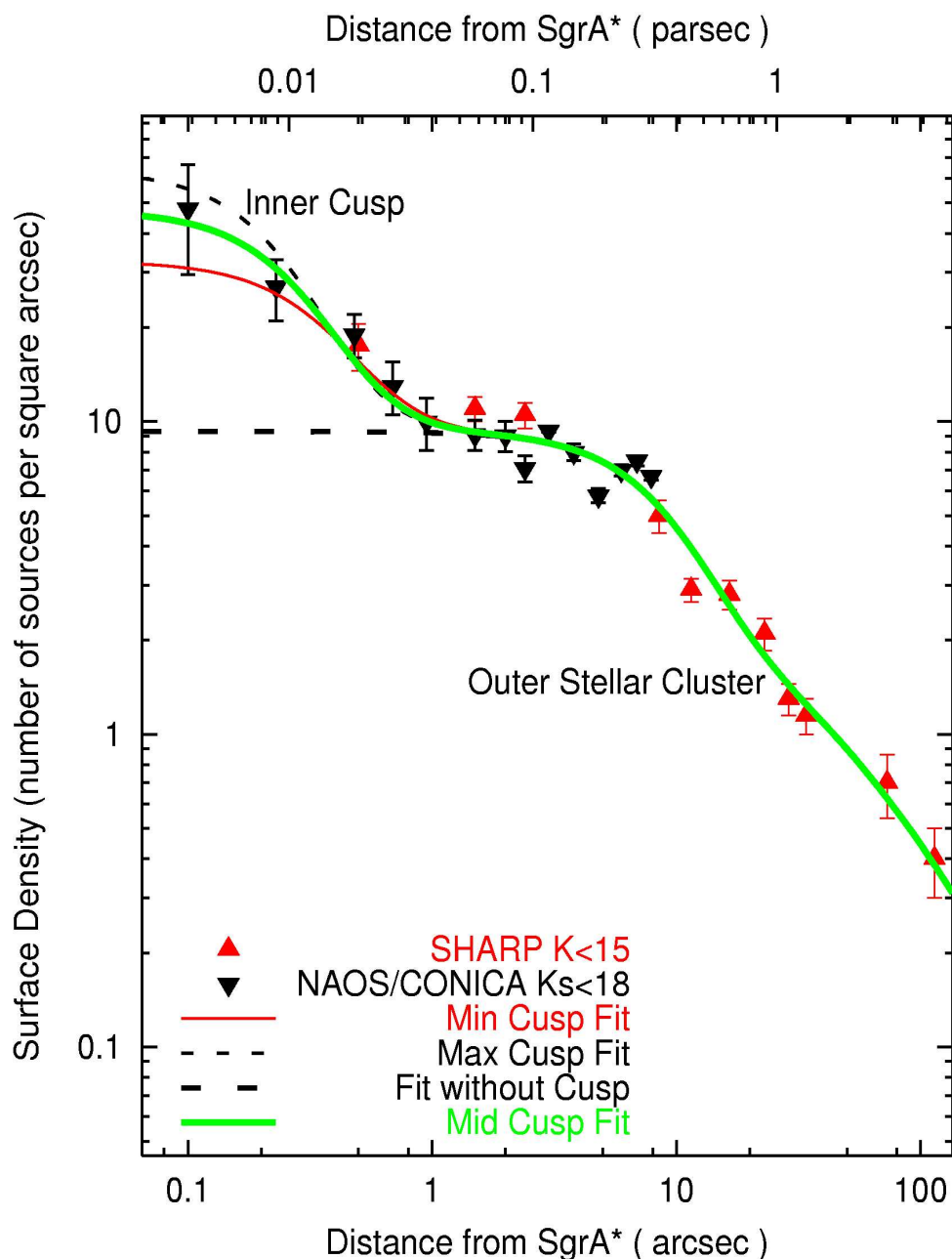


Figure 4.1: **Surface density of stars vs. distance from Sgr A*.** Surface density of stars vs. distance from Sgr A*. The downward pointing triangles represent the CONICA/NAOS data for $K_s \leq 18$, the upward pointing triangles are SHARP/NTT data for $K_s \leq 15$ stars scaled up by a factor of 5 in order to match the fainter CONICA/NAOS counts. The data are taken from Genzel et al. (2000, 2003). The long dashed line is the superposition of the 5 outermost Plummer models (see, Table 4.1). The addition of the innermost Plummer model (the 'inner cusp') gives the 'composite model'. It is represented by the 3 other curves, where the thick-straight line corresponds to the middle values of the 'inner cusp' parameters R_1 and M_1 , the thin-straight line to its lower values, and the short-dashed line to its upper values.

Table 4.1: **Parameters of the 'composite model'.** The parameters of the 'composite model' used to fit the GC stellar cluster. For each Plummer model we give the value of the core radius R_i (in arcsec and in parsec) deduced from the surface density plot. M_i is the corresponding total mass scaled to the enclosed mass distribution (Fig 8.3). M_i^{apo} is the contribution in mass inside a sphere which has a radius equal to the apo-astron of S2. ρ_i is the calculated average density in $M_\odot \cdot pc^{-3}$. The first Plummer model ($R_1 = 0.4''$ or $0.015 mpc$) corresponds to the "inner cusp" centred at Sgr A*. The addition of the remaining 5 models represents the density distribution of the outer stellar cluster.

i	R_i [arcsec]	R_i [pc]	M_i [M_\odot]	M_i^{apo} [M_\odot]	$\rho_i(0)$ [$M_\odot \cdot pc^{-3}$]
1	0.4	0.015	8540	1080	6.0×10^8
2	13	0.5	1.8×10^6	10	3.5×10^6
3	52	2.0	2.7×10^6	0.25	7.9×10^4
4	97	3.8	6.7×10^6	0.01	2.9×10^4
5	220	8.5	13.1×10^6	0.002	5.1×10^3
6	321	12.4	27.6×10^6	0.001	3.4×10^3

projected mass density $\sigma(r)$ are described by:

$$\rho(r) = \frac{3M}{4\pi R^3} \frac{1}{\left(1 + \frac{r^2}{R^2}\right)^{\frac{5}{2}}}, \quad (4.1)$$

$$\sigma(r) = \frac{4\rho(0)R}{3} \frac{1}{\left(1 + \frac{r^2}{R^2}\right)^2}, \quad (4.2)$$

where R is the core radius, M the total mass.

The modelling of the surface number density data consists of a superposition of several Plummer models. In total six Plummer models with different core radii and mass densities are superposed on top of each others. This model will be termed in the following as 'composite model', it is given in eq. 4.3 below:

$$\sigma(r) = \sum_{i=1}^6 \frac{M_i}{\pi} \frac{R_i^2}{(r^2 + R_i^2)^2}. \quad (4.3)$$

The parameters of the individual models are given in Table 1. The core radius of the smallest Plummer model is of ~ 15 mpc, whereas the one of the largest model is of ~ 12 pc. Fig 1 shows that the data can be described by a cusp centred on Sgr A* superposed on a larger-scale, isothermal-like cluster with a distinct break in between. The 'composite model' emphasizes a distinct break in the density profile at a radial distance of about 0.5 arcsecond.

Genzel et al. (2003) fitted a broken power-law to their stellar counts, with a distinct break at 10 arcsec. They showed that there exists a cusp centred at a position of $(\Delta \alpha, \Delta \delta) = (+0.09'', -0.15'')$ from Sgr A*, with an uncertainty of $\pm 0.2''$. The combination of the five outermost components of the 'composite model' gives a similar configuration as the flattened isothermal sphere of core radius ~ 0.3 pc derived by Genzel et al. (2003).

Fig 4.1 shows there exists a mini-core centred on Sgr A*, which is denominated by the 'inner cusp'. It is represented by the innermost Plummer model with a core radius $R_1 = 15.5 \text{ mpc} \cong 0.4''$. The density of the 'inner cusp' is a few hundred times larger than that of the next outer stellar cluster and it has a ~ 33 times smaller core radius (see Fig 8.1 and Table 4.1). The 'composite model' implies density values as high as $1.68 \times 10^8 \text{ M}_\odot \text{ pc}^{-3}$ at $0.1''$, and $1.54 \times 10^7 \text{ M}_\odot \text{ pc}^{-3}$ at $1''$. These values are comparable to the ones derived by Genzel et al. (2003) from a broken power-law density profile ($7 \times 10^8 \text{ M}_\odot \text{ pc}^{-3}$ at $0.1''$ and $3 \times 10^7 \text{ M}_\odot \text{ pc}^{-3}$ at $1''$).

The above description shows it is possible to fit number density counts with a mass density distribution. This implicitly means that a certain mass is asserted for each stellar component - equivalently a certain mass-to-light ratio (M/L) is also asserted. However for simplicity this was always considered to be constant and equal to the outer stellar cluster M/L. Thus, the above analysis critically depends on the assumption that the ratio of number counts to total stellar mass (most sources are faint and cannot be directly observed) is constant with separation and environment in the Galactic Center. However, this assumption is most likely not valid (see chapter 8). In the following chapters, this assumption is relaxed, and higher values of the mass-to-light ratio will be considered in the central regions.

4.2 Enclosed Mass

From a mass surface density distribution, it is possible to derive a 3-dimensional mass distribution $\rho(r)$ (see eq 4.1), as well as an integrated mass distribution $M(r)$ which represents for a distance r from the centre, the enclosed mass present inside the radius r . Similarly to eq 4.3, the mass distribution of the 'composite model' is given by

$$M(r) = \sum_{i=1}^6 \frac{M_i r^3}{(r^2 + R_i^2)^{3/2}}. \quad (4.4)$$

This integrated mass distribution does only give meaningful values if it is tied to dynamical masses estimated at different radii. There exist a number of dynamical mass estimators which will be described briefly in the next paragraph. A direct estimation of the mass from observations is given in Genzel et al. (1996), they give a dynamical stellar mass of 3.2, 8.4, and $27.3 \times 10^6 \text{ M}_\odot$ at distances $R = 1.9, 3.8,$ and 11 pc from Sgr A*. These numbers were estimated assuming a mass-to-light ratio, $M/L (2\mu\text{m})$ of $2 \text{ M}_\odot/L_\odot$.

4.2.1 Mass estimators

Virial and Bahcall-Tremaine mass estimators

Possibilities to estimate the dark mass is via the virial theorem (M_{virial}), or by using the projected Bahcall-Tremaine mass estimators (M_{BT}) as given by Bahcall & Tremaine (1981) (see also, e.g. Genzel et al. 1996):

$$M_{\text{virial}} = \frac{3\pi}{2G} \frac{\sum_i w(i) v_i^2}{\sum_i w(i)/p_i} \quad (4.5)$$

and

$$M_{BT} = \frac{16}{\pi G \sum_i w(i)} \sum_i w(i) p_i v_i^2 \quad (4.6)$$

Here p_i is the projected radius of the star i at radius r_i , $w(i)$ are weighting factors, and v_i a one-dimensional velocity such as spectroscopically measured line of sight velocities. Both estimators assume a homogeneous distribution of the stars. The virial theorem assumes additionally an isotropic velocity field. The specific form of the Bahcall-Tremaine (BT) mass estimator presented here, assumes that the stars are on isotropic orbits which are dominated by a central mass.

The Leonard-Merritt estimator

Assumptions on isotropy of the cluster are not always met at the Galactic Centre. In the inner regions of the Sgr A* cluster, there exist anisotropies (see chapter 3). In this case, a more appropriate estimator would be the Leonard-Merritt (LM) estimator (Leonard & Merritt 1989) which is independent of any assumptions about isotropy. It can be constructed from the tangential and radial projections of the two-dimensional proper motion velocity, v_T and v_R , and can be written as follows:

$$\langle M(r) \rangle = \frac{16}{\pi G} \langle R(\frac{2}{3}v_R^2 + \frac{1}{3}v_T^2) \rangle \quad (4.7)$$

In this work we use the LM mass estimates as derived by Ott (2003). These used the proper motion data including the NACO data 2002.

The Jeans Method

A more powerful method to estimate a dynamical mass $M(r)$ enclosed at a distance r is, however, the Jeans method. It is free from assumptions on both isotropy and a dominating central mass. The Jeans equation can be derived from the collisionless Boltzmann equation

$$\frac{\partial f}{\partial t} + v \nabla f + \nabla \Phi \frac{\partial f}{\partial v} = 0 \quad (4.8)$$

with

$$f = f(t, r, v)$$

being the phase-space density of stars.

In this equation, v and r represent respectively the 3-dimensional velocities and separations from the centre. In a gravitational potential $\Phi(r)$, and for a spherical stellar distribution $n(r)$ with velocity dispersions in Φ and θ directions

$$\sigma_\Phi^2(r) = \sigma_\theta^2(r) \quad (4.9)$$

and assuming

$$\frac{\partial f}{\partial t} = 0$$

(no creation or destruction of stars), one finds

$$\Phi_r = \frac{GM(r)}{r} = v_{rot}^2(r) - \sigma_r^2(r) \left(\frac{d \ln(n(r))}{d \ln(r)} + \frac{d \ln(\sigma_r^2(r))}{d \ln(r)} + 2\beta \right) \quad (4.10)$$

It is then possible to estimate the enclosed mass $M(r)$ in a radius r as a function of v_{rot} , σ_r , n_r , and β . Here, v_{rot} accounts for a systematical rotation of the cluster. The anisotropy parameter, β , can be written as a function of the radial and tangential velocity dispersion, but also as a function of the proper motions v_T and v_R

$$\beta = 1 - \frac{\sigma_\theta^2(r)}{\sigma_r^2(r)} = \frac{3(\langle \sigma_R^2 \rangle - \langle \sigma_T^2 \rangle)}{3\langle \sigma_R^2 \rangle - \langle \sigma_T^2 \rangle} \quad (4.11)$$

The velocity dispersion $\sigma_r(r)$ and densities of stars $n(r)$ as a function of radius are connected to the projected velocity dispersion $\sigma_r(p)$ and the observed surface density $\Sigma(p)$ as a function of projected separation p via the Abel integral equations:

$$\Sigma(p) = 2 \int_p^\infty \frac{n(r)}{(r^2 - p^2)^{1/2}} dr \quad (4.12)$$

$$\Sigma(p)\sigma_r^2(p) = 2 \int_p^\infty \frac{n(r)\sigma_r^2(r)r}{(r^2 - p^2)^{1/2}} dr \quad (4.13)$$

These integral equations can now be used to perform a χ^2 fit of parameterized models for $n(r)$ and $\sigma_r(r)$ to the actually measured projected data $\Sigma(p)$ and $\sigma_r(p)^2$ (see discussion in Kormendy & Richstone 1995; Genzel et al. 1996). The used parametrized models are

$$n(r) = \frac{n_0}{1 + (r/r_0)^\alpha} \quad (4.14)$$

$$\sigma_r(r)^2 = \sigma(\infty)^2 + \sigma(r_{ref}^2(r/r_{ref}))^{-2\phi} \quad (4.15)$$

Here the central stellar density n_0 is estimated from the projected quantities via $n_0 = \Sigma_0/p_0$, with r_0 and the projected quantity p_0 being related to the core radius of the cluster. ϕ is a modelling parameter. $\sigma(r_{ref})$ is the velocity dispersion of the cluster at reference distance from the centre of about 0.4 parsec, and $\sigma(\infty)$ the velocity dispersion of the bulge at large distances from the centre. A detailed description of the calculation of $n(r)$, $\sigma(r)$ and $M(r)$ is given in Genzel et al. (1996) and Eckart & Genzel (1997).

In this work, we use mass estimates of the Jeans model as estimated in Genzel et al. (2000).

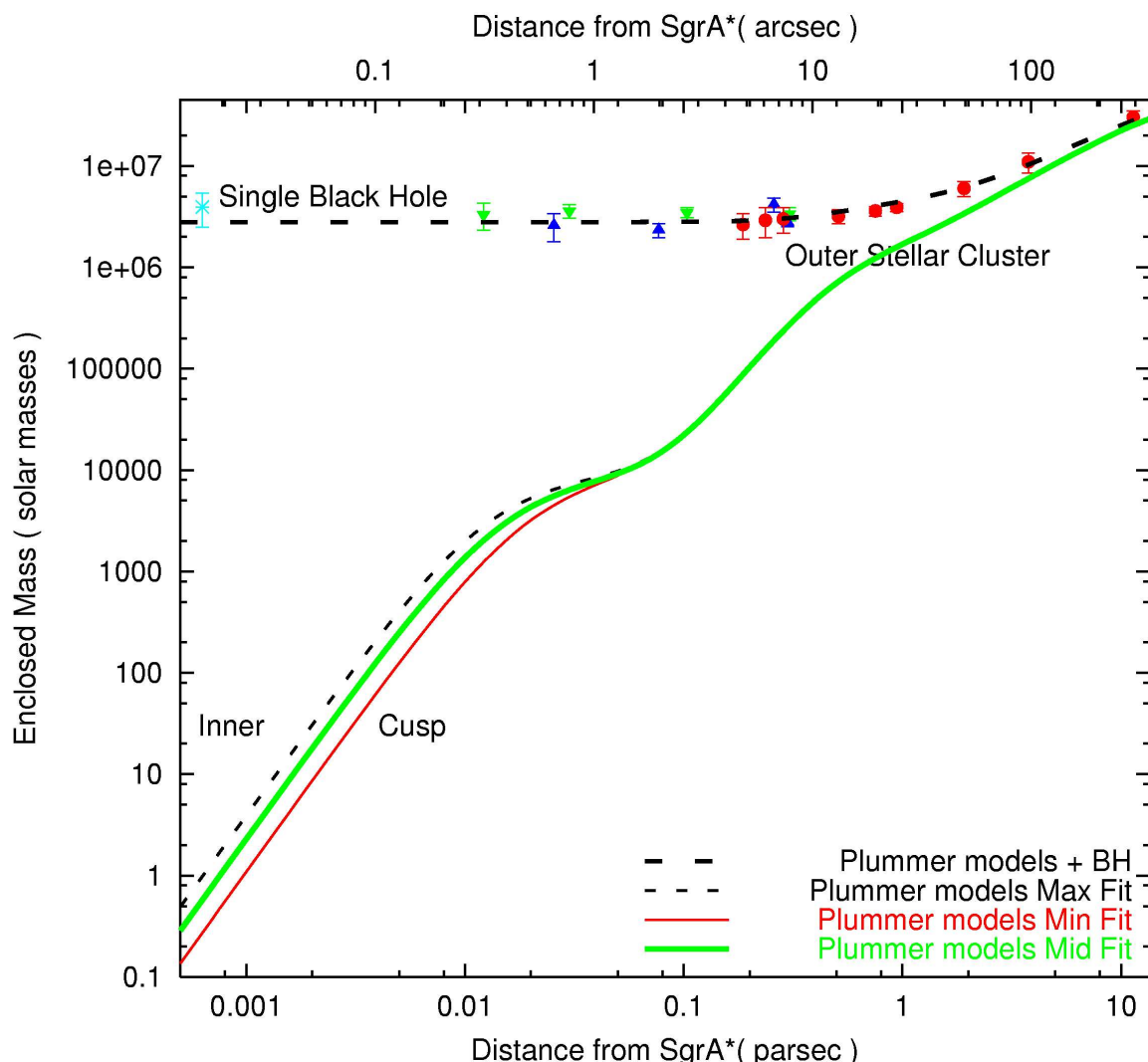


Figure 4.2: **Mass distribution in the central 10 pc of the Galactic Centre.** *Mass distribution in the central 10 pc of the Galactic Centre for an 8 kpc distance (Reid et al. 2003; Eisenhauer et al., 2003). Filled circles are mass estimates from a parameterized Jeans-equation model of the radial velocities of late type stars, assuming isotropy (Genzel et al. 2000). Filled downward-pointing triangles denote Leonard-Merritt projected mass estimators from a new NTT proper motion data set (Ott 2003). The star point denotes the mass derived from the orbit of S2. The error bar combines the orbital fit and astrometry errors (Eisenhauer et al. 2003). The long dashed line is a fit to the measured enclosed mass against distance. That results from a combination of the mass distributions deduced from the 'composite model' fit to the stellar cluster, plus a $2.9 \pm 0.3 \times 10^6 M_{\odot}$ black hole. The same model without a point mass is represented by the 3 other curves, they correspond to acceptable models of the stellar cluster within the error bars.*

The integrated mass distribution

The calibration of the enclosed mass, $M(r)$, only relies on a solid measure of the central mass (within 0.001 pc from SgrA*) derived from the Keplerian orbit of the star S2 and mass estimates of the entire stellar cluster at distances of several parsecs from the centre. At these large radii the published results of all different statistical mass estimators give very consistent results within uncertainties that are fully acceptable for this study (Eisenhauer 2003, Genzel et al. 2000, Serabyn & Lacy 1985; Güsten et al. 1987; Lacy et al. 1991; Herbst et al. 1993; Roberts & Goss 1993). By tying the mass modelling as a function of radius to the stellar number density distribution, it does not depend on possible anisotropies of the velocity field at radii of less than a parsec. It is only there where the anisotropies are apparently present at a considerable level (Genzel et al. 2000, Schödel et al. 2003). In particular, it is worth to point out that the fitting is not being done to enclosed mass estimates at these small radii. In Fig 2 these are only shown for completeness. The only assumption that is considered is that of a constant M/L ratio as a function of distance. This assumption is relaxed and discussed in the chapter 8 of this thesis.

Equation 4 derived for the 'composite model' of the integrated mass distribution can be scaled and fitted to the dynamical mass estimates vs. distance as they were described above. Figure 4.2 shows the compilation of these various mass estimates as derived by Genzel et al. (2000), Ott (2003), and Eisenhauer et al. (2003). The best obtained fit to these dynamical mass estimates corresponds to a $2.9 \times 10^6 M_{\odot} \pm 0.3 \times 10^6 M_{\odot}$ black hole plus the mass distribution of equation 4.4, of which the 6 total masses M_i , are listed together with their corresponding densities, ρ_i , in Table. 4.1. The resulting compact mass value is in good agreement with the value of $3.6 \pm 0.6 \times 10^6 M_{\odot}$ based on the orbit of S2 as recently derived by Eisenhauer et al. (2003) and (again based on S2) confirmed in chapter 7. An offset in the value of the enclosed compact mass will not influence our modelling significantly because the shape and mass of the 'composite model' depends primarily on the profile of the stellar number counts.

In Figure 4.2 the long-dashed line corresponds to the best fit, the thick-straight line shows only the enclosed mass without a BH obtained with the 'composite model' of the extended cluster. The thin-straight and the short-dashed lines represent the above discussed extreme cases of an inner cusp radius. The limits on the core radius, R_1 , of our model, deduced from the error bars on the number density counts, are found to be 13.2 mpc for the lower value R_1^{min} , and 20.2 mpc for the upper one R_1^{max} , with total cluster mass of $M = 8540_{\odot}$ and $M = 8820_{\odot}$ respectively. Note that these errors result from the uncertainties of the stellar number counts at the smallest distances to Sgr A* (Fig 4.1).

The orbit of S2

With an apo-centre of approximately 9 mpc (Schödel, 2004; Ghez et al., 2003), the star S2 orbits in a region inside the core radius ($R_1 \sim 15$ mpc) of this innermost model. Therefore its path can be mainly influenced, in addition to the BH potential, by the 'inner cusp' gravitational potential (see column 5 in Table 4.1). At these distances from the centre, the present number density counts have large error bars ($R_1^{min} = 13.2 \text{ mpc} \leq R_1 \leq R_1^{max} = 20.2 \text{ mpc}$, see Fig 4.1). Varying the mass, M_1 , of the central Plummer model component, for values beyond the estimated error, allows to study cases in which the mass-to-light ratio, M/L , varies as a function of distance

from Sgr A*. As described in Chapter 5 and Chapter 6, exploring the possible ranges for R_1 and M_1 that fulfill the constraints given by the orbital measurements of the star S2 allows to place valuable constraints on the amount of cusp mass and on the influence of the cusp structure and size.

Chapter 5

A High Accuracy Integrator

In non-point mass potentials, one needs to trace numerically the trajectory of the orbiting objects. If there exists, like assumed here for the case of the GC, a point mass plus possibly an extended mass distribution, the star at the centre will orbit in the potential of both the point mass and the fraction of the integrated mass which is seen under its radius. When the extended mass forms a spherically symmetric distribution, the trajectory of the star will follow a Rosetta-shaped orbit - unclosed orbits showing a shift of the peri-centre or rotation of the major axis (see Chapter 6).

In the case of the Galactic Centre, the amount of extended mass hidden in the centre is unknown. The major part of this work is to study the structure and content of this hypothetical mass. This is performed by studying the trajectory of the star S2 which is orbiting the central mass, and for which proper motion data and radial velocities are available. The approach used in the work to investigate this trajectory, is to integrate its orbit and fit it to the measured time-dependent positions and velocities. For this purpose, a high accuracy integrator is needed. A fourth order Hermite integrator was chosen, it is derived from the one used in high-accuracy N -body simulations (Aarseth 1999, Spurzem 1999). The advantage of the Hermite scheme is that it allows a fourth order accurate integration based on only two time steps. Therefore it requires the analytic computation of the time derivative of the gravitational force. The trajectory of S2 was computed around the BH and through the extended mass as given by the 'composite model' (see equation 4.4). In section 5.1 a detailed explanation of the Hermite scheme is given, it is based on Makino & Aarseth (1992), for a more detailed introduction, see also Aarseth (2003). Section 5.2 is an overview of the developments which were included to the code in order to accomplish these purposes.

5.1 The Hermite Integrator: An individual timestep scheme

The Hermite scheme is a multi-step fourth-order predictor-evaluate-corrector (PEC) scheme. In this scheme the acceleration and its time derivative are calculated analytically. They are then used to construct the interpolation polynomials of the force. It allows individual time-steps – different time-steps for the individual particles (Aarseth 1963, 1985, 2003). By the iteration of the evaluation and correction steps, the Hermite scheme becomes a time-symmetric integrator

that shows no secular errors in the semi-major axis and the eccentricity for the integration of a two-body Kepler problem with a constant time-step. The fourth order scheme has a very important advantage: it can be implemented as a self-starting scheme.

Here we describe the fourth-order Hermite scheme in detail as given in Makino & Aarseth (1992) and Aarseth (2003).

5.1.1 Algorithmic aspects

In the Hermite individual time-step scheme, each particle i has its own time t_i , timestep Δt_i , position \mathbf{x}_i , and velocity \mathbf{v}_i at time t_i , and acceleration \mathbf{a}_i and time derivative of the acceleration $\dot{\mathbf{a}}_i$ calculated at time t_i . The advantage of the individual timestep scheme is that one can assign different timesteps to different particles. A shorter time step is adjusted for particles coming close to each others (therefore needing a higher resolution of the paths), whereas it is kept long for the other particles. The integration proceeds according to the following steps:

- 1 Select particle i with a minimum $t_i + \Delta t_i$. Set the global time t to be this minimum, $t_i + \Delta t_i$.
- 2 Predict the positions and the velocities of all particles at time t using \mathbf{x} , \mathbf{v} , \mathbf{a} and $\dot{\mathbf{a}}$.
- 3 Calculate the acceleration \mathbf{a}_i and its time derivative $\dot{\mathbf{a}}_i$ for particle i at time t , using the predicted positions and velocities.
- 4 Calculate $\mathbf{a}_i^{(2)}$ and $\mathbf{a}_i^{(3)}$ using a Hermite interpolation based on \mathbf{a} and $\dot{\mathbf{a}}$. Add the corrections to the position and velocity of particle i . Calculate the new timestep and update t_i
- 5 Go back to step (1).

In step (2), the positions and the velocities are predicted. The latter are used to calculate $\dot{\mathbf{a}}$.

5.1.2 Computational aspects

Assume a set of N particles with positions $\mathbf{x}_i(t_0)$ and velocities $\mathbf{v}_i(t_0)$ ($i = 1, \dots, N$), given at time $t = t_0$, and let us look at a selected test particle at $\mathbf{x} = \mathbf{x}_0 = \mathbf{x}(t_0)$ and $\mathbf{v} = \mathbf{v}_0 = \mathbf{v}(t_0)$. Here and in the following, the index i for the test particle i and also occasionally the index 0 indicating the time t_0 will be dropped for brevity; sums over j are to be understood to include all j with $j \neq i$, since there should be no self-interaction. Accelerations \mathbf{a}_i and their time derivatives $\dot{\mathbf{a}}_i$ are calculated explicitly:

$$\mathbf{a}_i = \sum_j Gm_j \frac{\mathbf{R}_{ij}}{(R_{ij}^2 + \epsilon^2)^{3/2}} \quad ; \quad \dot{\mathbf{a}}_i = \sum_j Gm_j \left[\frac{\mathbf{V}_{ij}}{R_{ij}^3} - \frac{3(\mathbf{V}_{ij} \cdot \mathbf{R}_{ij})\mathbf{R}_{ij}}{(R_{ij}^2 + \epsilon^2)^{5/2}} \right], \quad (5.1)$$

where ϵ is the softening parameter. It is included to all inverse R terms in order to reduce effects of close encounters. and

$$\mathbf{R}_{ij} = \mathbf{x}_{p,j} - \mathbf{x}_{p,i} \quad ; \quad \mathbf{V}_j = \mathbf{v}_{p,j} - \mathbf{v}_{p,i} \quad ; \quad R_{ij} = |\mathbf{R}_{ij}| \quad ; \quad V_{ij} = |\mathbf{V}_{ij}|$$

By low order predictions,

$$\mathbf{x}_{p,j} = \frac{(t - t_j)^3}{6} \dot{\mathbf{a}}_j + \frac{(t - t_j)^2}{2} \mathbf{a}_j + (t - t_j) \mathbf{v}_j + \mathbf{x}_j \quad (5.2)$$

and

$$\mathbf{v}_{p,j} = \frac{(t - t_j)^2}{2} \dot{\mathbf{a}}_j + (t - t_j) \mathbf{a}_j + \mathbf{v}_j, \quad (5.3)$$

where j runs through all the particles, including particle i . Since $\dot{\mathbf{a}}_j$ is calculated directly, all quantities used in the predictor are obtained by direct calculation, rather than by interpolation. The corrector is based on the third-order Hermite interpolation constructed from \mathbf{a} and $\dot{\mathbf{a}}$ at times t_i and $t_i + \Delta t_i$. The third-order Hermite interpolation polynomial is obtained from the Taylor series using higher derivatives of \mathbf{a} at $t = t_0$:

$$\mathbf{a}_i(t) = \mathbf{a}_{0,i} + \Delta t \dot{\mathbf{a}}_{0,i} + \frac{\Delta t^2}{2} \mathbf{a}_{0,i}^{(2)} + \frac{\Delta t^3}{6} \mathbf{a}_{0,i}^{(3)} \quad ; \quad \dot{\mathbf{a}}_i(t) = \dot{\mathbf{a}}_{0,i} + \Delta t \dot{\mathbf{a}}_{0,i}^{(2)} + \frac{\Delta t^2}{2} \mathbf{a}_{0,i}^{(3)}, \quad (5.4)$$

where $\Delta t = t - t_i$, \mathbf{a}_0 and $\dot{\mathbf{a}}_0$ are the acceleration and its time derivative calculated at time t_i . If $\mathbf{a}_{0,i}$ and $\dot{\mathbf{a}}_{0,i}$ are known from direct summation (From equation 2.1, using the predicted positions and velocities), one can invert the equations above to determine the unknown higher order derivatives of the acceleration at $t = t_0$ for the test particle:

$$\mathbf{a}_{0,i}^{(2)} = \frac{-6(\mathbf{a}_{0,i} - \mathbf{a}_{1,i}) - \Delta t_i(4\dot{\mathbf{a}}_{0,i} + 2\dot{\mathbf{a}}_{1,i})}{\Delta t_i^2} \quad (5.5)$$

and

$$\mathbf{a}_{0,i}^{(3)} = \frac{12(\mathbf{a}_{0,i} - \mathbf{a}_{1,i}) + 6\Delta t_i(\dot{\mathbf{a}}_{0,i} + \dot{\mathbf{a}}_{1,i})}{\Delta t_i^3}, \quad (5.6)$$

where $\mathbf{a}_{1,i}$ and $\dot{\mathbf{a}}_{1,i}$ are the acceleration and its derivative at time $t_i + \Delta t_i$. The correction formulae for the position and the velocity are expressed as

$$\mathbf{x}_i(t_i + \Delta t_i) = \mathbf{x}_{i,p} + \frac{\Delta t_i^4}{24} \mathbf{a}_{0,i}^{(2)} + \frac{\Delta t_i^5}{120} \mathbf{a}_{0,i}^{(3)} \quad (5.7)$$

and

$$\mathbf{v}_i(t_i + \Delta t_i) = \mathbf{v}_{p,i} + \frac{\Delta t_i^3}{6} \mathbf{a}_{0,i}^{(2)} + \frac{\Delta t_i^4}{24} \mathbf{a}_{0,i}^{(3)}. \quad (5.8)$$

For a given energy error, the Hermite scheme allows timesteps which are larger by some factor of order unity depending on the parameters of the system under study. The Hermite scheme has been commonly adopted during the past years (Aarseth 1999, Aarseth 2003), because it

needs less memory and allows slightly larger timesteps. The timestep is given following the empirical standard formula (Aarseth 1985). It is expressed as:

$$\Delta t_i = \sqrt{\eta \frac{|\mathbf{a}_{1,i}| |\mathbf{a}_{1,i}^{(2)}| + |\dot{\mathbf{a}}_{1,i}|^2}{|\dot{\mathbf{a}}_{1,i}| |\mathbf{a}_{1,i}^{(3)}| + |\mathbf{a}_{1,i}^{(2)}|^2}}, \quad (5.9)$$

where η is a parameter that controls the accuracy. The error in the force calculation is controlled by the choice of η , which in the majority of the cases is taken between 0.01 and 0.04. The values of $\mathbf{a}_{1,i}$ and $\dot{\mathbf{a}}_{1,i}$ are already known, since they were directly calculated. The value $\mathbf{a}_{1,i}^{(3)}$ is the same as that of $\mathbf{a}_{0,i}^{(3)}$, because a third order interpolation is used. The second order derivative, $\mathbf{a}_{1,i}^{(2)}$ is calculated as

$$\mathbf{a}_{1,i}^{(2)} = \mathbf{a}_{0,i}^{(2)} + \Delta t_i \mathbf{a}_{0,i}^{(3)}. \quad (5.10)$$

However, when starting the time integration these higher order terms are not available. These can be calculated explicitly and then used to determine the timestep following Aarseth (1985). It is also possible to use a special formula (Makino & Aarseth 1992) for the initial timestep

$$\Delta t = \eta \frac{|\mathbf{a}|}{|\dot{\mathbf{a}}|} \quad (5.11)$$

which is as well implemented in the Hermite integrator.

5.2 Development of the Code

The initial code was written by R. Spurzem (Recheninstitut ARI, Heidelberg), and was further developed within the framework of this thesis. The equations of motion were rewritten in a reference centred at the central black hole. The fourth-order Hermite integrator requires the analytic computation of the time derivative of the gravitational force. The equations of the 'composite model' were differentiated and implemented to the force calculation in the case of a Plummer model and a Power-law profile.

The input parameters are 3-D positions and 3-D velocities. The path of the orbit is integrated in both the potential of the black hole and the extended mass, which is considered as a smooth static potential. In this case, the gravitational force on a given star depends only on the enclosed mass within the radius corresponding to the position of the star. Only the Newtonian gravitational force is considered, relativistic effects are not considered as they don't enter in the scope of this work, the enclosed mass at radius r is $M = M_{BH} + M(r)$. For the case of the Galactic Centre, we assume that the proper motion of Sgr A* relative to the surrounding stars can be neglected, thus the potential of the extended mass is well centred on the central point mass, and held fixed throughout the integration process. This assumption is well realistic since radio interferometry observations of Sgr A* with respect to background quasars has established that after subtraction of the motions of Earth and Sun around the Galactic centre, the proper motion of Sgr A* is probably smaller than $\sim 18 \text{ km s}^{-1} \pm 7 \text{ km s}^{-1}$ in the plane of the Galaxy and

$\sim 0.4 \text{ km s}^{-1} \pm 0.9 \text{ km s}^{-1}$ toward the Galactic pole (Backer & Sramek 1999; Reid et al. 1999, 2004). This implies $V_{S_{GRA^*}} \sim 10^{-4} - 10^{-2} V_{S_2}$. Likewise, the uncertainty in the local standard of rest velocity ($\leq 10 \text{ km s}^{-1}$) can also be neglected at the present level of analysis (see Salim & Gould 1999). We assume that the stellar cluster is gravitationally bound to the black hole and that the velocity of the central object, which dominates by far the gravitational potential, is close to zero. We also assume that the stars act as ideal test particles, i.e. that the masses of the individual stars are negligible compared to the mass of Sgr A*. Since the K= 14 - 15 stars in the Sgr A* cluster are most probably O/B-type stars (Genzel et al., 1997; Eckart, Ott, & Genzel, 1999; Figer et al., 2000; Gezari et al., 2002; Ghez et al., 2003, Eisenhauer et al. 2005, submitted), with 10 to 20 solar masses ($m_{S_2}/M_{S_{GRA^*}} \sim 5 \times 10^{-6}$), that are orbiting a dark mass of several million solar masses, this assumption seems well justified.

The initial coordinates being x, y, z and v_x, v_y, v_z at t_0 , the 3-D acceleration is computed at the time $t = t_0 + \delta t$. The quadratic deviation of the computed orbit from each data point is computed at each time t_{data} corresponding to each epoch of observation of the data points. This gives the χ^2 value which is the goodness of fit of the orbit to the present data. Further on, the minimization scheme is implemented following a grid scheme for which a 6-level loop is implemented allowing for the variation of the 6 initial parameters giving at the end of each new orbital integration a new χ^2 value. The loop will end after a coverage of a wide parameter space, the lowest found χ^2 value will be held as for the best fitting orbit. A detailed description of this procedure is given in Chapter 6.

Chapter 6

Modelling of the S2 Orbit

6.1 Keplerian and Non-Keplerian Orbits

Stellar dynamics of a dense stellar cluster in the vicinity of a SMBH has always been a highly complex subject since it involves many physical processes (like mass formation, mass segregation, collisions, binary formation (mergers), mass evolution, relativistic effects, tidal forces, dense environment...). With the present observations on the Galactic Centre, it became possible for the first time to trace a quasi complete orbit of a star (S2) around the central black hole. Very close to the centre, the study of the orbiting stars is the most direct way of investigating the potential at these small scales since they are a direct response to the potential itself. Earlier works showed that it was possible to fit Keplerian orbits to the observed stellar positions of six different stars (Schödel et al 2003, Ghez et al. 2005). Only the case of the star S2, showing the shortest period and the smallest uncertainties, is studied in terms of non-Keplerian orbits in this work. In this chapter, a description of the method used in order to study the star S2 in terms of both Keplerian and non-Keplerian potentials is given the way approached by Mouawad et al. (2005).

6.1.1 Kepler's laws

Bodies on closed orbits repeat their path after a constant period of time. This motion is described by the empirical laws of planetary motion found by Johannes Kepler (1571-1630), which can be mathematically derived from Newton's laws. I put more emphasize on these laws, since they are applicable to the star S2 and it is for the first time that a massive black hole can be constraint by a single stellar orbit. They can be formulated as follows:

1. The orbit of a planet around the Sun is an ellipse, with the Sun in one of the focal points of the ellipse.
2. Law of equal areas in equal time: As the planet moves on its orbit, during a given amount of time, the line from the Sun to the planet sweeps a constant area of the orbital plane, regardless

of which part of its orbit the planet traces during that period of time. This means that the planet moves faster near its perihelion than near its aphelion, because at the smaller distance it needs to trace a greater arc to cover the same area.

3. The cube of the semi-major axis, a , is proportional to the square of the orbital period, T . In case $m \ll M$, where M is the mass of the central body such as the sun and m the mass of the orbiting test particle, e.g. a planet, the mass of the central body is given by the relation

$$M = \frac{4\pi^2 a^3}{GT^2} \quad (6.1)$$

where G is the gravitational constant.

6.1.2 Non-Keplerian motion

There exists only two types of central gravitational fields where bound particles move on closed orbits. These are the spherical Keplerian and harmonic potentials. In traveling from pericentre to apo-centre and back, the azimuthal angle ϕ increases by an amount

$$\Delta\phi = 2 \int_{r_{peri}}^{r_{apo}} \frac{\frac{M}{r^2} dr}{\sqrt{2m(E - U) - \frac{M^2}{r^2}}}, \quad (6.2)$$

where (r, ϕ) are the planar polar coordinates in which the centre of the attraction is at $r = 0$ and ϕ is the azimuthal angle in the orbital plane, r_{peri} and r_{apo} represent the closest and the furthest separations from the centre of force respectively. E and U are the total and potential energy respectively, M the total mass of the spherical system and m the mass of the particle (Binney & Tremaine 1987). In general, $\Delta\phi/2\pi$ will not be an integer number. Hence the orbit will not be closed. In this case, the trajectory will be indefinitely spanning an area between two circular boundaries determined by the inner radius r_{peri} and the outer radius r_{apo} (see Fig 6.1).

An a simplified way, the Newtonian orbital shift can be modelled by considering the case of a spherically symmetric mass distribution. One can assume that a given star can penetrate the extended mass distribution, and neglect any collisional interaction. The (Newtonian) gravitational force on a given star depends only on the enclosed mass within the radius corresponding to the position of the star. This is a consequence of the spherical symmetry of the considered mass distribution and applies as well to the Plummer distribution considered in this work. Therefore, as the star moves towards the centre of forces, the gravitational force and hence the curvature of the orbit is smaller than for the case in which the whole mass is concentrated within a radius smaller than the periastron radius of the stellar orbit. This leads to orbits with *retrograde* orbital shifts, that is, shifts in the *opposite direction* as compared to the relativistic orbital shift.

Jiang & Lin (1985) presented an analytical treatment of the orbits of a test particle which is allowed to enter into the inner region of a sphere with uniform matter distribution without collision. Only the Newtonian gravitational force was considered and the relativistic effect has been neglected. They found that the major axis precesses about an axis passing through the

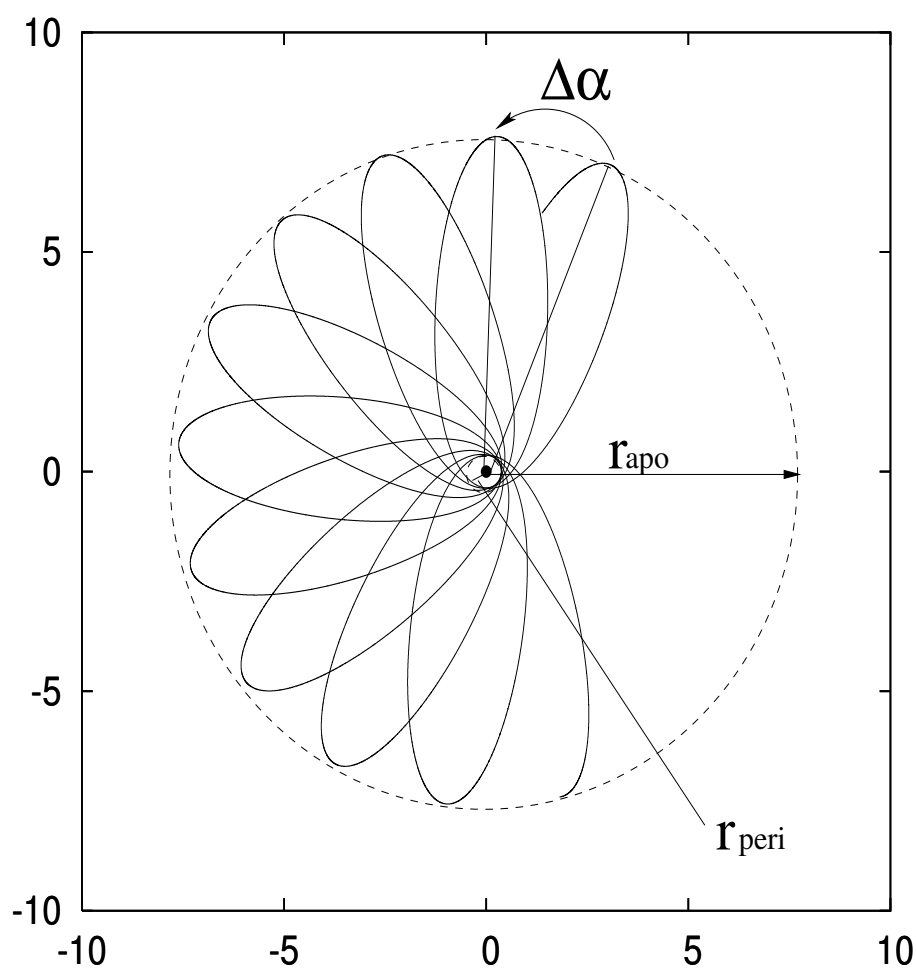


Figure 6.1: **Rosetta-shift Orbit.** Orbit showing rosetta shift in projection on the plane of the sky. The orbital shift, $\Delta\alpha$, is determined by the shift of the major-axis. The unclosed orbit will scan the area between the inner and the outer circle.

centre of the system and perpendicular to the plane of motion of the object. This finding can be generalized to any spherically symmetric distribution, and applies also for a Plummer potential.

Rubilar & Eckart (2001) studied the case of a Plummer model distribution around a SMBH in application to the GC, their results are given in chapter 8.

6.1.3 Orbital elements

Keplerian orbits

The trajectory of a test mass m bound in the gravitational field of a body of mass M , with $m \ll M$ can be described by seven orbital elements, (see Fig 6.2):

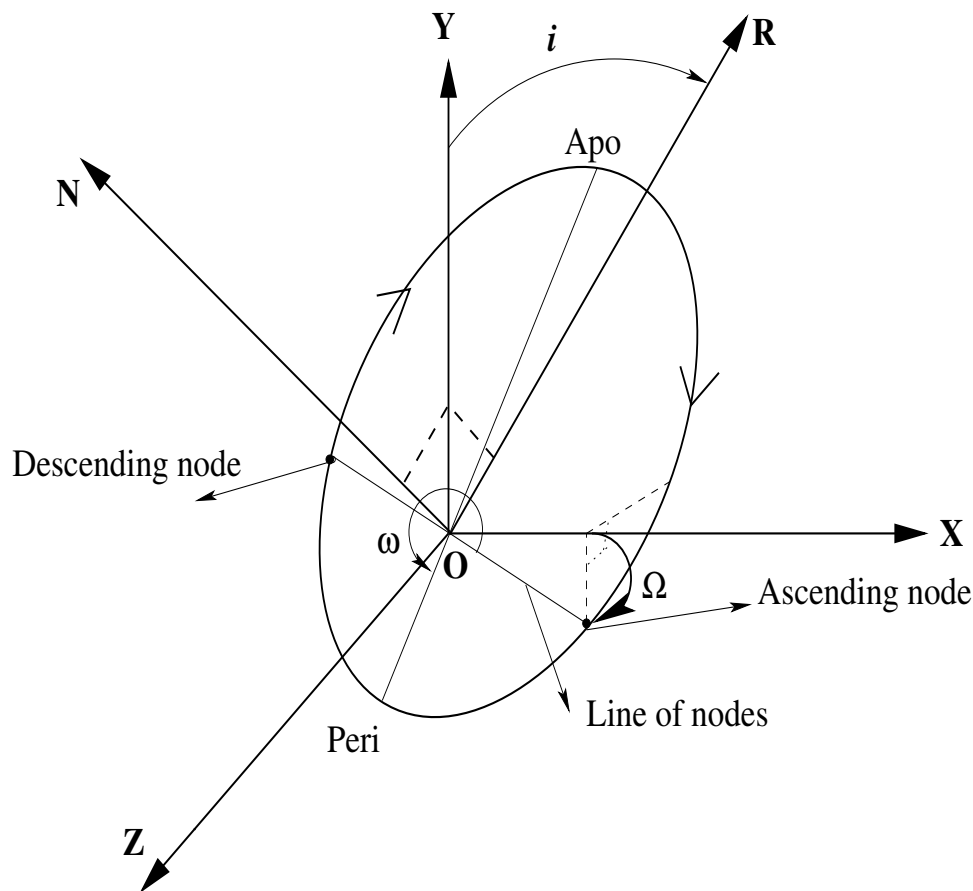


Figure 6.2: **Orbital elements in Space** Figure representing the orbital elements in space. The (XY) plane represents the plane of the sky, and the (Z) axis the line of sight. (N) is the vector normal to the orbital plane. (R) is present in the orbital plane. (N) , (Y) , and (R) belong in the same plane which is perpendicular to the orbital plane. The line of nodes defines the intersection between the plane of the sky and the orbital plane. The ascending and descending nodes are noted following the given direction of motion and direction of the orbit.

-The *period* P of the orbit, which is the time needed till the particle returns back to its initial location.

- The length of the *semi-major axis* a , which is half the distance between the *apo-centre* and the *peri-centre*.

- The *eccentricity* or ellipticity $0 < e < 1$ of the orbit.

- The time of *peri-centre passage*, T_{peri} .

- The *angle of the line of nodes*, $0 \leq \Omega \leq 180$. The line of nodes connects the two points of the orbit where it crosses the plane of the sky. The object moves toward the observer when it passes through the *ascending node*. The other node is called the *descending node*. Ω is usually defined east over north and corresponds to a rotation of the projected orbit on the plane of the sky. Changing Ω does not affect the shape of the projected orbit.

- The *angle from (ascending) node to peri-centre*, $0 \leq \omega \leq 360$. ω corresponds to a rotation

of the orbit within the orbital plane.

- The *inclination* $-90 \leq \mathbf{i} \leq 90$ is the angle between the plane of the orbit and the plane of the sky. It is measured *positive* when the northern part of the orbit lies *behind* the plane of the sky.

Rosetta-shaped orbits

The trajectory of a test mass m bound in the gravitational field of a central total mass M ($m \ll M$), composed of a point mass and an extended component of a **fixed radius**, will result in unclosed orbits known as Rosetta-shaped orbits. These can be defined by 8 orbital elements. We define them this way:

Five orbital elements, \mathbf{T}_{peri} , Ω , ω , \mathbf{i} , and the \mathbf{a} conserve the same definition as for the case of a Keplerian orbit, because the precession of the orbit occurs in the orbital plane, whereas for the other 3 elements we give the definition below:

- The *period* \mathbf{P} of the orbit, defined as the time between two consecutive apo-centre passage.
- The *eccentricity* or ellipticity $0 < \mathbf{e} < 1$ of the orbit, eccentricity of the equivalent closed Keplerian orbit between two consecutive apo-centre passages.
- The *peri-astron-shift angle*, $\Delta\alpha$ which is the precession angle of the major-axis per revolution. This angle depends on the amount of extended mass present within the radius determined by the position of the star.

6.1.4 Determination of orbital elements from positions and velocities

In the simulations, the initial parameters are the central mass and the 6 phase-space coordinates. Here, the correspondance between both, the orbital parameters and the phase-space coordinates, is given:

Eccentricity

The total energy and angular momentum of the orbiting particle are conserved. In the Keplerian case, another quantity is also conserved, that is the Laplace-Runge-Lenz-Vector, which is defined by:

$$\mathbf{A} = \mathbf{p} \times \mathbf{L} - Mk \frac{\mathbf{r}}{r}, \quad (6.3)$$

where \mathbf{p} and \mathbf{L} are the linear and the angular momentum respectively, M the central mass and k a constant. \mathbf{A} is in the direction of the radius vector of the peri-centre and has a magnitude $A = Mke$. For a Keplerian orbit, $e = A/Mk$ determines the eccentricity of the orbit. For a rosetta-shaped orbit, we use this same definition to define the eccentricity of the corresponding *closed* Keplerian orbit.

Inclination and angle of line of nodes

Geometrical considerations lead to the relations in equations 6.4 between the inclination and the angular momentum, as well as between the angle of line of nodes, Ω , and the angular momentum. It follows from the fact that the vector L lies in the direction of the normal to the orbital plane (Fig 6.1 above, for a detailed explanation see Sterne 1960), one can write:

$$\cos i = L_z/L \quad ; \quad \sin i \cos \Omega = -L_y/L. \quad (6.4)$$

Angle of the peri-astron-shift

The angle of the peri-astron-shift was estimated by looking for two successive apo-astron positions, i.e. points along the orbit having a maximum value of $|r|$. From these two points, the corresponding angular shift is finally computed. In principle, one could also compute the shifts using the newtonian angular integral for a spherically symmetric system (see equation 6.2).

The other 4 orbital elements, \mathbf{T}_{peri} , \mathbf{P} , ω and \mathbf{a} were calculated by a direct application of the definition.

6.2 The Method

In the Keplerian case, four observed positions at different epochs should be sufficient to fit an orbit to the data. This allows to derive accelerations which are necessary to compute the gravitational Newtonian force. However, the inevitable errors or uncertainties on the measurements make the determination of a unique orbit impossible. Earlier works (Ghez et al. 2000, Eckart et al. 2002) have shown such a behaviour. Practically, a good Keplerian fit of the S2 orbit was achieved for the first time with a meaningful accuracy, only when more than half of the orbit was observed (Schödel et al. 2002). More complex is the case of rosetta-shaped orbits, where more parameters are involved (extended mass fraction, mass distribution model and core radius). Especially, because bigger deviations from a Keplerian orbit occur closer to its apo-astron. In principle, at least three orbits of three different stars would be needed in order to determine the full mass distribution characteristics mentioned above (Rubilar & Eckart, 2001). For the moment, a simultaneous fit of multiple orbits as proceeded by Schödel et al. (2003), Ghez et al.(2005) and Eisenhauer et al. (2005) is possible just for Keplerian orbits at the centre of our Galaxy. In a non-Keplerian configuration, the star S2 is, presently, the only available candidate that can be studied.

Fitting the path of S2 to a Keplerian orbit allowed constraining the location of Sgr A* more precisely than the radio measurements (Ghez et al., 2003; Schödel et al., 2003; Eisenhauer et al., 2003). Additional spectroscopic information on line-of-sight velocities allowed for a geometric determination of the distance of Sgr A* from the solar system. This was possible because, for a fixed angular scale, the orbital periods are proportional to $R_0^{3/2} M_{bh}^{-1/2}$ and the radial velocities are proportional to $R_0^{1/2} M_{bh}^{-1/2}$ where R_0 is the heliocentric distance to the black hole and M_{bh} is its mass, the two parameters are not degenerate and can be determined independently (Eisenhauer

et al. 2003). Sufficient information on stellar orbits even allows determining upper limits on the motion of Sgr A* relative to the stellar cluster (see Ghez et al., 2005).

The results derived from the Keplerian fits on the distance to the Galactic Centre are used in this work, and the distance is held fixed throughout the fitting. In the case of *non-Keplerian* orbits, there are ten fit parameters in total - six orbital elements, the total central mass M_{tot} , the fraction f of the extended mass to the total mass M_{tot} , and the 2-dimensional position P of the central mass.

In the following, it is described how the fitting procedure was applied.

6.2.1 χ^2 minimization scheme

For a given observation epoch, the deviation of the computed curve from the observed data point was calculated, by applying the least square equation, namely the quadratic sum of the differences between observed and calculated values, weighted by the inverse of the variances. This definition of the χ^2 can be applied even if the errors on the measurements are not gaussian but as long as they are independent.

A minimum point in the χ^2 -surface can be either *global* or *local*. Finding a global minimum is, in general, a not a straight forward task. Two standard heuristics are widely used (Press et al. 1992): (i) find local minima starting from widely varying starting values of the independent variables, and then pick the most extrem of these (if they are not all the same); or (ii) perturb a local minimum by taking a finite amplitude step away from it, and then see if the routine returns to a better point, or always to the same one.

Many methods were developed for a variety of global extremization problems. We chose a simple direct method using the heuristic (i):

The chosen minimization method is a grid scheme. Its basis is to vary all n parameters on adequately spaced grids, thereby using each point in the n -dimensional grid as a set of starting values for the fitting routine. The output will be a n -dimensional surface of χ^2 values, where the valley of the minimum χ^2 will be clearly indicated. Although relatively expensive in computing time (time $\propto N^n$, N being the number of steps per parameter), this is a robust method which does not easily converge to local minima. In order to economize on the computing time, I performed a simplified approach by holding four parameters fixed. These are M_{tot} , f and $P(R.A., Dec.)$. This means, that for each set of chosen values of M_{tot} , f and P , the minimization grid scheme was applied to estimate the best orbital fit; practically to find the 6 parameters (being the orbital elements) which give the lowest χ^2 value. The 4 parameters, M_{tot} , f and P , were held fixed during each fitting procedure, they were, however, varied separately on a larger grid. Practically, for each set of those, a single fit was applied separately. In the section 6.2.3, it is shown how these parameters were varied.

In order to study the main effects of a varying cusp mass on the orbit of star S2, a representative coverage of these 4-D parameter space is investigated. It include the full range of possible scenarios. At the beginning, 6 values of total masses were chosen, 6 values for P , and 12 values for f . It was possible to form, for each position P , a 2-D χ^2 grid of M_{tot} vs. f (results are given in Fig 7.4), meaning six of such grids. Depending on each parameter, the number of values per

Table 6.1: **Characteristic $\tilde{\chi}^2_{tot}$ of the orbital fits.** The first column lists the obtained characteristic $\tilde{\chi}^2_{tot}$ for which the resulting orbits are considered to be fitting orbits. The 2nd column expresses the total non-reduced χ^2_{tot} for 33 degrees of freedom ($\tilde{\chi}^2_{tot} = \chi^2_{tot}/33$). When column 3 lists the deviation of the obtained χ^2_{tot} from the lowest obtained χ^2_{tot} , column 5 corresponds their resulting σ error bars.

$\tilde{\chi}^2_{tot}$	χ^2_{tot}	$\Delta\chi^2_{tot}$	σ
0.68	22.5	0	$< 1\sigma$
0.71	23.5	1	1σ
0.80	26.5	4	2σ
0.95	31.5	9	3σ
1.17	38.5	16	4σ
1.44	47.5	25	5σ

parameter were increased or decreased. At the end, more than 400 orbits in total were computed and fitted to the data.

6.2.2 A χ^2 criterium

A valid computed orbit has to fit both the measured velocities and positions. Therefore, two reduced $\tilde{\chi}^2$ values, one for the positions, $\tilde{\chi}^2_{pos}$, and another for the velocities, $\tilde{\chi}^2_{vel}$, were estimated. While fitting the orbits, the $\tilde{\chi}^2_{pos}$ values for the positions and velocities were considered independently because the $\tilde{\chi}^2$ values for the velocities were, in general, much smaller than for the positions. In some cases they indicated that measurement errors were systematically overestimated. This way, it was possible to attain, both in velocities and in positions, a similar fit quality. Under this condition, it is always possible to define a common χ^2_{tot} by adding both the χ^2 values obtained from the positions and the velocities. The total reduced $\tilde{\chi}^2$, $\tilde{\chi}^2_{tot}$, is simply the χ^2_{tot} divided by the number of degrees of freedom which is equal to 33 in our case. Table 6.1 lists obtained total reduced $\tilde{\chi}^2_{tot}$ and non-reduced χ^2_{tot} which indicated errors $\leq 5\sigma$. These errors were estimated by applying a deviation $\Delta\chi^2_{tot}$ from the the lowest obtained χ^2_{tot} . In the following analysis we used solutions with an error $\leq 1\sigma$.

6.2.3 Influence of model parameters

A particular important issue for this case are the values of the initial parameters. Solving first for a Keplerian orbit, and determining the set of parameters, allowed the constriction of the parameter margin. This procedure, with 6 initial input parameters is less intensive in computing. I used the position measurements for S2, the dynamical position of Sgr A* and the 5 line-of-sight velocity measurements as determined by Schödel et al. (2003) and Eisenhauer et al. (2003). The Keplerian fitting routine was verified with the latter mentioned Keplerian works, and showed complete approval.

Orbital Elements as Initial Parameters

The six independent elements correspond to the three velocities and three coordinates, that determine the orbit dynamically. From the imaging data, sky positions and proper motions are given in a certain error range for each epoch. For a chosen initial epoch, and given values for M_{tot} , f and P , six input values are varied within certain limits. This leads to a number of N^6 orbital runs for each fitting procedure (N = number of steps per parameter). At the end of each run a χ^2 value was estimated (see section 6.2.2), constructing this way a 6D-surface of χ^2 values. In a second step, in the cases with relatively low χ^2 , the fitting procedure was applied with a higher temporal resolution, i.e. smaller time step. Each of these cases was recomputed separately looking at higher resolution, but in a smaller parameter range, leading to a new 6D-surface of χ^2 . This iteration was repeated a few times till the necessary precision was reached, and the global minimum found.

Central Mass as Initial Parameter

The black hole potential at the position of S2 can be treated as a point mass. From limits of its proper motion Reid et al. (2003) deduced a lower limit of this mass at $5 \times 10^5 M_\odot$. It has also been shown that its mass is unlikely to exceed $4.8 \times 10^6 M_\odot$ (Ghez et al. 2003; Schödel et al. 2002). Another upper limit is set by the dynamical mass estimates at larger radii. We estimated an average value of the integrated total mass between ~ 0.2 pc and ~ 1 pc from gas tracers and stellar velocities following Schödel et al. (2002, see their figure 3) and Genzel et al. (2000, see their figure 17). At a 5σ level this estimate does not exceed a value of $4.8 \times 10^6 M_\odot$. In the simulations, the value of the central mass is varied in this mass range between $2.6 \times 10^6 M_\odot$ and $4.8 \times 10^6 M_\odot$, considering six values of M_\odot – estimates of the best fitting values from different observational works (Genzel et al. 2000, Schödel et al. 2003, Aschenbach et al. 2004, Ghez et al. 2005, and Eisenhauer et al. 2005). In addition, for any of these given total central mass values, M_{tot} , the effect of various extended mass fractions, f , was investigated (see Fig 7.4).

BH Position as Initial Parameter

Based primarily on the small differences between the radio and infrared positions, the estimated uncertainty of the Sgr A* infrared position is about 10 mas (Reid et al., 2003). Note that the well-studied star S2 moved within about 16 mas of the position of Sgr A* on the 2002 May 2. I used the position of Sgr A* as determined by Reid et al. (2003). When fitting non-Keplerian orbits, the location of the point mass is chosen within this error bar at 6 discrete positions - the central value of the nominal radio position, the four extreme values determined from the error bars, and the best offset value as determined by Eisenhauer et al (2003), which is the deviation of the focus of their Keplerian orbit from the central radio position. These six cases are denominated as the *centre*, *northern*, *western*, *southern*, *eastern* and *offset* positions. Then, to allow for a better sky coverage, 8 additional positions were chosen such that they encircle the *offset* position which was found to show the lowest $\tilde{\chi}^2_{tot}$ values. Fig 6.3 shows these different positions. Table 7.1 gives their coordinates relative to the *offset* position. In order to check the

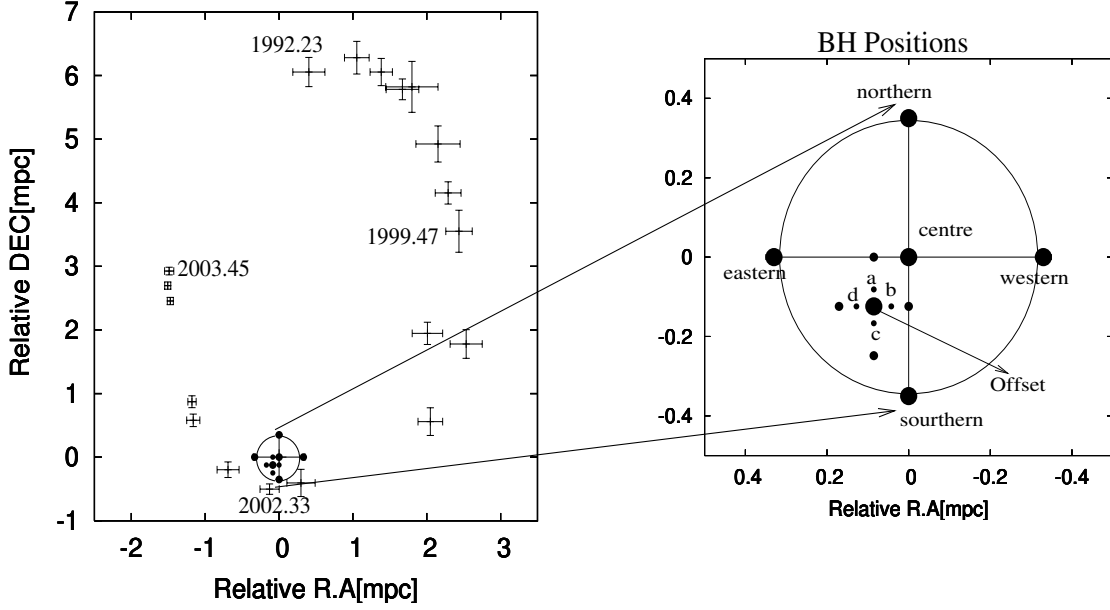


Figure 6.3: **Positions of the central mass.** *Left: Illustration of the sky positions at different epochs, Right: a zoom to the central position, the circle indicating the error range, the filled black circles indicate the different Black Hole positions chosen as initial parameter, the position at (0,0) indicates the nominal radio position of sgr A*.*

accuracy of the focus of the Keplerian orbit, we compare the two positions for the star S2 at the epoch 2002.30 calculated with the orbital parameters given by Eisenhauer et al. (2003) and by Ghez et al. (2003, astro-ph/0306130). From the corresponding positions and uncertainties, an offset of the projected orbital focus given by Ghez et al. (2003) from the one of Eisenhauer et al. (2003) of 0.0 ± 2.9 mas East and 0.8 ± 2.0 mas North can be derived. Hence, there is an excellent agreement between the two independent results.

Core radius

In order to take into account the uncertainty of the core radius of the inner cusp, the orbital fits computed for the best fitting model value of $R_1 = 15.5$ mpc, were repeated only in the case of the fitting orbits, with an error $\leq 2\sigma$, for the extreme cases of $R_1^{min} = 13.2$ mpc and $R_1^{max} = 20.2$ mpc.

Chapter 7

Stellar Orbits

In this chapter, I describe and develop the results obtained by Mouawad et al. (2005) on the modelling of the S2-orbit in terms of Keplerian and non-Keplerian orbits. Each case is justified under certain assumptions:

If for simplification, the mass to light ratio within $0.4''$ of Sgr A*, is considered to be comparable to that of the outer cluster ($M_{\odot}/L_{\odot}(2\mu\text{m}) \approx 2 M_{\odot}/L_{\odot}$), the stellar mass in this radius due to the stellar cusp will be $\sim 8500 M_{\odot}$ (see Table 4.1). Only in that case will the dynamics of the stars in the inner cusp be totally dominated by the super-massive black hole (Eckart & Genzel, 1997; Genzel et al., 2000; Ghez et al., 2000; Eckart et al., 2002; Schödel et al., 2002). In that case, the fraction of the extended mass over the point mass, being of the order of 10^{-3} , induces negligible peri-astron-shifts and the stellar orbits can be considered to be simply Keplerian. On the other hand, a more realistic approach which resembles the theoretical predictions on the increase of the mass-to-light ratio ($M_{\odot}/L_{\odot}(2\mu\text{m})$) towards the centre of a galaxy, should be considered. This is the case where the dynamics are no longer assumed to be Keplerian since the mass of the cusp would possibly hide more dark mass, yet, undetected with the present instruments. The obtained results show that it is not possible to distinguish between both Keplerian and non-Keplerian fits. More precisely, for both fits a minimum χ^2_{tot} value of 0.7 was obtained (see Fig 7.5). This leads to the possibility that apart from the black hole there could exist an additional extended mass component. When analysing stellar orbits around Sgr A*, the main interest is not only in the orbital elements of the individual stars, but mainly in the overall properties of the system. The study of the S2 orbit gives an upper estimate of the possible amount of mass present in a form of an extended component. It is of a high importance to explore this case. In fact the existence of an extended component, in a form of a cusp or a compact core in the very vicinity of a super massive black hole, is a key to know more about the history of formation of black holes, star clusters and other informations on the dynamics governed by a SMBH. These results were determined within the framework of this thesis and represents the first analysis of the orbit of S2 in the presence of a central mass distribution, extended to distances very close to the centre.

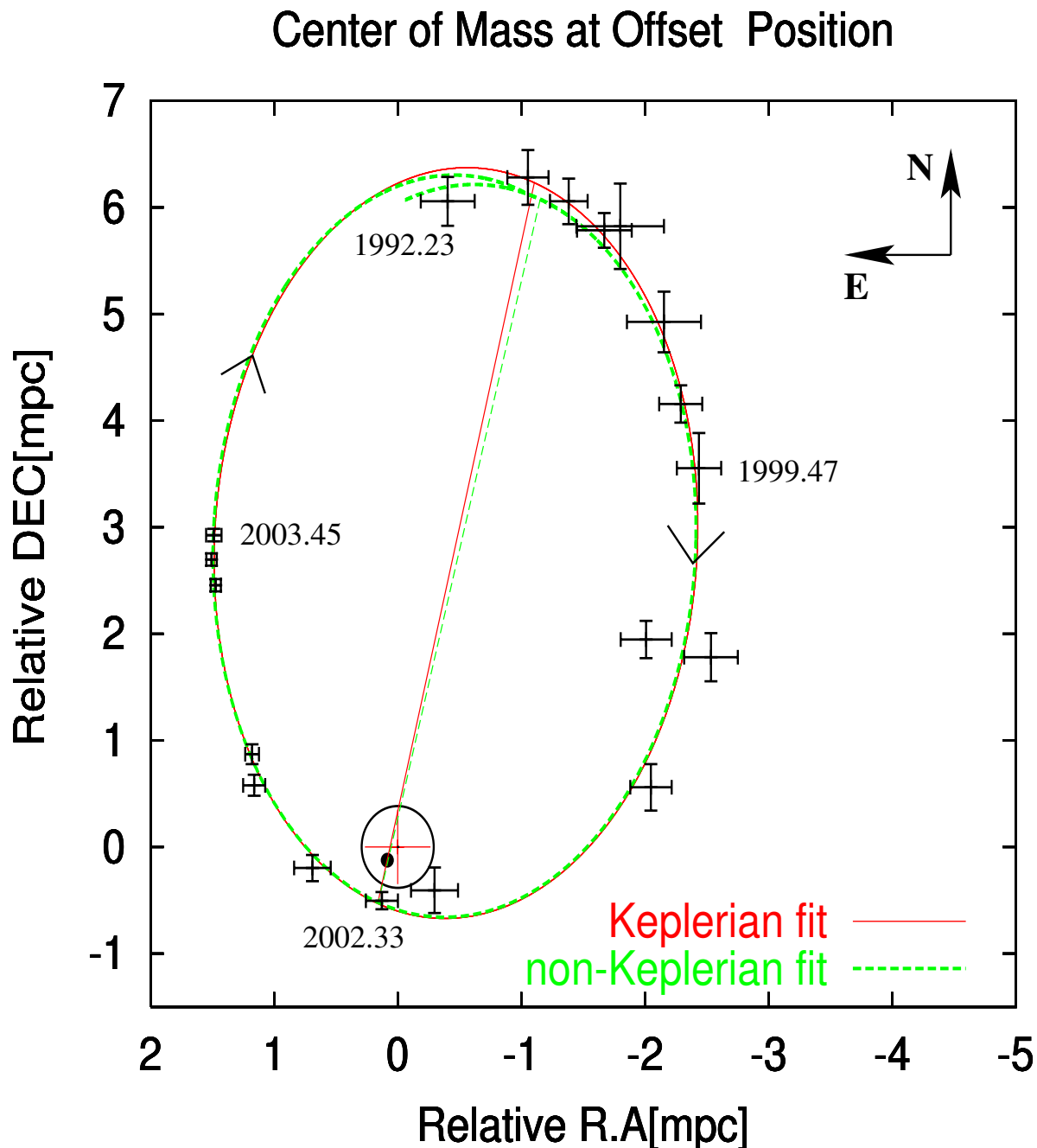


Figure 7.1: **Superposition of two best fitting orbits.** Red solid line: Keplerian orbit with $3.65 \times 10^6 M_{\odot}$ point mass. Green dashed line, non-Keplerian orbit with $4.8 \times 10^6 M_{\odot}$ total mass of which $1.2 \times 10^6 M_{\odot}$ are extended component. Here the central mass is at the offset position, 0.082 mpc east and 0.112 mpc south from the nominal radio position of Sgr A*. The lines connecting the peri-astron and apo-astron in both Keplerian and non-Keplerian cases are shown in red and green respectively.

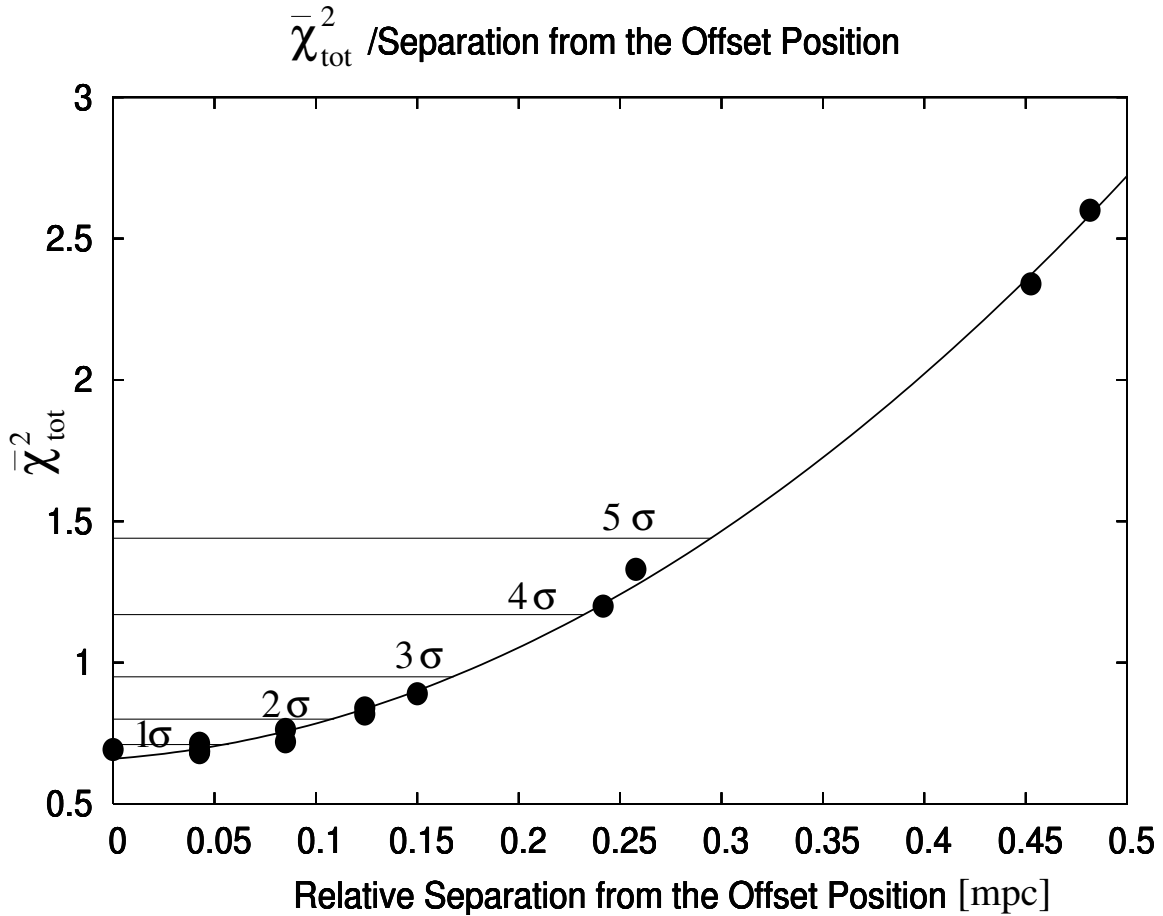


Figure 7.2: **Reduced $\bar{\chi}_{tot}^2$ values vs. separation from the *offset* position.** The lowest obtained reduced $\bar{\chi}_{tot}^2$ values in function of the separation from the *offset* position. These are fitted with a function of the form $7.2x^2 + 0.5x + 0.7$.

7.1 Results on Keplerian Orbits

In this work I present the orbit of S2 as it was determined from the measured positions of S2, the one used by Schödel et al. (2003) and Eisenhauer et al. (2003). Eisenhauer et al. (2003) included 5 spectroscopic measurements of the line-of-sight velocity of S2 in their analysis. In the case of Keplerian orbits, the best fit is obtained for a $3.65 \times 10^6 M_{\odot}$ black hole, with the black hole at the *offset* position, the orbital elements are given in Table A.1. The Keplerian fitting routine was verified with the latter mentioned Keplerian works, and showed complete approval.

Table 7.1: The lowest obtained $\tilde{\chi}^2_{tot}$ values. Table giving the lowest obtained $\tilde{\chi}^2_{tot}$ values for the 14 different cases of the central mass position. These positions are plotted in Fig 6.3. The coordinates given in brackets are in units of mpc. These are relative to the offset position.

BH position (R.A;Dec)	$M_{tot}[M_{\odot}]$	$M_{cusp}[\%]$	$\tilde{\chi}^2_{tot}$
Offset (0.0;0.0)	3.65	0%	0.69
Offset (0.0;0.0)	4.1	10%	0.69
Offset (0.0;0.0)	4.45	20%	0.69
Offset (0.0;0.0)	4.8	25%	0.7
a (0.0;0.045)	3.65	5%	0.68
a (0.0;0.045)	4.1	15%	0.68
b (-0.045;0.0)	3.65	0%	0.71
c (0.0;-0.045)	3.65	0%	0.71
c (0.0;-0.045)	4.1	10%	0.69
c (0.0;-0.045)	4.8	25%	0.7
d (0.045;0.0)	3.65	0%	0.7
d (0.045;0.0)	3.65	5%	0.7
d (0.045;0.0)	4.1	15%	0.71
(-0.09;0.0)	4.8	25%	0.76
(-0.09;0.0)	4.1	10%	0.77
(-0.09;0.0)	3.65	0%	0.78
(0.09;0.0)	3.65	5%	0.72
(0.09;0.0)	4.1	15%	0.72
(0.0;0.12)	4.1	20%	0.82
(0.0;0.12)	4.8	30%	0.82
(0.0;-0.12)	4.1	5%	0.84
(0.0;-0.12)	4.8	20%	0.84
Centre (-0.09;0.12)	3.65	5%	0.89
Southern (-0.09;0.23)	4.8	20%	1.2
Eastern (0.26;0.12)	3.3	0%	1.35
Eastern (0.26;0.12)	3.65	10%	1.35
Northern (-0.09;0.35)	3.0	10%	2.6
Western (-0.44;0.12)	4.0	20%	2.34

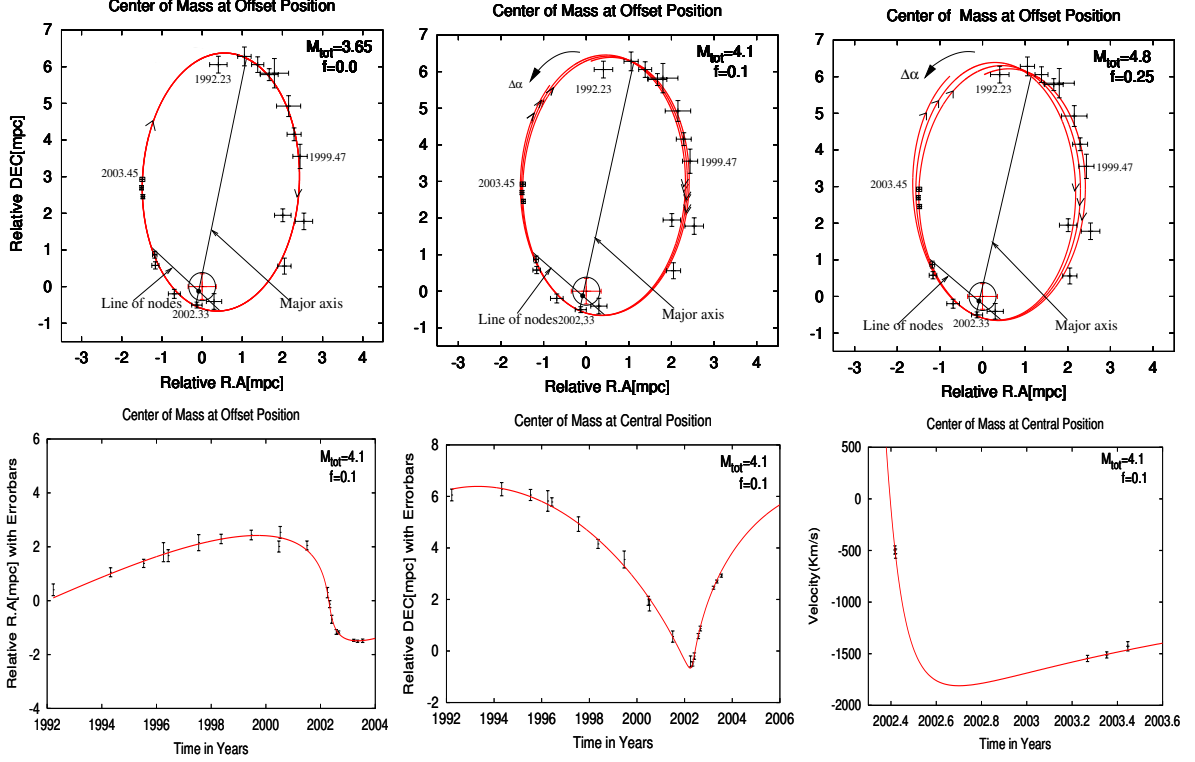


Figure 7.3: Three exemplary orbits determined by our fitting. Upper left panel: Keplerian orbit with $3.65 \times 10^6 M_\odot$ point mass. Upper middle panel, non-Keplerian orbits with $4.1 \times 10^6 M_\odot$ total mass of which $0.4 \times 10^6 M_\odot$ are extended. Upper right panel, non-Keplerian orbits with $4.8 \times 10^6 M_\odot$ total mass of which $1.2 \times 10^6 M_\odot$ are extended. Here the central mass is at the offset position, 0.082 mpc east and 0.112 mpc south from the nominal radio position of Sgr A*. The lower panels show the velocity in the relative R.A., the relative Dec., and along the line-of-sight as a function of time for the case of $4.1 \times 10^6 M_\odot$ central mass + 10% extended component. This case is representative for the other cases. The direction of $\Delta \alpha$ the peri-centre-shift is shown by an arrow.

7.2 Results on Non-Keplerian Orbits

Position of Sgr A*

As explained in chapter 6, the orbital fitting was performed choosing 14 different central mass positions. The orbits showing an error $\leq 1\sigma$ correspond to the cases where the central mass positions were at the *offset* position or at separations of $\pm 0.05 \text{ mpc}$ ($\pm 1.3 \text{ mas}$) in R.A or in Dec. from the *offset* position (see Fig.6.3). Fig.7.2 illustrates the behaviour of the χ^2_{tot} with separation from the *offset* position. For relative positions at $(\pm 0.09 \text{ mpc}, 0.0 \text{ mpc})$ or $(0.0 \text{ mpc}, \pm 0.12 \text{ mpc})$ the fitting orbits show errors $> 1\sigma$. The cases of the *eastern*, *northern*, *southern* and *western* position can most likely be excluded as mainly only fits with errors $> 5\sigma$ were found. To give nevertheless an idea of the orbits in such cases, Fig.7.6 illustrates some of them. Table 7.1

$M \backslash F$	0	0.05	0.1	0.15	0.2	0.25	0.3	0.35	0.4	0.45	0.5	0.55
6.8									1.41	0.79	0.85	1.81
6.1							2.08	1.04	0.75	0.82	1.8	
5.4						1.26	0.73	0.69	1.15			
4.8	3.97	3.2	1.9	1.18	0.86	0.7	0.94	1.46				
4.1	1.09	0.84	0.68	0.76	1.1	2.7						
3.65	0.68	0.79	1.07	1.39	2.55							
3.3	1.2	1.41	2.62									
3	2.02	3.24	4.23									
2.6	3.01	4.59										

Figure 7.4: **Values of χ^2 .** M is the total mass: point mass + cusp component, F is the fraction of the cusp component over the total mass. Dark red to very faint red corresponds to decreasingly well fitting orbits. Gray boxes for non fitting orbits. The best cases are obtained for $0.68 \leq \chi^2 \leq 0.7$.

lists the different cases showing the lowest $\tilde{\chi}_{tot}^2$ values for each central mass position. In the following, the focus of this study is on the case of the *offset* position of the central mass.

Central mass

If an additional extended mass component is assumed, then the best fit is obtained for a $4.1 \times 10^6 M_\odot$ total mass of which 10% or 15% are extended, or a $4.8 \times 10^6 M_\odot$ total mass of which 25% or 30% are extended. Fig 7.1 is a plot of both Keplerian orbit and the non-Keplerian orbit which corresponds to the maximum cusp mass at 1σ level, giving the biggest peri-astron shift. Fig 7.4 gives the $\tilde{\chi}_{tot}^2$ values for the different central masses values and extended mass fractions. The lowest values given in dark red indicate clearly a trend, which is the higher the total central masses are the higher the extended mass fractions, f , can get. These values represent the best fitting orbits. Similarly, a more representative plot for these values is shown in figure 7.5 where for each fraction f , each set of $\tilde{\chi}_{tot}^2$ values vs. different discrete central total mass values at the offset position was fitted with splines indicating clearly the valley of the minimum $\tilde{\chi}_{tot}^2$, and its corresponding total central mass value. This figure shows clearly that there could exist different combinations of possible extended mass fractions and total masses.

A plot of these orbits is given in Fig 7.3. A representative plot for three best fitting orbits is given in Fig 7.3, it shows as well the positions and the 5 radial velocity measurements in function of time. The orbital parameters including the error bars for the three above discussed best fitting cases are given in Table A.1. Within the uncertainties the orbital parameters for the Keplerian case agree with earlier works (Schödel et al. (2003), Ghez et al. (2003), Eisenhauer et al. (2003)). Giving the fact that a central mass of $4.8 \times 10^6 M_\odot$ shows 5σ level estimate of the dynamical mass estimates (see section 6.2.3), the orbit with $4.1 \times 10^6 M_\odot$ with 10% or 15% extended component is considered to be the best fitting orbit in the case of non-Keplerian orbits.

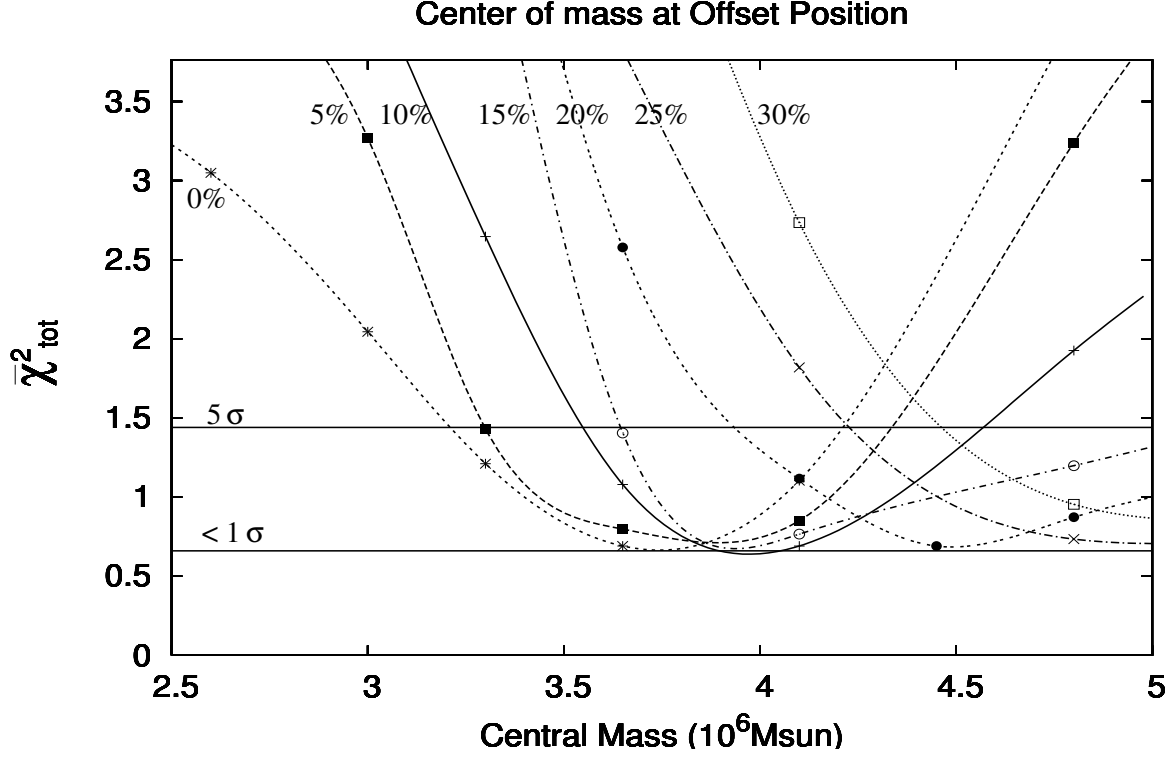


Figure 7.5: $\tilde{\chi}_{tot}^2$ values vs. the total central mass. Plot of the $\tilde{\chi}_{tot}^2$ values vs. the total central mass, M_{tot} , calculated for different extended mass fractions, f , with the point mass at the offset position. Values of the same f are fitted with splines. Crosses: $f = 0$; “x” symbols: $f = 0.05$; stars: $f = 0.1$; empty squares: $f = 0.15$; filled squares: 0.2 , empty circles: $f = 0.25$; and filled circles: $f = 0.3$. The two horizontal lines denoted by $< 1 \sigma$ and 5σ delimit the region fitting orbits ($\tilde{\chi}_{tot}^2 \leq 1.45$). The fit with the lowest $\tilde{\chi}_{tot}^2$ is indicated by a star, it corresponds to the case of $M_{tot} = 4.1 \times 10^6 M_{\odot}$ and $f = 0.1$.

Higher total central masses and cusp masses

Fig 7.5 shows a plot of $\tilde{\chi}_{tot}^2$ vs. different discrete central total mass values and for each fraction f of the extended mass at the offset position. Other orbits with total masses higher than $4.8 \times 10^6 M_{\odot}$, up to $11.6 \times 10^6 M_{\odot}$ were also modelled. It is found that at a 5σ level of confidence the S2 orbit could fit the data for cusp masses of up to 70% of the total mass. This resulted in an upper limit of cusp masses as high as $8 \times 10^6 M_{\odot}$ corresponding to an extended component of $\sim 1 \times 10^6 M_{\odot}$ inside the sphere of a radius equal to the apo-centre of S2. However, the total masses in these cases are in disagreement with the dynamical mass estimates at large radii. Therefore, these are regarded as unrealistic but I mention the result for completeness.

Large amounts of extended mass inside the S2 orbit would be possible if the mass distribution function at the centre were steeper than in our model or if the core radius were smaller than the apo-centre of S2 (~ 9 mpc). In that case I found that mass densities – exceeding the currently derived few $10^8 M_{\odot} \text{pc}^{-3}$ by three or four orders of magnitude – are unlikely to form a stable configuration because stellar collisions will become of increasing importance (see

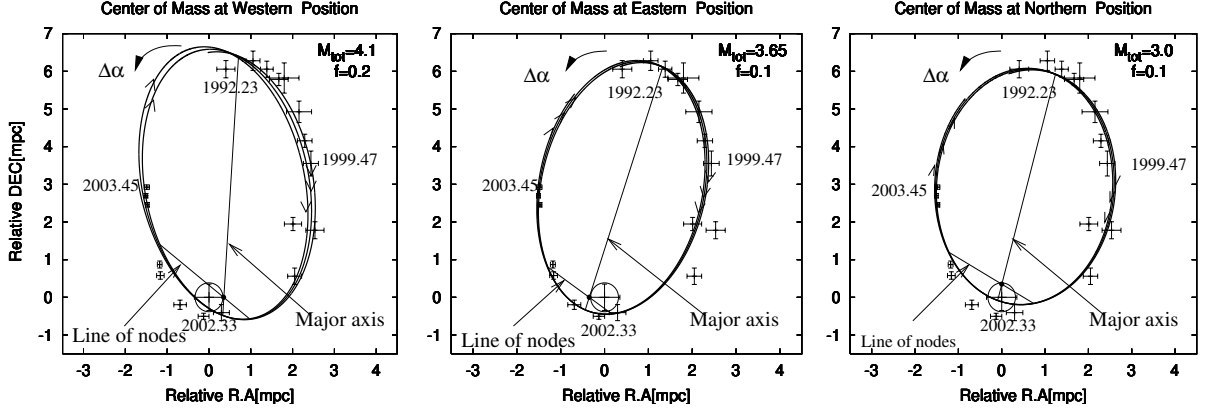


Figure 7.6: **Exemplary three non-fitting orbits.** Example of 3 orbits with an error $\geq 5\sigma$ corresponding to: (Left) the case of Western position, a fit with $3.3 \times 10^6 M_\odot$ point mass + $0.8 \times 10^6 M_\odot$ extended component (Middle) the case of Eastern position, a fit with $3.3 \times 10^6 M_\odot$ point mass + $0.4 \times 10^6 M_\odot$ extended component, and (Right) the case of Northern position, a fit with $2.7 \times 10^6 M_\odot$ point mass + $0.3 \times 10^6 M_\odot$ extended component.

section 8.2.1).

7.3 Influence of Mass Distribution and Cusp Size

The study is based on the assumption that the mass distribution of the 'inner cusp' follows that of the stellar light. Hence, the shape of the cusp was fixed to a Plummer model-like distribution with a fixed slope $\alpha = 5$, similarly its core radius was probed within a certain range, which were defined in Table 4.1. In this section, this assumption is relaxed, and I give a description of the eventual case, when both shape and size of the cusp transcend these limits.

7.3.1 Power-Law mass distribution

Using a series of Plummer model density profiles, implies a value of the cusp slope of $\alpha \leq 5$. As mentioned in chapter 4, Genzel et al. (2003) fitted the stellar number density with a broken power-law of a slope equal 1.4 ± 0.1 . From theoretical models of cusps around massive black holes, one would expect power-law indices in the range $3/2 \leq 7/4$ (Bahcall & Wolf 1977; Murphy et al. 1991). To study the influence of the density profile on the peri-astron shift, I performed fittings of the S2 orbit considering a power-law profile of a slope equal to 1.4. It is of the form,

$$\rho(R) = 1.2 \times 10^6 \left(\frac{R}{10''} \right)^{-\alpha} (M_\odot pc^{-3})$$

, with $\alpha = 2.0 \pm 0.1$ at $R \geq 10''$ and $\alpha = 1.4 \pm 0.1$ at $R < 10''$. The peri-astron shift induced by the same amount of mass inside S2's apo-centre but different fractions of mass, f , did not exceed the one induced by a Plummer model density profile by more than 12% (see Fig 7.7). Thus, by

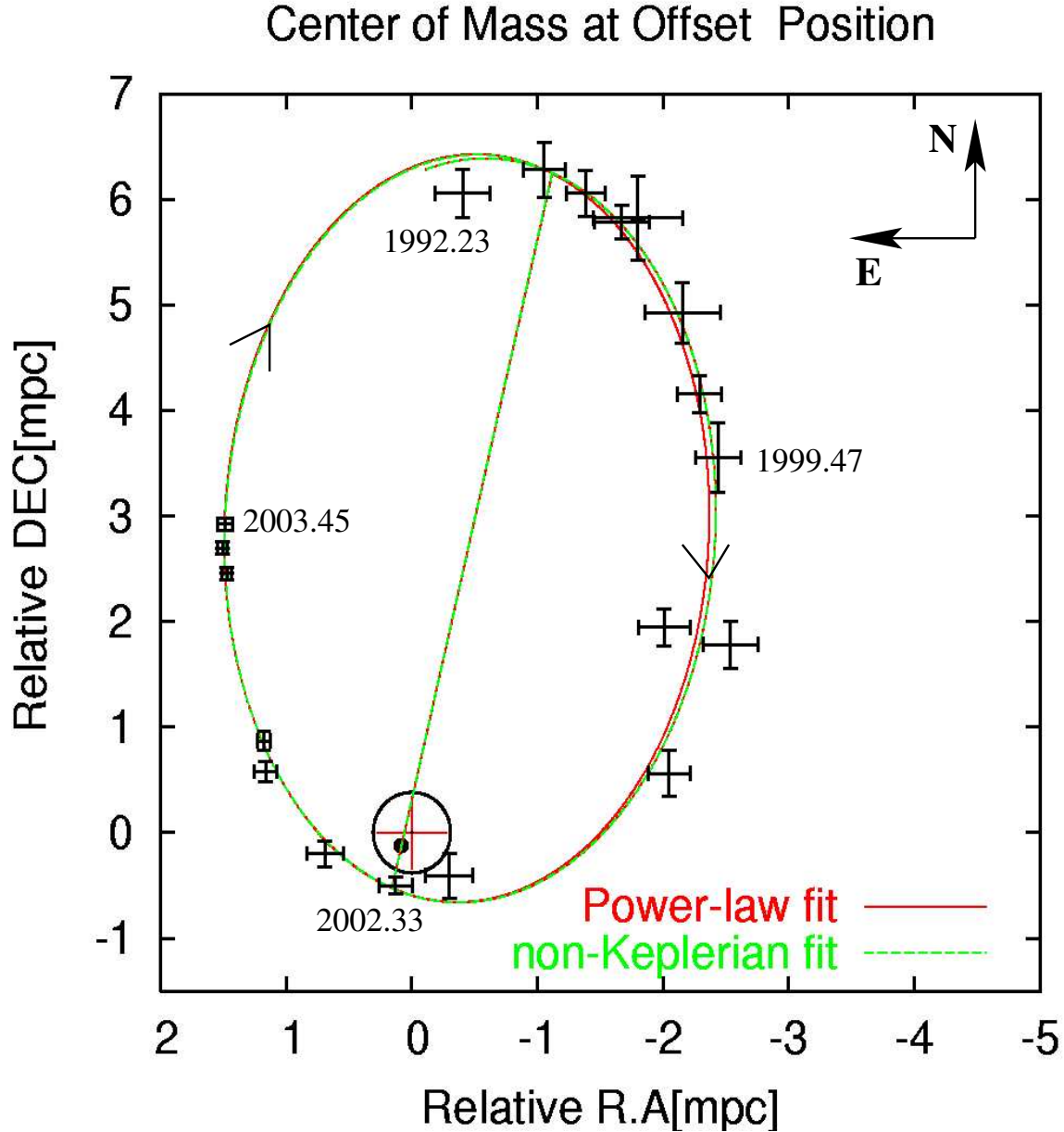


Figure 7.7: **Orbits in Power-law and Plummer potentials.** Red solid line: Keplerian orbit in a Power-law 'inner cusp' potential with $3.7 \times 10^6 M_{\odot}$ point mass plus $0.5 \times 10^5 M_{\odot}$ inside the sphere of radius the apo-centre of the S2-orbit. Green dashed line: non-Keplerian orbit with $4.1 \times 10^6 M_{\odot}$ central mass and $f = 0.1$; this correspond to $\sim 0.5 \times 10^5 M_{\odot}$ inside the sphere of radius the apo-centre of the S2-orbit. The induced peri-astron-shifts are $48'$ and $42'$ for a power-law and a Plummer model respectively. Here the central mass is at the offset position, 0.082 mpc east and 0.112 mpc south from the nominal radio position of Sgr A*. The line of nodes are shown in red and green respectively.

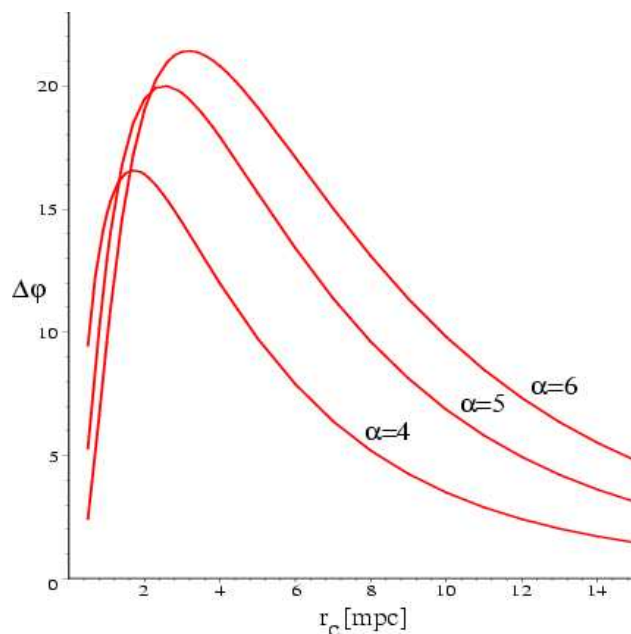


Figure 7.8: **Orbital shifts as a function of $R_1 = r_c$ = core radius of the Plummer model.** *Orbital shifts in degrees as a function of R_1 , for $\alpha = 4, 5, 6$, and for a star with orbital elements similar to that of the S2 and with a very high extended mass fraction of 0.8 (Rubilar & Eckart, 2001).*

covering a wide range of slopes $1.4 \leq \alpha \leq 5$, it results that the deviation of the peri-astron-shift never exceeds 12% from the derived value for a Plummer mass distribution, meaning that for a Plummer model a higher amount of mass can be included inside the orbit and the peri-astron shift induced will be smaller than for the case of a power-law. Thus, these estimates indicate an upper limit on the mass that could be present inside the S2 apo-centre, and consequently on the mass of the cusp. Here, I point out that the exponent α of a Plummer model does not represent a constant slope of the mass distribution, the slope of the cusp is a function of the core radius as well as the separation from the centre. In the plot of the number density counts vs. separation from the centre (see Fig 4.1), it is clear that the slope of the cusp is shallow inside the core radius, but has a maximum of 5 around the core radius. Thus, since the star S2 orbits inside the core radius, it is mainly influenced by a rather shallow mass distribution. This is consistent with the results of Rubilar & Eckart (2001). They found that the maximum orbital shift is reached faster by the sharper edged mass distributions, i.e. for steeper mass distributions (see Fig 7.8).

7.3.2 Core Radius of the 'inner cusp'

In the case of the *offset* position, for all the orbits with errors $\leq 2 \sigma$, the fitting procedure was repeated for the extreme cases of $R_1^{min}=13.2$ mpc and $R_1^{max}=20.2$ mpc of the inner cusp radius. Even with these different core radii, it results that the cases of the *offset* position listed in Table 7.1 still give the lowest $\tilde{\chi}^2_{tot}$ values. Also the fit quality remains unchanged at $\tilde{\chi}^2_{tot} \simeq 0.7$. This is due to the fact that the mass of the cusp induced inside the orbit of S2 is relatively small because the cusp radius is bigger than the apo-centre of S2.

I also consider that the compact component can have a much smaller core radius than the stellar profile, possibly well within the S2 apo-centre. In this case, based on the result of Rubilar & Eckart (2001, see Fig 7.7), one can deduce that for the same extended mass fraction, f , the induced peri-astron shift is smaller for a bigger core radius.

The plot of the Fig 7.8 shows the orbital shifts $\Delta\phi$ as a function of R_1 , for $\alpha = 4,5,6$, and a fraction f of 0.8 for a star with an apo-centre distance of 10 mpc. This plot demonstrates that there is a maximum orbital shift depending on the properties of the mass distribution. Decreasing R_1 from infinity to smaller values, the amount of mass that is resolved by the stellar orbit between the apo-astron and peri-astron increases which results in an increasing orbital shift. Then the amount of resolvable mass decreases again as the extent of the mass distribution shrinks below the peri-astron radius. Thus for a core radius that does not exceed a value of 15.5 mpc, the estimation on cusp mass as presented in this work is an upper limit.

Another characteristic deduced from the plot is that, the maximum orbital shift is reached faster by the sharper edged mass distributions (i.e. for larger values of α). This behavior represents a degeneracy in the sense that independent of α there are in general two different radii R_1 at which a given observable peri-astron shift occurs. Therefore, (for a given fraction of unresolved mass f) a minimum of two stars on different orbits is required to derive the compactness (shape of the distribution described by α) of the central mass concentration. Three stars on different orbits (i.e. with different orbital energy E or angular momentum l) are necessary in order to unambiguously solve for all three parameters f , α , and R_1 .

7.4 Relativistic Prograde Peri-astron-shift

The scale of distances at which the relativistic effects are appreciable is determined by the gravitational length scale. For a mass $M = 3.7 \times 10^6 M_\odot$ of the SMBH, it is given by

$$\frac{GM}{c^2} = 3.7 \times 10^{-4} \text{ mpc} \sim 3.6 \times 10^{-2} \text{ AU} \quad (7.1)$$

This equals half the Schwarzschild radius and corresponds to ~ 1500 the peri-centre distance of the star S2. Therefore relativistic effects are expected to influence the S2-orbit.

The presence of the compact mass concentration in the SMBH will induce prograde peri-astron-shifts which will result in rosetta-shaped orbits. The resulting relativistic prograde peri-astron advance per revolution can be written as (see Weinberg 1972, eq.(8.6.11)).

$$\Delta\phi = \frac{6\pi G}{c^2} \frac{M}{a(1-e^2)}, \quad (7.2)$$

with a being the semi-major axis and e the eccentricity of the orbit, respectively. For the case of the S2-orbit, $e = 0.88$ and $a = 4.5$ mpc. The resulting angular shift for a central black hole mass of $\sim 3.7 M_{\odot}$ is about $9'$, which is a less dominant but considerable effect in comparison to the highest Newtonian retrograde shift $> 1^{\circ}$ allowed by the S2-orbit. In this study relativistic effects are not included. It should be pointed out that the peri-centre-shift due to relativistic effects is in the opposite direction of that due to the extended mass and that in a way, they could mask the amount of extended mass close to the SMBH.

7.5 Conclusion and Outlook

In this chapter, it was demonstrated that the measured positions and line-of-sight velocities of S2 can be fitted by Keplerian orbits as well as by non-Keplerian orbits. Assuming a simple Keplerian case, by definition, the central gravitational potential is entirely dominated by the point mass associated with Sgr A*. More revealing, however, is the assumption of non-Keplerian orbits, where dynamical constraints can be derived on the extended mass component due to e.g. the surrounding stellar cluster. This is as well a more physical assumption, as the presence of an observed stellar cusp shows that – at least to a certain extent – there is some extended mass present near the black hole. In this work, this potential was modelled as the central black hole plus an extended mass component. This extended mass component is distributed according to the Plummer density model of the inner cusp that was obtained by fits to stellar number density counts in chapter 4. Based on the assumption that the extended mass follows the observed stellar distribution and using constraints given from dynamical mass estimates at outer radii, it is possible to derive an upper limit for the extended mass fraction.

With this analysis it was possible to pinpoint the Galaxy's central dark with an error of only 1.3 mas (10 AU), in agreement with (Schödel et al. 2003, Ghez et al. 2003, astro-ph/0306130, Eisenhauer et al. 2005). The results on the fitting of non-Keplerian orbits were analysed in terms of total central mass and fractions of cusp over the total central mass.

Independently on the extension of the cusp distribution towards the outer radii, it is possible to describe the results on non-Keplerian orbital fits of the star S2 in terms of the mass present inside the sphere of radius the apo-centre of the S2-orbit exclusively. This goes without the assumption of a certain cusp extension and therefore no constraints can be added from dynamical mass estimates at outer radii.

Therefore, the other way of presenting the results is in terms of total mass and fraction of M_{apo} , which is the mass present inside the sphere of radius the apo-centre of the S2 orbit. Table 7.2 describes the results on the orbital fitting in terms of M_{apo} , the central mass M_{inner} being the mass of the SMBH plus the extended fraction M_{apo} , and the cusp mass fraction, $M_{cusp} \%$, being M_{apo}/M_{inner} .

The remarkable comment to notice from this table, is that at a 1σ level, the possible range of total central mass is relatively narrow. Basically independent of the amount of total or extended mass, the values found for the total central mass is about $3.7 \pm 0.2 \times 10^6 M_{\odot}$. It is in agreement with the different results on Keplerian fits for the S2-orbit of $3.7 \pm 1.5 \times 10^6 M_{\odot}$ (Schödel et al. 2003) or $4.1 \pm 0.6 \times 10^6 M_{\odot}$ Ghez et al. (2003). It also agrees with results on multi-orbital

Table 7.2: **Cusp Mass for different $\tilde{\chi}^2_{tot}$ values.** Table giving, for each goodness of fit $\tilde{\chi}^2_{tot}$, the different total central masses ranges and the corresponding extended mass fractions inside the orbit of S2. This table is representative of the obtained results on the fitting of the S2 orbit.

$\tilde{\chi}^2_{tot} \leq$	$M_{inner}[M_{\odot}]$	$M_{apo}[M_{\odot}]$	$M_{cusp}[\%]$
1σ	[3.5 : 3.9]	[0.0 : 0.19]	5%
3σ	[2.8 : 4.4]	[0.0 : 0.763]	15%
4σ	[2.6 : 4.5]	[0.0 : 0.995]	22%

fits of seven S-stars giving $M_{BH} = 3.7 \times 10^6 M_{\odot}$ (Ghez et al. 2005) or of six S-stars giving $3.61 \pm 0.32 \times 10^6 M_{\odot}$ for a distance to the GC of 7.62 kpc (Eisenhauer et al. 2005).

At a 3σ level, this is also in agreement with the latest black hole mass estimate of $2.72^{+0.12}_{-0.19} \times 10^6 M_{\odot}$ that were derived by Aschenbach et al. (2004) from an analysis of the quasi-periodicity observed in strong X-ray flares.

In chapter 8, the analysis of the 'inner cusp' will be done in terms of the mass that is confined inside the core radius of the Plummer model.

Chapter 8

Analysis

The central question investigated in this chapter is the nature of the possible extended mass component in the cusp at the GC. Two hypotheses will be discussed: The existence of a cluster of faint low-mass stars, not yet detectable with the resolution and sensitivity of current instruments, and the existence of a cluster of heavy dark objects like stellar black holes (SBH) and neutron stars (NS).

The mass of the 'inner cusp' derived from direct stellar number density counts in chapter 4 corresponds only to $8540 M_{\odot}$ which is equivalent to $3100 M_{\odot}$ inside the core radius R_1 (15.5 mpc or $0.4''$). It is based on the assumption that the ratio of the stellar number counts to the total stellar mass does not vary with radius and environment in the Galactic Centre (see also Genzel et al., 2003), and that the $M/L(2\mu\text{m})$ is equal to $2 M_{\odot}/L_{\odot}$ at all separations from the centre. This implying a homogeneous stellar population at all distances from the centre. As it was outlined in the previous chapters, in this work, the mass-to-light ratio, $M/L(2\mu\text{m})$, is considered to increase in the 'inner cusp', which will allow for a population change in the centre. In section 8.1, the K-band luminosity function is analyzed, the presence of faint low-mass stars is studied, and M/L ratios are derived. In section 8.2, I investigate the existence of a cluster of stellar remnants and a cluster of intermediate mass black holes. Finally, section 8.3 and 8.4 concern the connection and implications of a dark extended mass distribution with the observations.

8.1 The K-Luminosity Function

I use the K -band luminosity function (KLF) for $K \leq 18$ mag within a projected radius of $1.5''$ from Sgr A* as it was determined by Genzel et al. (2003, see Fig 8.1) (Note that the KLF is not corrected for extinction nor for distance modulus). The KLF gives the local number density for a given K magnitude. As it can be seen in Fig 8.1, in the central $1.5''$, the surface density increases for the fainter stars. With a magnitude limit of $K = 18$, this proposes that undetected fainter stars can be even denser, and probably hide a considerable mass in the central $1.5''$. In the following, the maximum amount of mass present in stars is derived.

The authors fitted the KLF with a power-law with a slope of $\beta = 0.21 \pm 0.03$, ($\beta = d \log N / dK$). Since this result is based on a number of roughly 60 stars within $1.5''$ of Sgr A*, the observed stars themselves cannot account for a significant extended mass component. However, here it is

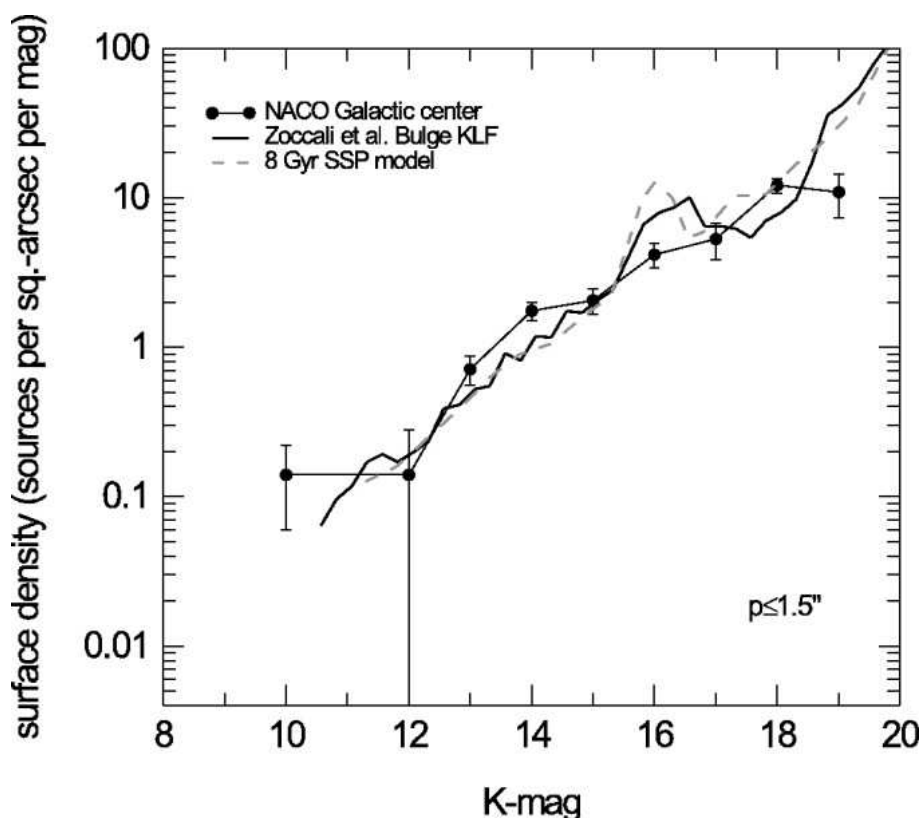


Figure 8.1: **K-band Luminosity Function of the central cusp region (Genzel et al. 2003).** *KLF* (sources per square arcsecond per magnitude) as a function of K_s of the central cusp region ($\leq 1.5''$; filled circles with $\pm 1 \sigma$ error bars). The *KLF* points have been corrected for incompleteness as discussed in the text. Errors take into account both the Poisson error and the uncertainty of the crowding/confusion correction (10%). The Galactic centre data points are a combination of the new 2002 August NAOS/CONICA data (for $12 \leq K_s \leq 18$) and of the SHARP/NTT data sets (T. Ott et al. 2003, in preparation), scaled in the $12 \leq K_s \leq 14.5$ overlap region for best match with the CONICA data. For comparison, the continuous curve is the *KLF* of the Galactic bulge on scales of degrees, and the dashed curve is a single-age (8 Gyr) stellar population model of the bulge (from Zoccali et al. 2003), both scaled vertically to match the centre data and corrected horizontally to the same K -band extinction.

Table 8.1: **Characteristic of a hypothetical inner cluster of main sequence stars.** For each 'observed' K -magnitude limit (not corrected for extinction) I give the numbers of stars N , cluster mass M_{Cl} , average stellar masses M_{av} , and mass-to-luminosity ratio, $M/L(2\mu m)$, within the central $0.4''$ for hypothetical Plummer model type clusters with KLF extrapolated by two power-law slopes of $\beta = 0.21$ and $\beta = 0.35$. M_{Cl} is the mass inside the core radius R_1 of the innermost Plummer model component. The derived M/L values include a correction for $A_K=3$.

Magnitude limit	$\beta=0.21$				$\beta=0.35$			
	N	$M_{Cl}[M_{\odot}]$	M_{av}	M/L	N	$M_{Cl}[M_{\odot}]$	M_{av}	M/L
$K \leq 28$	3500	800	0.9	1.0	44500	5200	0.1	3.7
$K \leq 27$	2200	710	1.4	0.9	20000	3700	0.15	2.8
$K \leq 26$	1350	620	2.3	0.8	9000	2400	0.3	1.8
$K \leq 25$	820	525	3.7	0.7	4100	1500	0.8	1.1
$K \leq 24$	510	450	6.0	0.6	1920	1000	1.6	0.8
$K \leq 23$	310	390	10	0.5	950	700	3.3	0.5
$K \leq 22$	190	325	16	0.4	510	480	6.0	0.4
$K \leq 21$	120	235	26	0.4	320	380	9.7	0.3
$K \leq 20$	70	193	42	0.3	230	270	11.2	0.2

assumed that the observed stars trace the mass carrying population which can currently only be accessed theoretically by extrapolating the KLF towards its faint end.

For the extrapolation of the KLF two different slopes were considered, $\beta = 0.21$ and a steeper one, $\beta = 0.35$, which fits the Bulge KLF (Alexander and Sternberg 1999) as well as a model of an old (~ 10 Gyr) stellar cluster of solar metallicity (Zoccali et al. 2003). In the following, only the region within R_1 of the inner Plummer model component is considered.

The KLF gives the number of stars per surface area per magnitude. As a first step, in order to calculate the total number of stars present within the spherical volume enclosed by the core radius of $R = 0.4''$ of the here used central Plummer model component, the KLF is de-projected (see Appendix A.2). This will give a volume number density for a given K magnitude. Having the intrinsic number of stars, for a given magnitude, from stellar counts using imaging data, the total number of stars, $N(\leq K)$, brighter than a magnitude K , can be, in a second step, computed. In a third step, one needs to estimate the mass of the $N(\leq K)$ stars. Therefore, masses of different spectral types and luminosity classes were also derived for the corresponding K -band magnitudes, this is explained in Appendix A.3 Adequately, $M/L(2\mu m)$ are estimated in a final step (see also Appendix A.2). Table 8.1 lists the resulting numbers of stars, the total cluster mass, M_{Cl} , the average stellar mass in the cluster, M_{av} , and the corresponding $M/L(2\mu m)$ for clusters given by faint-end KLF with slopes of $\beta = 0.21$ and $\beta = 0.35$ and for different cut-off magnitudes, between $K = 20$ ($M_{min} = 1 M_{\odot}$) and $K = 28$ ($M_{min} = 0.06 M_{\odot}$).

The results listed in Table 8.1 show that the mass of stars present within $R = 0.4''$ deduced from a $\beta = 0.21$ slope KLF cannot be higher than $800 M_{\odot}$, even after extrapolation to the faintest

Table 8.2: **Estimated masses of different stellar types.** *Masses, Mass (M_{\odot}), estimated for a given magnitude K , and for different spectral types in luminosity class V (see Appendix A.3).*

K[mag]	Mass[M_{\odot}]	Spectral types
16.425	1.60	F0
17.005	1.40	F5
17.695	1.05	G0
18.665	0.79	K0
18.915	0.67	K5
20.065	0.51	M0
20.065	0.4	M2
20.915	0.33	M3
22.315	0.21	M5
23.815	0.12	M7
25.265	0.06	M8

magnitudes (see Table 8.2 for a short list of K-magnitudes and corresponding main sequence stars at the GC, Table A.3 includes a more complete list for a larger sample of stars). Therefore, a cluster with a KLF of $\beta = 0.21$ cannot explain a mass of $3100 M_{\odot}$ within $R = 0.4''$, estimated from direct number density counts with an $M/L(2\mu m) = 2 M_{\odot}/L_{\odot}$.

$M/L(2\mu m)$ converges to a value $2 M_{\odot}/L_{\odot}$ and M_{cl} converges to $\sim 3100 M_{\odot}$, for $\beta = 0.35$, and a magnitude limit between 26 and 27. Higher magnitude limits would increase $M/L(2\mu m)$ further, and the mass of the inner cusp calculated from the Plummer model would be underestimated.

Table 8.1 also shows that for a main-sequence stellar population, $M/L(2\mu m)$ does not exceed $4.0 M_{\odot}/L_{\odot}$, even if very faint low-mass stars ($K = 28$) and a steep faint-end KLF ($\beta = 0.35$) are considered. On the other hand, the derived M/L values for the best fitting orbits from the modelling of the S2-orbit are given in Table 8.3. They result in high values of $96 M_{\odot}/L_{\odot}$ and $144 M_{\odot}/L_{\odot}$ possible within the obtained best fitting cases of 10% and 15% cusp and a total mass of $4.1 \times 10^6 M_{\odot}$. The contribution of the mass distribution of the 'composite model' for the different values of M/L is presented on the enclosed mass plot in Fig 8.2. The contribution in mass inside R_1 can be read on that Figure for each curve of different M/L . These high M/L values derived from the S2 modelling exceed by far the highest possible M/L of $4 M_{\odot}/L_{\odot}$ derived from extrapolation of the faint-end KLF. The latter leading to the conclusion, that the best fitting case of a non-Keplerian orbit for S2 allows for an extended mass component that is far too large to be explained by a stellar population of main sequence stars, and therefore would require another type of mass carriers. I show in section 8.2 that such a configuration is possible.

Table 8.3: **Mass-to-Light ratios for different cusp mass values.** *Mass-to-light ratios $M/L(2\mu\text{m})$, for the different offset position fitting orbits discussed in chapter 7. The errors on M/L are model dependent. From scaling to the enclosed mass estimate in Fig. 4.2, the error is estimated to be of 10%.*

M_{tot}	f	$M/L(2\mu\text{m})[M_{\odot}/L_{\odot}]$
3.65	0.0	2.00
3.65	0.05	42.74
3.65	0.10	85.48
4.10	0.05	48.01
4.10	0.10	96.02
4.10	0.15	144.03
4.10	0.20	192.04
4.80	0.20	224.82
4.80	0.25	269.32
4.80	0.30	337.24

8.1.1 Stability of a cluster of low-mass Stars

For a multi-mass stellar distribution, high mass stellar remnants (SBHs and/or NHs) are expected to migrate to the centre as a consequence of dynamical friction. One would expect that, within a Hubble time, these compact objects show a higher concentration toward the centre than the lighter ones (Morris et al., 1993; Escudé & Gould, 2000), which should be transferred by that mechanisms to orbits at greater distances from the centre of the cluster. This argues against the existence of a cluster of low-mass stars in the inner cusp.

On the other hand, the possibility of a cluster of low-mass stars cannot be excluded and we are far from understanding the properties of the stars in the cusp. There is for example the unexplained presence of massive young stars, e.g. MS O/B-type stars close to the black hole (Genzel et al., 1997; Eckart, Ott & Genzel, 1999; Figer et al., 2000; Gezari et al., 2002; Ghez et al., 2003, Eisenhauer et al. 2005, submitted). These stars have not had enough time to achieve energy equipartition with the fainter older stellar population. They are hence dynamically un-relaxed. Also, there are indications for a radial anisotropy of the stars in the cusp which might be un-relaxed (see section 3.2.3), in spite of the expected short relaxation time in this dense environment. Because of this general lack of theoretical understanding of the cluster near Sgr A*, one can consider that a cluster of faint low-mass stars should not be ruled out entirely from the possible interpretations of the 'inner cusp' (see Mouawad et al. 2005).

8.2 Is the Cusp Dominated by Dark and Massive Objects?

A result of the model calculations is that a possible best solution for the orbital fits of star S2 can be achieved with a black hole mass of $M_{BH} = 3.65 \times 10^6 M_{\odot}$ and a fraction, f , of 15% or less

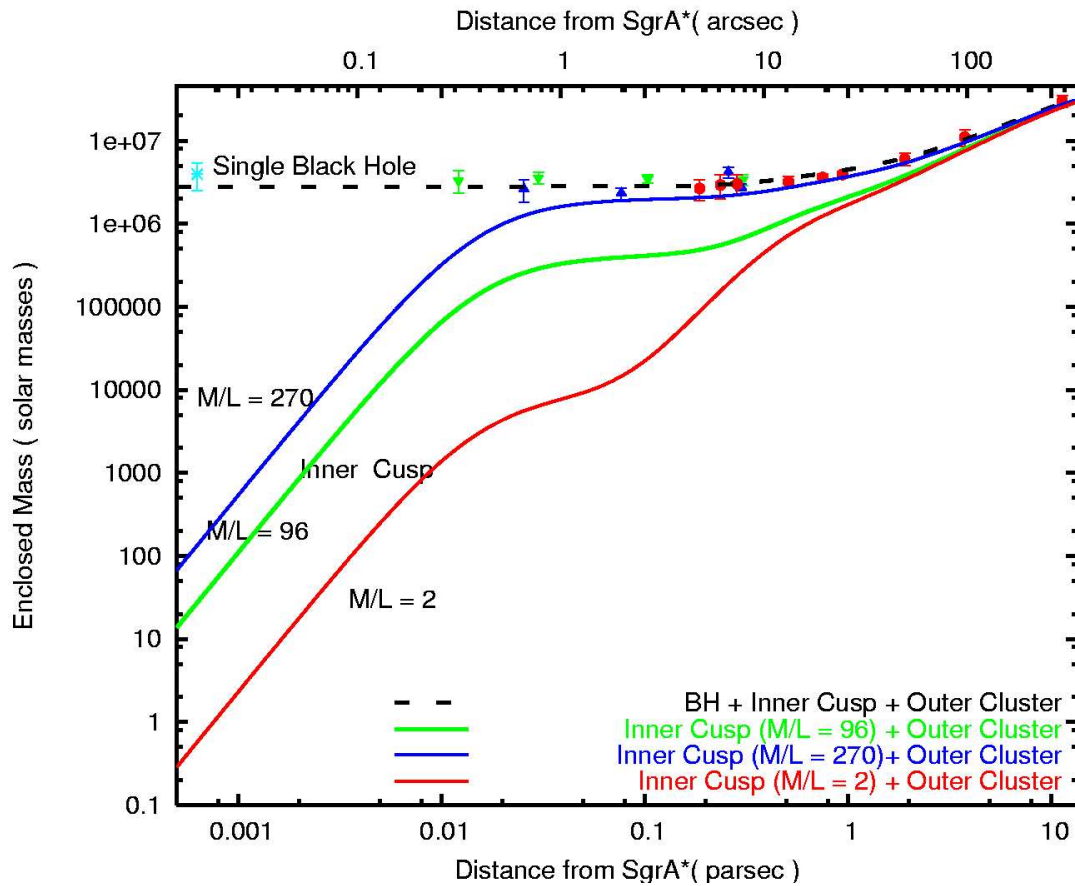


Figure 8.2: **Influence of the M/L on the mass distribution.** Enclosed mass in the central 10 pc similar to Fig 4.2. The contribution of the mass distribution of the 'composite model' is plotted for different values of the M/L . Red: $M/L = 2$ corresponds to the Keplerian case. Green: case of cusp fraction $f = 10\%$ for a central mass of $4.1 \times 10^6 M_{\odot}$. Blue: case of cusp fraction $f = 25\%$ for a central mass of $4.8 \times 10^6 M_{\odot}$.

i.e. $M_{cusp} \leq 1.5 \times 10^5 M_{\odot}$. The evaluation presented in section 8.1 shows that such a heavy cusp is unlikely to consist of stars only. Here, I study the case whether such a cusp could consist of heavier mass carriers like SBHs or NSs.

Presence of stellar remnants in the centre due to dynamical friction

When the compact remnants of massive stars are themselves significantly more massive than the normal field stars in the Galactic Centre, as would be the case of black hole remnants, than they are susceptible to inward migration as a consequence of dynamical friction. The resulting mass segregation can lead to a pronounced concentration of compact objects within the central stellar core within a Hubble time (Morris, 1993). N -Body simulations of globular clusters showed

that the combination of stellar evolution (production of SBHs, NSs, white dwarfs (WDs) and of binaries including such objects) and stellar dynamics will almost certainly lead to a strong increase of M/L in the central parts of the nuclear star cluster. SBHs and NSs sink to the centre and may coalesce (Gürkan et al. 2003). Such highly detailed self-consistent simulations of the dynamical episodes are, however, not yet possible on the scale of the Galaxy. N -Body simulations (even with cutting-edge special purposes computers like GRAPE-6 (Makino 2001)) cannot follow the evolution of a galactic nucleus over a Hubble time if relaxation is appreciable (Freitag & Benz, 2002).

Under certain assumptions and for some range of initial parameters, less realistic but more efficient Monte Carlo numerical simulations of the evolution of the GC (Freitag & Benz, 2002) showed that the SBHs sink to the centre on a short timescale of a few gigayears, settle into a centrally concentrated distribution and dominate the stellar mass there. Similarly, Murphy Cohn & Durisen (1991, see their figure 8b) showed that densities higher than $10^9 M_{\odot} \text{pc}^{-3}$ could reside in regions as close as few mpc from the central SBH. Other studies by Morris (1993) and Miralda-Escudé & Gould (2000) estimate that $10^4 - 10^5$ SBHs, due to dynamical friction, would have accumulated at distances of less than about 1 pc from the centre. These latter works can only account for about $10^2 - 10^4 M_{\odot}$ within separations of about 20 mpc from the centre which represents only 1% to 10% of our upper mass limit derived from the orbit of S2. However, the central density of the SBH cluster depends on various uncertain quantities: the SBH mass function, the stellar IMF and formation rate, the remnant progenitor masses, and the dynamical age of the GC. Morris (1993) argued that within a wide range of assumptions about the IMF, and about the minimum stellar mass capable of producing a black hole remnant, the total mass of remnants concentrated into the inner few tenth of a parsec, would be about $0.4 - 5 \times 10^6 M_{\odot}$. If the black hole remnants were to achieve equipartition with the field stars, they would form an inner core with a radius of a size as small as 50 mpc. These would coalesce or form a quasi-stable cluster of SBHs. Even if a catastrophic merger of stellar remnants did occur at some point at the age of the galactic nucleus, the continuous influx of massive stellar remnants would ensure that a concentrated population of them is present within the stellar core. These findings apply, however, in the absence of an initial central black hole. For the moment, a similar study of a cluster with already a pre-existing SMBH, as in the centre of our Galaxy, is not yet available.

In situ formation of stellar remnants

In the case of the Galactic Centre, complex dynamical episodes have taken place. A numerous variety of young early-type, bright and massive stars exist at distances of 10 mpc - 400 mpc from the centre (see section 3.2). There exist a dozen of bright O/B main sequence stars within about 40 mpc of Sgr A*, these are fast moving S-stars (mass $\sim 20 M_{\odot}$) of which the star S2 is an example. There exists also ~ 30 more massive ($30 M_{\odot} \lesssim \text{mass} \lesssim 100 M_{\odot}$) very bright early-type stars, the so-called He stars exhibiting He/HI emission lines (see section 3.2.1). The existence of these two types of stars at these regions from the centre is still not understood. These could have formed there or would have migrated there due to different in-spiraling processes (Genzel et al. 2003; Ghez et al. 2003; Gerhard et al. 2001, Krabbe et al. 1995). If such stars were always

present in the centre of the Galaxy, due to stellar evolution, their remnants would contribute very efficiently to the formation of a dense cluster also at the centre. Here, it is assumed that these stars would end their lives in the formation of NSs or SBHs with masses between $1.5 M_{\odot}$ and $10 M_{\odot}$ (on average $7 M_{\odot}$), their lifetimes are also considered to be $\lesssim 10^7$ yrs. If after a single lifetime about 40 of such stars form stellar remnants, throughout the age of the Galaxy ($\sim 10^{10}$ yrs), it is possible to account for about $10^5 M_{\odot}$ needed to explain the upper mass limit found for the 'inner cusp'.

Considering the two above described scenarios - while these do not represent the complete history of the galactic nucleus - it is, however, a fair conclusion that *strong* to *moderate* dynamically caused M/L variations prevail at the GC.

The aim of this work does not extend to the formation of a high density cluster of stellar remnants at the GC. In the following, I investigate if such a hypothetically high M/L configuration of stellar remnants can form a stable configuration.

8.2.1 Stability of a cluster of stellar remnants

Rauch & Tremaine (1996) studied the configuration of a central massive black hole plus an extended mass distribution M of radius R consisting of objects with mass m in terms of its *non - resonant* relaxation time t_{rel}^{nr} .

Under the assumption that $M \ll M_{BH}$, Rauch & Tremaine (1996) derive how t_{rel}^{nr} depends on M_{BH} , M , and the orbital time scale t_{orb} at the outer edge of the cluster. If (a) the stellar orbits have random orientations and moderate eccentricities, (b) the density of stars is approximately uniform within R , and (c) $M_{cluster} / M_{BH} = 10^{-2} - 10^{-5}$ then Rauch & Tremaine (1996) find that

$$t_{rel}^{nr} \sim \frac{M_{BH}^2}{m^2 N \ln \Lambda} t_{orb}, \quad (8.1)$$

where $\ln \Lambda$ is the Coulomb logarithm ~ 13 in this case. This situation should - to first order - be applicable to the black hole/cusp scenario at the Galactic Centre. Condition (a) is probably fulfilled with the possible exception that the stars in the cusp might have fairly high eccentricities (Schödel et al. 2003). Assuming a Plummer model as a cusp description fulfils condition (b). For the upper limit found on the cusp mass of $\leq 15\%$, M/M_{BH} is of the order of 10^{-2} , if restricted to the region within the core radius R_1 . This is close to what is required by condition (c).

Here, $M_{BH} = 3.65 \times 10^6$ and m_{sr} is the average mass of the stellar remnants. A value of $m_{sr} = 5 M_{\odot}$ is roughly consistent with a composite cluster made of NSs ($m \sim 1.5 M_{\odot}$) and SBHs ($5 M_{\odot} < m < 25 M_{\odot}$). Under the assumption that most of the mass inside the core radius is present in the form of stellar remnants of average mass m_{sr} , $t_{rel}^{nr} \sim 10^6 \times t_{orb}$. Considering that the core radius of 15-20 pc will define t_{orb} , t_{rel}^{nr} will be about 2×10^7 years.

It is possible to investigate whether such a configuration is stable by estimating how many stellar black holes evaporate. Integrating a Maxwell distribution function for the velocities

above the escape velocities gives the percentage of stars not bound to the BH. For the velocity dispersion, following Alexander et al. (2003), one can write:

$$v_{escape} = \sqrt{2}v_{circular} = \sqrt{2(1 + \alpha)} \sigma. \quad (8.2)$$

For a value of $\alpha = 2$, about 0.03% of the present stellar black holes will be evaporated after each relaxation time. For a steeper cusp with $\alpha=3$, 0.006% of the stellar black holes will evaporate on that time scale. For t_{rel}^{nr} of a few 10^7 years and α between 2 and 3 about 50% of the stellar black holes will have evaporated after 25 to 250 t_{rel}^{nr} corresponding to about 5×10^8 to 5×10^9 years. Given the fact that there will also be an influx of mass i.e. SBHs or NSs from outside the cusp one can consider such a configuration stable over a significant fraction of the Milky Way's age (see Mouawad et al. 2005).

Given equation 8.1, for a fixed t_{orb} , and with a given M , the relaxation time decreases linearly with N , i.e with the cusp mass. Thus, cusp masses well exceeding $2 \times 10^5 M_{\odot}$ would not form a stable configuration compared to the age of the Milky Way.

8.2.2 Stability of a cluster of intermediate mass black holes

Another possible form of the dark mass at the GC is the presence of a cluster of intermediate mass black holes (IMBH). This possibility is motivated by the findings of Paumard et al.(2004) of the possible existence of an IMBH at the centre of the compact cluster IRS 13E located approximately 3.6" south-west of Sgr A* (see section 3.2.2). This detection plays in favour of a scenario, first suggested by Gerhard (2001), in which the helium stars and the other hot stars in the central parsec originate from the stripping of a massive cluster formed several tens of pc from the centre. This cluster would have spiralled towards Sgr A* and IRS 13E would be its remnant. Furthermore, IRS 13E might be the second black hole needed according to a model by Hansen & Milosavljević (2003) to drag massive main-sequence stars, in the required timescale, very close to the massive black hole.

Numerical modelling by Portegies Zwart & McMillan (2002) showed that an IMBH with masses ranging between 10^3 and $10^4 M_{\odot}$ could form by runaway growth in massive, young stellar clusters as a result of stellar collisions in the dense cluster centre. They also argue that the accumulation at the centre of a galaxy of many IMBHs produced through this runaway process in nearby young star clusters (like the Arches and Quintuplet clusters in our Galaxy) provides an interesting new way of building up the mass of a central SMBH. Hansen & Milosavljević (2003) also discuss that it is possible that this process of accumulation is still ongoing in our own Galaxy.

As an application to the results on the non-Keplerian orbital modelling of the star S2, as presented in this work, I studied the stability of a cluster of IMBHs by estimating its evaporation time the way discussed in section 8.2.1. It results that a cluster of IMBHs cannot form a stable configuration over a considerable fraction of the age of the Milky Way. Reid et al. (2004) exclude the existence of IMBHs more massive than $10^4 M_{\odot}$ between roughly 10^3 and 10^5 AU (5 mpc and 500 mpc) from Sgr A* (see next section). As an example, I present the case of a cluster of $\sim 10^5 M_{\odot}$ formed by ~ 100 IMBHs with masses about $10^3 M_{\odot}$, the corresponding

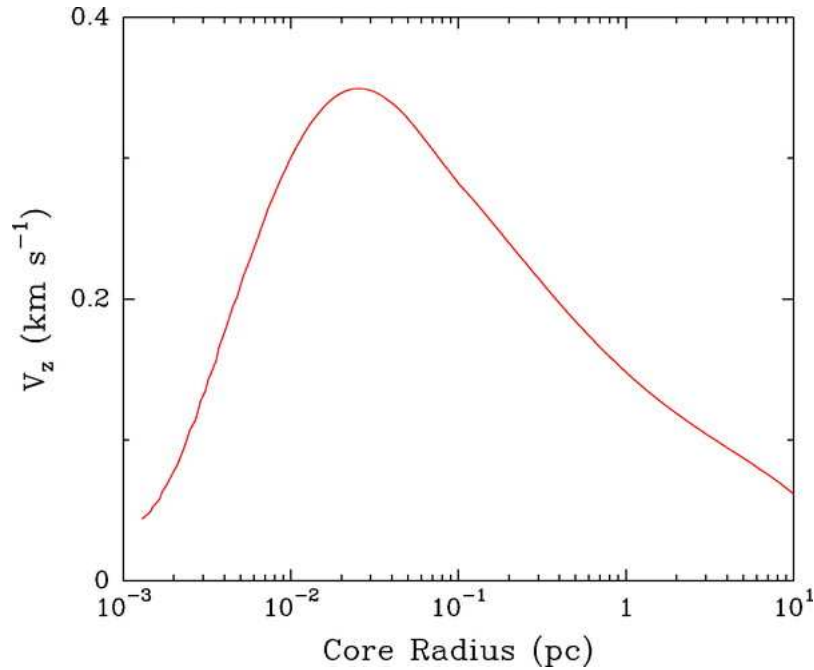


Figure 8.3: Motion of Sgr A* due to gravitational forces of random stellar orbits (Reid et al. 2004). Results of direct simulations of the motion of Sgr A*, owing to the gravitational forces of random stellar orbits, for a hypothetical cluster of stellar remnants. The stellar cluster was assumed to contain $0.4 \times 10^6 M_{\odot}$ with Plummer radial distribution. The line traces the simulated rms of one component of the velocity of Sgr A* as a function of the core radius of the Plummer-model distribution. For core radii less than about 0.03 pc, the velocity obtained by fitting a straight line to positions over an 8 yr period, similar to the observations, is smaller than the instantaneous velocity owing to rapid fluctuations in position caused by stellar remnants with orbital periods less than 16 yr.

relaxation time is only about 10^5 years, smaller by an order of 2 magnitudes than for that of a cluster of stellar remnants. This, leaving a cluster of stellar remnants as the only plausible interpretation of the upper-limit on the extended mass fraction if existent at the GC.

8.3 Brownian Motions of the SMBH

It is important to investigate other constraint on Sgr A*'s motion. If a cluster of stellar remnants should be present at the GC, it would effect the motion of Sgr A*. Random distributions of stars orbiting Sgr A* will produce small time-variable asymmetries in the mass distribution, which lead to small motions of Sgr A* about the centre of mass of the system.

Reid et al. (2004) studied such a behaviour in application to the 'inner cusp' configuration as discussed in this thesis, in order to quantify the motion of Sgr A* under the influence of a

compact cluster of stellar remnants. They considered dark clusters of stellar remnants totalling $0.4 \times 10^6 M_{\odot}$ containing 50% NSs of $1.4 M_{\odot}$ and 50% SBHs with a uniform distribution of masses between 3 and $25 M_{\odot}$. The core radius of the cluster was varied and large numbers of random simulations were evaluated to determine the rms velocity of a $3.6 \times 10^6 M_{\odot}$ SMBH. They calculated the position of Sgr A* at time intervals of 8 years and differenced these to determine the corresponding velocity, and compared these with their observations.

Their simulation results are shown in Figure 8.3. A cluster of only 5×10^4 dark stellar remnants containing $0.4 \times 10^6 M_{\odot}$ could induce velocities greater than 0.3 km s^{-1} to one component of the measured motion of Sgr A*. A core radius of 15.5 mpc plus a black hole mass of $3.6 \times 10^6 M_{\odot}$, will induce a one-dimensional rms motion of 0.34 km s^{-1} on Sgr A*. Furthermore, over a wide range of core radii from about 0.004 to 0.4 mpc, such a cluster could increase the velocity with roughly more than 0.2 km s^{-1} . By applying these calculations to the central stellar cluster, which contains about 10^6 to 10^7 stars observed within 2 pc of Sgr A*, Reid et al. (2004) find a comparable contribution to the motion of Sgr A* from a cluster of dark stellar remnants. Using observational data (see section 3.3), they also determine an upper limit on the intrinsic proper motion of the SMBH at the GC of 18 km s^{-1} . This implies a lower limit on the mass of Sgr A* of $\sim 5 \times 10^5 M_{\odot}$, the latter being subject to the orbital motion of the surrounding stellar cluster.

A contribution from such a cluster of dark stellar remnants (0.3 km s^{-1}) would increase the estimate on the lower limit of the mass of Sgr A* to 0.7×10^6 or $1.7 \times 10^6 M_{\odot}$ instead of $\sim 5 \times 10^5 M_{\odot}$. Thus, there is no contradiction for the existence of such a cluster close to Sgr A*.

8.4 Comparison with Observational Results

Detection of stellar remnants through X-ray emission

A systematic X-ray survey of the Galactic Centre region at sub-arcsecond scale with Chandra by Munro et al. (2003) over a field of $17' \times 17'$ centred on Sgr A* has revealed more than 2000 discrete X-ray sources. Stellar remnants, WDs with magnetically accreting disks, binaries with NSs or SBHs are considered as responsible for a large fraction of these discrete sources. Their density distribution peaks in the central parsec.

Later, Munro et al. (2004) identified seven X-ray transients located within 23 pc of Sgr A*. Their variable X-ray luminosities showing peaks $> 5 \times 10^{33} \text{ erg s}^{-1}$ suggests that these are accreting SBH or NS.

Transients show peak luminosities intermediate between those typically considered outburst and quiescence phases of X-ray binaries. Remarkably four of these transients lie within only 1 pc of Sgr A*. This implies that, compared to the numbers of similar systems located between 1 and 23 pc, transients are over-abundant by a factor of ~ 20 per unit stellar mass within 1 pc of Sgr A*. The excess transient X-ray sources are low-mass X-ray binaries that were produced, as in the cores of globular clusters, by three-body interactions between binary star systems and either SBHs or NSs that have been concentrated in the central parsec through dynamical friction. Alternatively, they could be high-mass X-ray binaries that formed among the young stars that are present in the central parsec.

As mentioned earlier, Morris (1993) and Miralda-Escudé & Gould (2000), propose that

about 10^4 SBHs and NSs could possibly be present within 1 pc of Sgr A*, mostly driven there by dynamical friction. Under different assumptions on the initial mass function (IMF) at the GC, the binary density, binary forming rate, and binary lifetime, Munro et al. (2004) argue that the observed X-ray binary transients could explain the presence of the above mentioned 10^4 remnants. Unfortunately, very few such faint transients ($L_X < 10^{36}$ erg s^{-1}) have ever been detected before, so there are no reliable estimations on how often any one of them will become active. In the rest of the Galaxy, it is estimated that 1% of X-ray binaries has become brighter than 10^{36} erg s^{-1} in the past 30 years. A crude estimate would be that only about 0.1% to 10% of these sources were detected (Munro, private communication). Therefore, this doesn't contradict the higher abundance of these sources in the inner regions of the central cluster as argued in this thesis.

The detected transients were all at least as bright as Sgr A*. The non-identification of any transient in the inner 40 mpc indicate that (active) transients are not abundant at these separations from Sgr A*. This is however not surprising since the binary lifetime at separations of \sim mpc is expected to be very short in the strong tidal field of the SMBH.

Future detection of gravitational waves emission ?

The hypothetical presence of a cluster of stellar remnants have potentially important implications for the study of SMBHs by the Laser Interferometer Space Antenna (LISA), since the in-spiral of SBHs into a SMBH generate the best source of low-frequency gravitational waves detectable with LISA (Sirgudsson & Rees 1997, Freitag et al. 2003).

These authors predict different detection rates due to in-spirals of SBHs NSs, WDs, and main sequence stars (MSS) into the Galactic SMBH. For SBHs and NSs, the rates vary between 0.01 detection (for Freitag et al. 2003) and 10 detections (Sirgudsson & Rees 1997) over the whole year of the LISA observation. Whereas for MSS, only estimations from Freitag et al. (2003) predict a rate of less than 10 detections.

Here, I argue that if, as discussed in section 8.2, a dense cluster of < 30000 stellar remnants were to be present on the scale of 20 mpc, than a higher detection rate (> 10 detections) of gravitational waves would be expected from the SBHs and NSs. Therefore, the observations with LISA could give us conclusive answers about the presence of stellar remnants at the GC.

Chapter 9

Summary

This work concerns the stellar dynamics in the vicinity of the central Galactic black hole, it adds to our understanding on the growth to SMBHs and their interplay with their host galaxy. The Milky Way is an ideal object to study the dynamics of stars close to a SMBH since it is the nearest object, meaning that information on the stellar components in the nuclear region can be obtained in such a detail that is impossible for any other galaxy.

More than twelve years of regular observations of the Galactic centre (Eckart et al. 1995, 1997; Genzel et al. 1996, 1997, 2000, 2003; Ghez 1998, 2000, 2003, Eisenhauer 2005) have given rise to a unique picture of stellar orbits around a SMBH present at the position of the radio source Sgr A*. These are orbits of bright O/B main sequence stars existing within about only 40 mpc from Sgr A*. They form a group of about 12 stars of $\sim 20 M_{\odot}$ (Eisenhauer et al. 2005) and are nominated by the S-stars. This thesis aims to exploiting the potential close the Galactic black hole by studying the dynamics of the stars governed by it. It is the first study where stellar orbits are modelled under the potential of a hypothetical dark extended mass distribution, and fitted to observational positional and radial velocity data.

Star S2, shows the shortest orbital period and the most complete orbit. Among the S-stars it is the unique candidate capable to provide informations about the distribution of the extended mass fraction in the GC.

In this work, high-resolution NIR observations of the nuclear star cluster obtained with SHARP at the ESO NTT and NAOS/CONICA at the ESO VLT, at the diffraction limit of 4-8 meter class telescopes, are used. The NIR imaging data acquired with the new NIR camera and adaptive optics system NAOS/CONICA at an 8 m class telescope allowed additional fundamental observations due to its high sensitivity, large field-of-view, and its exceptional ability to exploit the resolution of an 8m-class telescope.

The observed high increase of the surface stellar density at distances of ~ 20 mpc from the SMBH proposes the presence of a distinct dense core, superimposed over a larger scale cluster. In contrast to Genzel et al. (2003) who model the inner surface density by a power-law profile, in this work, the inner region is represented by a compact Plummer-law profile. It is nominated by the 'inner cusp' throughout this work, has a core radius of 20 mpc and extends to regions outside its core radius. The mass distribution, following the stellar light curve, is represented

according to these two different profiles which fit the number density counts very well.

Under the assumption that the dark mass follows the stellar light curve, it was shown that a considerable amount of not-yet-detected extended mass could be hidden in the vicinity of the black hole. Using dynamical mass estimates at different separations from the centre, it is possible to scale the resulting mass distribution function, and fit it to these mass estimates. This gives the amount of enclosed mass in function of separation from the centre. By determining the mass distribution this way, there goes the implicit assumption of a constant mass-light-ratio, $M/L(2\mu\text{m}) = 2(M/L)_{\odot}(2\mu\text{m})$, the one measured at large distances from the centre. However, due to mass segregation, massive stellar components could sink into the centre and dominate the mass inside. This leads to higher central values of the M/L . This work shows the first approach in which the M/L is not assumed to be constant overall the central stellar cluster.

The scenario of the presence of stellar remnants at the GC was first proposed by Morris et al. (1993). It was argued that the presence of stellar remnants at the GC can be due to inward migration of compact objects caused by dynamical friction and also due to stellar evolution of massive stars present close to the centre.

A fourth order Hermite integrator optimized for our purposes is used to integrate the path of the star S2 in the central mass plus the extended mass potential. A grid method developed in the framework of this thesis is used to fit the observational positional and radial velocity data to the S2-orbit. A wide coverage of the parameter space is allowed. The mass of the cusp is varied as a fraction of the total central mass. This modelling results in an estimation of an upper limit on the extended mass fraction. It is set using two constraints: the data on the S2 star and the limit of the enclosed mass at larger radii derived from various dynamical mass estimates.

It is found that at a 1σ level the cusp mass could attain 15% of the total central mass of $4.1 \times 10^6 M_{\odot}$ (in this case, $M/L(2\mu\text{m}) \sim 140 (M/L)_{\odot}(2\mu\text{m})$), and at a 3σ level 25% of the total central mass of $4.8 \times 10^6 M_{\odot}$ (in this case, $M/L(2\mu\text{m}) \sim 270 (M/L)_{\odot}(2\mu\text{m})$). However, with the available data, it is not yet possible to discriminate between point-mass and non-point-mass potentials. Similarly, due to degeneracy in the free fit parameters, the mass distribution function and the core radius of the used model are not yet discernable. This result agrees with the conclusions of Rubilar & Eckart (2001) that, at least three orbits are needed in order to determine the true mass distribution function, its extension and its amount.

The results on non-Keplerian orbital fitting imply that inside the radius of 20 mpc, there could exist a mass as high as $\sim 10^5 M_{\odot}$. Such a high mass fraction gives high central densities of the order of $10^9 M_{\odot} \text{pc}^{-3}$. The existence of such a dark and dense core is investigated considering the presence of faint, low-mass main sequence stars and stellar remnants.

The magnitude limit detected with NAOS/CONICA is $K = 18$, it corresponds to $\sim 2 M_{\odot}$. Fainter stellar components ($K \leq 25$ mag), that could be present in the centre are studied in detail. The observed K-band luminosity function together with stellar counts are analysed. It is found that stellar components cannot account for the presence of such a high fraction of mass at the centre, the maximum attained M/L doesn't exceed the value of $4 (M/L)_{\odot}(2\mu\text{m})$. Moreover less massive stars are not expected to reside in the innermost central regions of a galaxy.

Such a fraction, if present, could probably be constituted by a heavier component, like stellar

black holes or neutron stars. Considering the puzzling complexity of the Galactic Centre region, it is possible to argue for a probable existence of a stellar remnants component, high enough to account for the upper mass limit required from the S2-orbit modelling. This fraction can be due to stellar evolution of in situ young massive stars and to segregating massive compact remnants from the outer regions.

The evaporation time of an 'inner-cusp' formed by stellar remnants in the presence of a SMBH is approached by applying the Maxwell distribution function. It is found that such a configuration could form a stable configuration over fractions of the age of the Milky Way.

Appendix A

List of Abbreviations/Orbital Parameters

A.1 List of Abbreviations

AO	Adaptive Optics
ESO	European Southern Observatories
FOV	Field-of-View
FWHM	Full Width at Half Maximum
GC	Galactic Centre
HB	Horizontal Branch
IMBH	Intermediate Mass Black Hole
IMF	Initial Mass Function
KLF	K-band Luminosity Function
MSS	Main Sequence Star
NACO	NAOS/CONICA
NIR	Near Infrared
NS	Neutron Star
PSF	Point Spread Function
SED	Spectral Energy Distribution
Sgr A*	Sagittarius A*
SMBH	Super-massive Black Hole
SBH	Stellar Black Hole
SSA	Simple Shift-and-Add
WD	White Dwarf

A.2 Orbital Parameters

Table of the orbital parameters of the orbits within a 1σ limit. The full parameter range [Min;Max] that produces $\tilde{\chi}^2_{tot} \leq 1.45$ orbital fits for S2 is also given. The orbits corresponding to those fits have the smallest $\tilde{\chi}^2_{tot}$ and correspond to the case where the central mass is at the position, a , b , c , d and *offset* position (see Fig 6.3 and Table 7.1). Three exemplary orbits at the *offset* position are plotted in Fig 7.3. Here, orbital fits with $M_{tot} > 5.4 \times 10^6 M_{\odot}$ are excluded.

Table A.1: Orbital parameters I.

BH Position in mpc (R.A,Dec)	offset	offset	offset	offset	a(0,0.05)	a(0,0.05)	b(-0.05,0)
Total Mass M_{tot} ($10^6 M_{\odot}$)	3.65	4.10	4.45	4.80	3.65	4.1	3.65
Point Mass M_{BH} ($10^6 M_{\odot}$)	3.65	3.69	3.56	3.65	3.47	3.49	3.65
Cusp Percentage(%)	0	10	20	25	5	15	0
M^{apo} :Cusp mass \in S2's orbit ($10^6 M_{\odot}$)	0.001	0.049	0.105	0.133	0.02	0.072	0.001
e : Eccentricity	0.88	0.882	0.884	0.881	0.884	0.883	0.88
i : Inclination($^{\circ}$)	-47.89	-47.88	-48.26	-48.12	-48.0	-47.72	-48.23
a : Semi-major axis(mpc)	4.65	4.66	4.63	4.59	4.63	4.63	4.7
T : Time of peri-centre passage	2002.327	2002.328	2002.333	2002.333	2002.336	2002.336	2002.327
Ω : Angle of line of nodes($^{\circ}$)	45.3	45.38	44.47	44.59	43.29	43.13	44.49
ω : Angle of nodes to peri-centre($^{\circ}$)	245.1	244.84	245.26	245.6	246.54	246.56	245.22
P : Period (Years)	15.55	15.43	15.48	15.06	15.83	15.65	15.8
Peri-Centre distance	0.557	0.552	0.535	0.55	0.538	0.539	0.565
$\Delta\alpha$: Pericentre-shift per revolution	0 $^{\circ}$ 0'00"	0 $^{\circ}$ 40'48"	1 $^{\circ}$ 28'48"	1 $^{\circ}$ 52'43"	0 $^{\circ}$ 19'12"	1 $^{\circ}$ 3'36"	0 $^{\circ}$ 00'00"

Table A.2: Orbital Parameters II

BH Position in mpc (R.A,Dec)	c(0,-0.05)	c(0,-0.05)	c(0,-0.05)	d(0.05,0)	d(0.05,0)	d(0.05,0)	Min	Max
Total Mass M_{tot} ($10^6 M_{\odot}$)	3.65	4.1	4.8	3.65	3.65	4.1	3.28	5.40
Point Mass M_{BH} ($10^6 M_{\odot}$)	3.65	3.69	3.65	3.65	3.47	3.49	3.28	3.97
Cusp Percentage(%)	0	10	25	0	5	15	0	35
M^{apo} :Cusp mass \in S2's orbit ($10^6 M_{\odot}$)	0.001	0.05	0.14	0.001	0.022	0.071	0	0.26
e : Eccentricity	0.883	0.884	0.885	0.884	0.888	0.886	0.868	0.897
i : Inclination($^{\circ}$)	-48.31	-48.15	-48.29	-47.39	-48.04	-47.77	-46.86	-50.19
a : Semi-major axis(mpc)	4.7	4.7	4.67	4.62	4.68	4.59	4.52	4.79
T : Time of peri-centre passage	2002.329	2002.330	2002.331	2002.338	2002.337	2002.339	2002.327	2002.337
Ω : Angle of line of nodes($^{\circ}$)	45.39	45.34	45.66	44.31	4.46	44.24	42.17	46.1
ω : Angle of nodes to peri-centre($^{\circ}$)	244.8	244.77	244.58	246.35	245.93	246.19	244.1	247.7
P : Period (Years)	15.80	15.63	15.41	15.41	16.07	15.49	14.61	16.67
Peri-Centre distance	0.548	0.545	0.537	0.537	0.522	0.523	0.511	0.6
$\Delta\alpha$: Pericentre-shift per revolution	0 $^{\circ}$ 0'00"	00 $^{\circ}$ 41'24"	1 $^{\circ}$ 53'24"	0 $^{\circ}$ 00'00"	0 $^{\circ}$ 19'23"	1 $^{\circ}$ 02'20"	0 $^{\circ}$ 00'00"	3 $^{\circ}$ 07'12"

Appendix B

De-projection of the K-band Luminosity Function

The observed K-band luminosity function (KLF), as used in this work, gives the number of sources, $dN_p(K, r)$, per square arcsecond, ds^{-1} , per magnitude, dK^{-1} : $dN_p/ds dK$. One would like to find the number of stars $N(K, r)$ present in a unit volume of the same radius r , $V(r)$. Therefore, a conversion of the observed KLF to a local 'volume density' KLF is necessary, i.e., a de-projection of the KLF.

If the distribution of the particles (stars) is a composite Plummer-like mass distribution, as assumed in this work, it is possible to find a relation between the integrated mass, $M(r)$ (in a volume, $V(r)$), and the integrated mass $M_p(r)$ seen in projection on a surface on the sky in the same radius, r .

The mass surface density, and volume density distribution of a Plummer model and the here used 'composite model' are given in equations 4.1, 4.2, 4.3, and 4.4.

The projected mass distribution can be integrated following the relation below (Spitzer et al. 1975):

$$M_p(r) = 2\pi \int_0^r \sigma(r') r' dr', \quad (\text{B.1})$$

Thus, for a simple Plummer model one finds,

$$M_p(r) = M_{tot} \frac{r^2}{R^2 + r^2}, \quad (\text{B.2})$$

This leading to the relation below between $M(r)$ and $M_p(r)$,

$$\frac{M(r)}{M_p(r)} = \frac{r}{\sqrt{R^2 + r^2}}. \quad (\text{B.3})$$

However, the 'composite model', as given in equation 4.4 can be written in this form,

$$\sigma(r) = \sum_{i=1}^6 \sigma_i(r) \quad ; \quad M(r) = \sum_{i=1}^6 M_i(r)$$

the summation above applies also to the projected mass, leading to

$$M_p(r) = \sum_{i=1}^6 M_{p_i}(r). \quad (\text{B.4})$$

thus, the projected mass and the 3-dimensionnal mass distribution will follow equation 9.5 below

$$\frac{M(r)}{M_p(r)} = \frac{\sum_{i=1}^6 M_{(tot)_i}(r) \frac{r^3/R_i^3}{(1+r^2/R_i^2)^{3/2}}}{\sum_{i=1}^6 M_{(tot)_i} \frac{r^2}{R_i^2+r^2}}. \quad (\text{B.5})$$

So that there exists a relation $M(r) = f(M_p(r))$.

On the other hand, Genzel et al. (2003) give the number of stars N_p per $(1.5'')^2$ at different magnitudes K . This same equation 9.5 between $M(r)$ and $M_p(r)$ applies between $N(r)$ and $N_p(r)$, since $M(r) \propto N(r)$. This, making it possible to find the number of stars $N(1.5'')$ in a volume $V(1.5'')$, given the number of stars $N_p(1.5'')$ projected on the sky in a radius of $1.5''$.

It is possible to extrapolate these values to different radii, by simply applying the equation:

$$\frac{N(r)}{N(1.5'')} = \frac{\sum_{i=1}^6 \rho_i(r)}{\sum_{i=1}^6 \rho_i(1.5'')} \frac{r^3}{1.5^3}. \quad (\text{B.6})$$

Finally, with the equation 9.5 and equation 9.6, it is possible to calculate the number of stars in a volume for any radius r from the $N_p(1.5'')$ given by Genzel et al. (2003).

Appendix C

K-band magnitude/Stellar masses

In order to study the $M/L(2\mu m)$ ratio, it is necessary to estimate the mass corresponding to each observed K-band magnitude of the individual stars. The different Luminosity classes, V (main sequence stars), III (giants) and I (supergiants) were considered. These offer a good coverage of the complexity of the stellar constituents of the central cluster. For a range of spectral classes, Johnson (1966), Kenneth (1991) and Binney & Merrifield (1998) give, under the standard MK spectral classes classifications, estimations on the stellar mass and radius of some stars in relation to their spectral class, their absolute visible magnitude M_V and the color ($V - K$). These are listed in Table C.1 for the available spectral types.

S_k is the flux density and is given by:

$$S_k = 10^{\epsilon - 0.4m}$$

Johnson (1966) gives $\epsilon = 2.8$ for the K -band. m corresponds to the apparent magnitude in K of a certain source.

Luminosities are related to flux densities via:

$$L = 4\pi d^2 \times S_k,$$

where $d = 8 \text{ kpc}$ being the distance to the Galactic Centre. The extinction towards the GC in the K -band is considered to be equal to 3 magnitudes, $A_K=3$. Using the equations above, it is possible to estimate, for each given K-band magnitude, the corresponding Luminosity in the K-band and to associate the given stellar mass to it.

Table A.2 given below lists the obtained masses in solar masses, for the corresponding Class of luminosity and spectral type. The V and K are the absolute magnitudes in the visible and the K-band wavelength respectively. The apparent magnitudes listed here are not corrected for the extinction.

The mass-to-light ratios are then simply computed via:

$$M/L(2\mu m) = \frac{\sum_i N_i \times M_i}{\sum_i N_i \times L_i}, \quad (\text{C.1})$$

where N_i is number of stars per magnitude K . These values are computed for different apparent magnitudes limits ($K \leq 25$) and listed in Table 8.2.

Table C.1: Stellar masses corresponding to K-band magnitudes.

N	C	Spectral type	M_V	(V-K)	mk	M_{\odot} (l)
1	V	O6	-5.5	-0.93	9.945	37
2	V	O8	-4.9	-0.93	10.545	23
3	V	O9	-4.5	-0.89	10.905	19
4	V	B0	-4.0	-0.85	11.365	17.5
5	V	B1	-3.2	-0.76	12.075	13
6	V	B2	-2.4	-0.67	12.785	9.8
7	V	B3	-1.6	-0.57	13.485	7.6
8	V	B5	-1.2	-0.43	13.745	5.9
9	V	B8	-0.2	-0.25	14.565	3.8
10	V	A0	0.6	0.0	15.115	2.9
11	V	A5	1.9	0.35	16.065	2.0
12	V	F0	2.7	0.79	16.425	1.6
13	V	F5	3.5	1.01	17.005	1.4
14	V	G0	4.4	1.22	17.695	1.05
15	V	K0	5.9	1.75	18.665	0.79
16	V	K5	7.4	3.00	18.915	0.67
17	V	M0	8.8	3.25	20.065	0.51
18	V	M2	9.3	3.75	20.065	0.4
19	V	M3	10.4	4.00	20.915	0.33
20	V	M5	12.3	4.5	22.315	0.21
21	V	M7	14.3	5.00	23.815	0.12
22	V	M8	16.0	5.25	25.265	0.06
23	III	G0	1	1.75	13.765	1.0
24	III+	K0	0.7	2.33	12.885	1.1
25	III+	K5	-0.2	3.74	10.575	1.2
26	III+	M0	-0.4	3.8	10.315	1.2
27	III+	M2	-0.6	4.23	9.685	1.3
28	I	O9	-6.5	-0.82	8.835	19
29	I	B0	-6.4	-0.7	8.815	25
30	I	B5	-6.2	-0.13	8.445	20
31	I	A0	-6.3	0.21	8.005	16
32	I	A5	-6.6	0.36	7.555	13
33	I	F0	-6.6	0.63	7.285	12
34	I	F5	-6.6	0.93	6.985	10
35	I	G0	-6.4	1.44	6.675	10
36	I	K0	-6.0	2.16	6.355	13
37	I	K5	-5.8	3.7	5.015	13
38	I	M0	-5.6	3.82	5.095	13
39	I	M2	-5.6	4.31	4.605	19
40	I	M5	-5.6	6.3	2.615	24
41	IIIa	M5	-0.3	5.96	8.255	1.05
42	IIIb	M5	-0.3	5.96	8.255	1.4

Bibliography

- [1963] Aarseth S. J., 1963, MNRAS, 126, 223
- [1985] Aarseth S. J., 1985, in Brackhill J. U., Cohen B. I., eds, Multiple Time Scales. Academic Press, New York, p.377
- [1999] Aarseth S. J., 1999, CeMDA 73, 127
- [1999] Aarseth, S. J. 1999, Pub. Astron. Soc. Pac , 111, 1333
- [2003] Aarseth, S. J. 2003, in P.V. Landshoff, D. R. Nelson, S. Weinberg, eds, 'Gravitational N-Body Simulations'. Cambridge University Press.
- [1999] Alexander, T. 1999, ApJ, 527, Issue 2, 835
- [1999] Alexander, T. & Sternberg, A., 1999, ApJ, 520, 137A
- [2003] Alexander, T. 2003, In: The Galactic black hole. Lectures on general relativity and astrophysics. Edited by Heino Falcke; Friedrich W. Hehl. Series in high energy physics, cosmology and gravitation. Bristol: IoP, Institute of Physics Publishing, ISBN 0-7503-0837-0, 2003, p. 246-274
- [1986] Allen, D. A. & Sanders, R. H., 1986, Natur, 319, 191-194
- [1990] Allen, D. A.; Hyland, A. R.; Hillier, D. J, 1990, MNRAS, 244, 706A
- [2004] Aschenbach, B., Grosso, N., Porquet, D., Predehl, P., A&A v.417, p.71-78
- [1999] Backer, D. C. & Sramek, R. A. , 1999, Volume 524, Issue 2, pp. 805-815.
- [2001] Baganoff, F. K.; Bautz, M. W.; Brandt, W. N.; Chartas, G.; Feigelson, E. D.; Garmire, G. P.; Maeda, Y.; Morris, M.; Ricker, G. R.; Townsley, L. K.; Walter, F., 2001, Natur, 413, 45B
- [2003] Baganoff, F. K.; Maeda, Y.; Morris, M.; Bautz, M. W.; Brandt, W. N.; Cui, W.; Doty, J. P.; Feigelson, E. D.; Garmire, G. P.; Pravdo, S. H.; Ricker, G. R.; Townsley, L. K., ApJ, Volume 591, Issue 2, pp. 891-915
- [1976] Bahcall, J. N. & Wolf, R. A., 1976, ApJ, vol. 209, p. 214-232.

- [1977] Bahcall, J.,N. & Wolf, R. A. 1977, ApJ, 216, 883b
- [1981] Bahcall, J. N. & Tremaine, S., 1981, ApJ; 244, 805
- [2003] Baumgardt, H., Hut, P., Makino, J., McMillan, S., & Portegies Zwart, S. 2003, ApJL, 582, L21
- [1978] Becklin, E. E., Matthews, K., Neugebauer, G. and Willner, S. P., 1978, ApJ, 219, 121-128
- [1969] Bevington, R., P. & Keith, R., D., 1969, 'Data Reduction and Error Analysis for the Physical Sciences', Published by MacGrawth Hill, New York
- [1998] Binney, J. & Merrifield, M., 1998, 'Galactic Astronomy', Princeton University Press.
- [1987] Binney, J. & Tremaine, S. 1987, 'Galactic Dynamics', Princeton Series in Astrophysics.
- [1996] Blum, R. D.; Sellgren, K.; Depoy, D. L., 1996, AJ, 112, 1988B
- [1983] Bohren, C.F. & Huffman, 1983, D.R. asls. book
- [1986] Butchart, I. McFadzean, A. D., Whittet, D. C. B. et al., 1986, A&A 154
- [1990] Catchpole, R. M.; Whitelock, P. A.; Glass, I. S., 1990, MNRAS, 247, 479
- [2002] Chiar, J.E., Adamson, A. J., Pendleton, Y. J. et al., 2002, ApJ 570, 198
- [1991] Christou, J. C., 1991, Exp. Astron., vol. 2, no. 1, 1991, p. 27-56
- [1999] Cotera, A.; Morris, M.; Ghez, A. M.; Becklin, E. E.; Tanner, A. M.; Werner, M. W.; Stolovy, S. R., 1999, 'The Central Parsecs of the Galaxy', ASP Conference Series, Vol. 186. Edited by Heino Falcke, Angela Cotera, Wolfgang J. Duschl, Fulvio Melia, and Marcia J. Rieke., p. 240
- [2003] Cuadra, J.; Nayakshin, S.; Sunyaev, R., 2003, A&A, 411, 405C
- [1984] Duley, W. W. & Williams, D. A., 1984, Natur 311, 685
- [1975] Dainty, J., C., 1975, 'Laser speckle and related phenomena', Topics in Applied Physics, Berlin: Springer, 1975, edited by Dainty, J.C.
- [1994] Diamond, P. J.; Kemball, A. J.; Junor, W.; Zensus, A.; Benson, J.; Dhawan, V., 1994, ApJ, 430, 61
- [2001] Doeleman, S. S.; Shen, Z.-Q.; Rogers, A. E. E.; Bower, G. C. et al., 2001, 2001, AJ, 121, 2610D
- [1992] Eckart, A., Genzel, R., Krabbe, A., Hofmann, R., van der Werf, P. P., and Drapatz, S., 1992, Natur 355, 526

- [1995] Eckart, A., Genzel, R., Hofmann, R., Sams, B. J. & Tacconi-Garman 1995, *ApJ*, 445, L23
- [1996] Eckart, A. & Genzel, R. 1996, *Nature*, 383, 415
- [1997a] Eckart, A. & Genzel, R., 1997. *MNRAS*, 284, 576
- [1997b] Eckart, A., Genzel, R., Hofmann, R., Drapatz, S., Katterloher, R., Quirrenbach, A., and Tacconi-Garman, L., 1997, proceedings of the ESO workshop, held at Garching, Germany, 18-21 June 1996, Publisher: Berlin, New York: Springer-Verlag, p.259
- [1998] Eckart, A., 1998, Habilitation
- [1999] Eckart, A., Ott, T., Genzel, R. 1999, *A&A*, 352L, 22E
- [2000] Eckart, A.; Hippler, S.; Glindemann, A.; Hackenberg, W.; Quirrenbach, A.; Kalas, P.; Kasper, M.; Davies, R. I.; Ott, T.; Rabien, S.; Butler, D.; Holstenberg, H.-C.; Looze, D.; Rohloff, R.-R.; Wagner, K.; Wilnhammer, N.; Hamilton, D.; Beckwith, S. V. W.; Appenzeller, I.; Genzel, R., 2000, *Exp. Phys.* v.10, Issue 1, p.1-3
- [2002a] Eckart, A., Genzel, R., Ott, T. & Schödel, R. 2002a, *MNRAS*, 331, 917
- [2002b] Eckart, A., Mouawad, N., Krips, M., Straubmeier, C., and Bertram, T., 2002, *SPIE* 4835-03, *Cnf. Proc. of the SPIE Meeting on 'Astronomical Telescopes and Instrumentation'*, held in Waikoloa, Hawaii, 22-28 August 2002b
- [2002c] Eckart, A., Bertram, T., Mouawad, N., Viehman, T., Straubmeier, C., Zuther, J. 2002, Contribution to the JENAM meeting on: The VLTI - Challenges for the Future, Porto, Portugal, September 4-7, 2002c
- [2003] Eckart, A., Moulataka, J. et al: accepted to *ApJ* (2003)
- [2003b] Eckart, A., Moulataka, J., Viehmann, T., Straubmeier, C., Mouawad, N., Genzel, R., Ott, T., Schödel, R., Baganoff, F. K., Morris, M. R., Proceedings of the Galactic Center Workshop 2002 - The central 300 parsecs of the Milky Way., 2003, *Astron. Nachr Suppl.*, 324, 557E
- [2004a] Eckart, A.; Moulataka, J.; Viehmann, T.; Straubmeier, C.; Mouawad, N., 2004, *ApJ*, Volume 602, Issue 2, pp. 760-769
- [2004b] Eckart, A.; Baganoff, F. K.; Morris, M.; Bautz, M. W.; Brandt, W. N.; Garmire, G. P.; Genzel, R.; Ott, T.; Ricker, G. R.; Straubmeier, C.; Viehmann, T.; Schödel, R.; Bower, G. C.; Goldston, J. E., 2004, *A&A*, v.427, p.1-11
- [2005] Eckart, A., Schödel, R., Straubmeier, C., 2005, 'The Exploration of the Supermassive Black Hole at the Center of the Milky Way', ICP (Imperial College Press), London, 2005

- [2003] Eisenhauer, F., Schödel, R., Genzel, R., Ott, T., Tecza, M., Abuter, R., Eckart, A. & Alexander, T. 2003, *ApJ*, 597, Issue 2, L121
- [2005] F. Eisenhauer, R. Genzel, T. Alexander, R. Abuter, T. Paumard, T. Ott, A. Gilbert, S. Gillessen, M. Horrobin, S. Trippe, H. Bonnet, C. Dumas, N. Hubin, A. Kaufer, M. Kissler-Patig, G. Monnet, S. Stroebele, T. Szeifert, A. Eckart, R. Schoedel, S. Zucker, 2005, submitted to *ApJ*, Astro-ph/0502129
- [2001] Ferrarese, L., Pogge, R. W., Peterson, B. M., Merritt, D., Wandel, A., & Joseph, C. L. 2001, *ApJL*, 555, L79
- [1998] Figer, D. F.; Najarro, F.; Morris, M.; McLean, I. S.; Geballe, T. R.; Ghez, A. M.; Langer, N., 1998, *ApJ*, Vol. 506, Issue 1, pp. 384-404.
- [2000] Figer, Donald F., Becklin, E. E., McLean, Ian S., Gilbert, Andrea M., Graham, James R., Larkin, James E., Levenson, N. A., Teplitz, Harry I., Wilcox, Mavourneen K. & Morris, Mark, 2000, *ApJ*, 533L, 49F
- [2003] Figer, Donald F.; Gilmore, Diane; Kim, Sungsoo S.; Morris, Mark; Becklin, E. E.; McLean, Ian S.; Gilbert, Andrea M.; Graham, James R.; Larkin, James E.; Levenson, N. A.; Teplitz, Harry I., 2003, *ApJ*, 599, pp. 1139
- [2000] Fragile, P.C. & Mathews, J., 2000, *ApJ* 542, 328
- [2002] Freitag, M. & Benz, W., 2002, *A&A*, 394, 345
- [2003] Freitag, M. 2003, *ApJ*, Volume 583, Issue 1, pp. L21-L24
- [1994] Genzel, R., Hollenbach, D. J., Townes, C. H., Eckart, A., Krabbe, A., Lutz, D. & Najarro, F.t., 1994, *NATO Advanced Science Institutes (ASI), Series C*, 445, 327
- [1996] Genzel R., Thatte N., Krabbe A., Kroker H. & Tacconi-Garman L. E., 1996, *ApJ*, 317, 153
- [1997] Genzel, R., Eckart, A., Ott, T., & Eisenhauer, F., 1997, *MNRAS*, 291, 219G
- [2000] Genzel, R., Pichon, C., Eckart, A., Gerhard, O. & Ott, T., 2000, *MNRAS*, 317, 348
- [2001] Genzel, R., 2001, *Dynamics of Star Clusters and the Milky Way*, ASP Conference Series, Vol. 228. Edited by S. Deiters, B. Fuchs, R. Spurzem, A. Just, and R. Wielen, p.291
- [2003] Genzel, R., Schödel, R., Ott, T., Eisenhauer, F., Hofmann, R., Lehnert, M., Eckart, A., Alexander, T., Sternberg, A., Lenzen, R., Clnet, Y., Lacombe, F., Rouan, D., Renzini, A. & Tacconi-Garman, L. E. 2003, *ApJ*, 594, Issue 2, 812
- [2003b] Genzel, R.; Schödel, R.; Ott, T.; Eckart, A.; Alexander, T.; Lacombe, F.; Rouan, D.; Aschenbach, B., 2003, *Natur*, 425, 934

- [2001] Gerhard, O., 2001, ApJ, 546, Issue 1, pp. L39
- [2002] Gezari, S., Ghez, A. M., Becklin, E. E., Larkin, J., McLean, I. S., Morris, M., 2002, ApJ, 576, 790G
- [1998] Ghez, A. M., Klein, B. L., Morris, M. & Becklin, E. E. 1998, ApJ, 509, Issue 2, 678
- [2000] Ghez, A., Morris, M., Becklin, E.E., Tanner, A. & Kremenek, T. 2000, Nature, 407, 349
- [2003] Ghez, A., Duchêne, G., Matthews, K., Hornstein, S. D., Tanner, A., Larkin, J., Morris, M., Becklin, E. E., Salim, S., Kremenek, T., Thompson, D., Soifer, B. T., Neugebauer, G., & McLean, I. 2003a, ApJ, 586, L127
- [2003] Ghez, A., Salim, S., Hornstein, S. D., Tanner, A., Morris, M., Hecklin, E. E. & Duchêne, G. 2003b, astro-ph\0306130
- [2003] Goldwurm, A.; Brion, E.; Goldoni, P.; Ferrando, P.; Daigne, F.; Decourchelle, A.; Warwick, R. S.; Predehl, P., 2003, ApJ, 584, 751G
- [2003] Gould, A., Quillen, A. C., 2003, ApJ, 592, 935
- [1995] Greenhill, L. J.; Colomer, F.; Moran, J. M.; Backer, D. C.; Danchi, W. C.; Bester, M., 1995, ApJ, 449, 365
- [2003] Gürkan et al. 2003, astro-ph/0308449
- [1987] Güsten R., Genzel R., Wright M. C. H., Jaffe D. T., Stutzki J., Harris A. I. 1987, ApJ, 317, 124
- [1991] Gwinn, C. R.; Danen, R. M.; Tran, T. Kh.; Middleditch, J.; Ozernoy, L. M., 1991, ApJ, 381, 43G
- [1996] Haller, Joseph W.; Rieke, M. J.; Rieke, G. H.; Tamblyn, P.; Close, L.; Melia, F., 1996, ApJ, 456, 194
- [2003] Hansen, B. M. S. & Milosavljević, ApJL, 593, L77
- [1993] Herbst T. M., Beckwith S. V. W., Forrest W. J. & Pipher J. L., 1993, AJ, 317, 956
- [1995] Hofmann, Reiner; Brandl, Bernhard; Eckart, Andreas; Eisenhauer, Frank; Tacconi-Garman, Lowell E., 1995, Infrared Detectors and Instrumentation for Astronomy, Albert M. Fowler; Ed., Proc. SPIE Vol. 2475, p. 192-202
- [2002] Hornstein, S. D.; Ghez, A. M.; Tanner, A.; Morris, M.; Becklin, E. E.; Wizinowich, P., 2002, ApJ, 577, pp. L9
- [2004] Horrobin, M.; Eisenhauer, F.; Tecza, M.; Thatte, N.; Genzel, R.; Abuter, R.; Iserlohe, C.; Schreiber, J.; Schegerer, A.; Lutz, D.; Ott, T.; Schödel, R., 2004, Astron. Nach., Vol.325, Issue 2, p.88-91

- [1993] Jackson, J. M., Geis, N., Genzel, R., Harris, A. I., Madden, S., Poglitsch, A., Stacey, G. J., and Townes, C. H., 1993, *ApJ*, 402, 173
- [1984] Jiang, H. X. & Lin, J. Y. 1985, *Am. J. Phys.*, 53, 694
- [1991] Kenneth, R., L., 1991, 'Astrophysical Data: Planets and Stars', Springer-Verlag
- [2003] Kim, S. S. & Morris, M., 2003, *ApJ*, 597, 312
- [1995] Kormendy, J. & Richstone, D. 1995, *Annu. Rev. Astron. Astrophys.*, 33, 581
- [2001] Kormendy, J. 2001, *Rev. Mexicana Astron. Astrofis. Ser. Conf.*, 10, 69
- [1995] Krabbe A. et al., 1995, *ApJ*, 317, L95
- [1998] Krichbaum, T. P.; Graham, D. A.; Witzel, A.; Greve, A.; Wink, J. E.; Grewing, M.; Colomer, F.; de Vicente, P.; Gomez-Gonzalez, J.; Baudry, A.; Zensus, J. A., 1998, *A&A*, 335, 106
- [1991] Lacy, J. H., Achtermann, J. M. & Serabyn, E. 1991, *ApJ*, 380, L71
- [1991] Lang R. K., 1992, *Astrophysical Data: Planets and Stars*, (Springer-Verlag)
- [1989] Leonard, P. J. T. & Merrit, D., 1989, *ApJ*; 339, 195
- [2003] Levin, Y. & Beloborodov *ApjL*, 590. L33
- [2005] Levin, Y., Wu, Al., and Thommes, E., 2005, *astro-ph/0502143*
- [1983] Lo, K. Y. & Claussen, M. J., 1983, *Natur*, 306, 645
- [1985] Lo, K. Y., 1985, *Proceedings of the ESO-IRAM-Onsala Workshop on (Sub)Millimeter Astronomy*, Aspenas, Sweden, June 17-20, 1985, 273 *sma..work..273L*
- [2004] Maillard, J. P.; Paumard, T.; Stolovy, S. R.; Rigaut, F., 2004, *A&A*, 423, 155M
- [1992] Makino, J. & Aarseth, S.J. 1992, *Proc. Astron. Soc. Japan*, 44, 141
- [2001] Makino, J. 2001, in *ASP Conf. Ser. 228: Dynamics of Star Clusters and the Milky Way*, ed. S. Deiters, B. Fuchs, R. Just, & R. Spurzem, 87
- [1998] Maoz, E. 1998, *ApJ*, 494, 181
- [2001] Melia, F. & Falcke, H. 2001, *Annu. Rev. Astron. Astrophys.* 2001, 39, 309
- [1997] Menten, Karl M.; Reid, Mark J.; Eckart, Andreas; Genzel, Reinhard, 1997, *ApJ*, 475, 111
- [1996] Mezger, P. G., Duschl, W. J. & Zylka, R. 1996, *Astron. Astrophys. Rev.*, 7, 289

- [2000] Miralda-Escudé, J. & Gould, A. 2000, ApJ, 545, Issue 2, 847
- [2000] Miyoshi, M.; Matsumoto, K.; Kamenno, S.; Takaba, H.; Iwata, T., 1994, Natur, 371, 395
- [1993] Morris, M. 1993, ApJ, 408, 496
- [1996] Morris, M. & Serabyn, E. 1996, Annu. Rev. Astron. Astrrophys. 1996, 34, 645
- [2003] Mouawad, N.; Eckart, A.; Pfalzner, S.; Straubmeier, C.; Spurzem, R.; Genzel, R.; Ott, T.; Schödel, R. (2003), Galaxies and Chaos, Edited by G. Contopoulos and N. Voglis, Lecture Notes in Physics, vol. 626, p.302-312.
- [2004] Mouawad, N., Eckart, A., Pfalzner, S., Moulataka, J., Straubmeier, C, 2004, The Dense Interstellar Medium in Galaxies, Proceedings of the 4th Cologne-Bonn-Zermatt Symposium, Zermatt, Switzerland, 22-26 September 2003. Edited by S.Pfalzner, C. Kramer, C. Staubmeier, and A. Heithausen. Springer proceedings in physics, Vol. 91
- [2004b] Mouawad, N.; Eckart, A.; Pfalzner, S.; Schödel, R.; Moulataka, J.; Spurzem, R., Astron. Nachr., Vol. 325, S1, Short Contributions Presented at the Annual Scientific Meeting of the Astronomische Gesellschaft and the Czech Astronomical Society in Prague, September 20-25, 2004., p.102
- [2005] Mouawad, N., Eckart, A., Pfalzner, S., Schödel, R., Moulataka, J., Spurzem, R., 2005, Astron. Nachr., Vol.326, Issue 2, p.83-95
- [2004] Moulataka, J.; Eckart, A.; Viehmann, T.; Mouawad, N.; Straubmeier, C.; Ott, T.; Schödel, R., 2004, A&A, v.425, p.529-542
- [2003] Muno, M. P.; Baganoff, F. K.; Bautz, M. W.; Brandt, W. N.; Garmire, G. P.; Ricker, G. R., 2003, ApJ, Volume 599, Issue 1, pp. 465-474
- [2004] Muno, M. P.; Baganoff, F. K.; Bautz, M. W.; Feigelson, E. D.; Garmire, G. P.; Morris, M. R.; Park, S.; Ricker, G. R.; Townsley, L. K., 2004, ApJ, 613, 326M
- [2002] Munyaneza, F. & Viollier, R. D. 2002, ApJ, 564, 274
- [1991] Murphy, B.W., Cohn, H.N., Durisen, R.H., 1991, ApJ 370, 60
- [1994] Najarro, F.; Hillier, D. J.; Kudritzki, R. P.; Krabbe, A.; Genzel, R.; Lutz, D.; Drapatz, S.; Geballe, T. R., 1994, A&A, 285, 573N
- [1997] Najarro, F.; Krabbe, A.; Genzel, R.; Lutz, D.; Kudritzki, R. P.; Hillier, D. J. 1997, A&A, 325, 700N
- [1999] Ott, T., Eckart, A., Genzel, R., ApJ 523, 248 (1999)
- [2003] Ott, Thomas; Genzel, Reinhard; Eckart, Andreas; Schödel, Rainer, 2003, Astron. Nachr., S 1, Proceedings of the Galactic Center Workshop 2002 - The central 300 parsecs of the Milky Way., p.543-549

- [2001] Paumard, T.; Maillard, J. P.; Morris, M.; Rigaut, F., 2001, A&A, 366, 466P
- [2003] Paumard, Thibaut, Maillard, Jean-Pierre, Stolovy, Susan, 2003, Astron. Nach., S 1, Proceedings of the Galactic Center Workshop 2002 - The central 300 parsecs of the Milky Way., p.303-307
- [2003] Porquet, D.; Predehl, P.; Aschenbach, B.; Grosso, N.; Goldwurm, A.; Goldoni, P.; Warwick, R. S.; Decourchelle, A., 2003, A&A, 407, 17P
- [2005] Pott, J.-U., Eckart, A., Glindemann, A., Viehmann, T., Schödel, R., et al. 2005 Msngr.119
- [1996] Rauch, K. P. & Tremaine, S., 1996, 1996, New A, 1, 149R
- [1999] Reid, M. J.; Readhead, A. C. S.; Vermeulen, R. C.; Treuhaft, R. N., 1999, ApJ, 524, Issue 2, pp. 816
- [2003] Reid, M. J., Menten, K. M., Genzel, R., Ott, T., Schödel, R. & Eckart, A., 2003, ApJ, 587, 208
- [1993] Reid, M. J. 1993, Annu. Rev. Astron. Astrpophys., 31, 345
- [1989] Rieke, G. H., Rieke, M. J. & Paul, A. E., 1989, ApJ, 36, 752
- [2003] Rigaut, F.; Geballe, T. R.; Roy, J.-R.; Draine, B. T., 2003, ANS, 324, 551R
- [1993] Roberts D. A. & Goss W. M., 1993, ApJS, 317, 133
- [2001] Rubilar, G. F. & Eckart 2001, A., A&A, 374, 95
- [1972] Sanders, R., H., & Lowinger, T. , 1972, Astron. J., Vol. 77, p. 292
- [2003] Scoville, N.Z., Stolovy, S.R., Rieke, M. et al: accepted to ApJ (9/1/03 issue)
- [1990] Sellgren, K.; McGinn, M. T.; Becklin, E. E.; Hall, D. N., 1990, ApJ, 359, 112S
- [1985] Serabyn, E. & Lacy 1985, J. H., ApJ, 293, 445
- [2004] Shukla, H., Yun, S.M. & Scoville, 2004, N.Z., ApJ, 616, 231
- [1997] Sigurdsson S. & Rees, M. J, 1997, MNRAS, Volume 284, Issue 2, pp. 318-326
- [1993] Smith, R. G., Sellgren, K. & Brooke, T. Y., 1993, MNRAS, 263, 749
- [2005] L. Subr & V. Karas, A& A accepted, astro-ph/0501203
- [2005] Pott et al. 2005, ESO Messenger
- [1992] Press, W. H., Flannery, B. P., Teukolsky, S. A., and Vetterling, W. T., 1992, 'Numerical recipes in C. The art of scientific computing', Cambridge: University Press

- [1975] Spitzer, L. Jr. 1975, *Dynamical Evolution of Globular Clusters*, Princeton Series in Astrophysics
- [1999] Spurzem, R. 1999, *J. Comp. Appl. Math.*, 109, 407
- [2002] Schödel, R., Ott, T., Genzel, R., Hofmann, R., Lehnert, M., Eckart, A., Mouawad, N., Alexander, T., Reid, M. J., Lenzen, R., Hartung, M., Lacombe, F., Rouan, D., Gendron, E., Rousset, G., Lagrange, A.-M., Brandner, W., Ageorges, N., Lidman, C., Moorwood, A. F. M., Spyromilio, J., Hubin, N., Menten, K. M. 2002, *Nature*, 419, 694
- [2003] Schödel, R., Ott, T., Genzel, R., Eckart, A., Mouawad, N., Alexander, T. 2003, *ApJ*, 596, 1015
- [2004] Schödel, R., 2004, PHD Thesis, Ludwig-Maximilians-Universität, München
- [1960] Sterne, Th. 1960, 'An introduction to celestial mechanics', p.44-58
- [2003] Tanner, Angelle M.; Ghez, A. M.; Morris, M.; Becklin, E. E., 2003, *ANS*, 24, 597T
- [2004] Tanner, A., M., Ghez, A., M., Morris, M., Christou, J., C., 2004, accepted by *ApJ*, astro-ph/0412494
- [1972] Weinberg, S., 1972, 'Gravitation and cosmology: Principles and applications of the general theory of relativity', New York: Wiley, c1972
- [1985] Winnberg, A.; Baud, B.; Matthews, H. E.; Habing, H. J.; Olton, F. M., 1985, *ApJ*, 291, 45
- [2000] Yusef-Zadeh, F., Melia, F., & Wardle, M. 2000, *Science*, 287, 85
- [2003] Zoccali, M., Renzini, A., Ortolani, S., Greggio, L., Saviane, I., Cassisi, S., Rejkuba, M., Barbuy, B., Rich, R. M., Bica, E., 2003, *A&A*, 399, 931Z
- [2002] Portegies Zwart, S. F.; McMillan, S. L. W., 2002, *ApJ*, 576, 899P

Acknowledgements

At the end of these exciting years of my Ph.D thesis, I would like to thank at first, my supervisor, Prof. Dr. Andreas Eckart, who offered me the opportunity to work on the dynamics at the Galactic Centre, which is one of the most competitive topics in Astronomy, and from whom I learned how solutions for problems can be simpler, if we simply, make them simpler! My first thanks are also to PD Dr. Susanne Pfalzner who introduced me to the world of numerical simulations, and who showed continuous interest in the details of my work, and who had to feel the pressure when I was confronting a new problem.

Special thanks to for Rainer Schödel for the long discussions concerning my work, and for always being ready to help whenever I asked, thanks also for the nice scientific exchange we had from München to Köln.

I thank you all again for being patient when correcting my manuscripts!

I also thank Prof. Dr. Rainer Spurzem in Ari, Heidelberg for his continuous input when it came to N-body simulations.

Many thanks to Prof. Dr. Mark Morris for the exciting discussions we had during conferences, but also via emails.

I would like to thank Jihane Moulataka not only for her scientific support and encouragement, and for having supported all my complaints, but also to have shared with me all the jokes we laughed about. chou? yalla bassita!

Lahbib, les mathématiques c'est ta spécialité, et qui d'autre aurait pu m'aider a intégrer ?, it was a pleasure having you in our group.

To Frederic and S. Jeyakumar thank you for your nice ideas and your interest in my scientific problems!

I am very grateful to Thomas Bertram and Jens Zuther, or should I say Jens Zuther and Thomas Bertram, well, I think both of them were of great help when it came to computer trouble. Thanks also for being the ones who also had to deal with my first german letters. An important fraction of german which I learned in the institute is due to the efforts of Juwe who had to speak sehr sehr langsam und sehr deutlich, aber Jetzt geht es besser, oder? I hope you will keep on doing these efforts, the poor foreigners will have they life in Germany more joyful this way.

I thank Julia for being the translator of the german administrative papers needed for the submission of this thesis and especially of the Zusammenfassung!

All my thanks to Bettina, Stephanie, Marlies, and Marrianna for all what they had to do to help me accustom with the german administration.

Definitely, thanks to all my friends in Germany and Lebanon and elsewhere for the confidence they showed in me, and the energy they gave me.

Thanks to Tuline and Nancy for keeping me informed with our local Lebanese news, and for

Dany, Tony and Hayla for sharing with me their music.

A very big thanks goes to Bhupendra, who lived with me all the troubles, and difficulties and who was always there to cheer me up, and with whom working in the nights became softer, thanks for being there when I needed you. Sorry when the 10 mins became longer and longer.

Finally, I am very thankful and grateful to my parents and all the members of my family in Lebanon who were always there to help. Thanks to Johnny, Dolly and Jihad without whom it wouldn't have been possible to be here. Sorry for making you suffer the distance between us and thank you for not growing much older during my absence! nchalla bchoufkon 3an 'arib. Bechkorkon jami3an 3al hobb yalleh 3atyouneh wel hamm yalleh hmeltouh ma3eh.

Erklärung

Ich versichere, daß ich die von mir vorgelegte Dissertation selbständig angefertigt, die benutzten Quellen und Hilfsmittel vollständig angegeben und die Stellen der Arbeit - einschließlich Tabellen, Karten und Abbildungen -, die anderen Werken im Wortlaut oder dem Sinn nach entnommen sind, in jedem Einzelfall als Entlehnung kenntlich gemacht habe; daß diese Dissertation noch keiner anderen Fakultät oder Universität zur Prüfung vorgelegen hat; daß sie - abgesehen von unten angegebenen Teilpublikationen - noch nicht veröffentlicht worden ist sowie, daß ich eine solche Veröffentlichung vor Abschluß des Promotionsverfahrens nicht vornehmen werde. Die Bestimmungen dieser Promotionsordnung sind mir bekannt. Die von mir vorgelegte Dissertation ist von Herrn Prof. Dr. Andreas Eckart betreut worden.

Teilpublikationen

Liste der Referierten Veröffentlichung

- **Mouawad, N.**; Eckart, A.; Pfalzner, S.; Schödel, R.; Moultaqa, J.; Spurzem, R. (2005). 'Weighing the cusp at the Galactic Centre'. *Astron. Nachr. / AN* 326, No. 2, 83-95.
- Moultaqa, J.; Eckart, A.; Viehmann, T.; **Mouawad, N.**; Straubmeier, C.; Ott, T.; Schödel, R. (2004). 'Dust embedded sources at the Galactic Center. 2 to 4 μm imaging and spectroscopy in the central parsec'. *Astronomy and Astrophysics*, v.425, p.529-542.
- Eckart, A.; Moultaqa, J.; Viehmann, T.; Straubmeier, C.; **Mouawad, N.** (2004). 'Young Stars at the Center of the Milky Way?'. *The Astrophysical Journal*, Volume 602, Issue 2, pp. 760-769.
- Schödel, R.; Ott, T.; Genzel, R.; Eckart, A.; **Mouawad, N.**; Alexander, T. (2003). 'Stellar Dynamics in the Central Arcsecond of Our Galaxy'. *The Astrophysical Journal*, Volume 596, Issue 2, pp. 1015-1034.
- Schödel, R.; Ott, T.; Genzel, R.; Hofmann, R.; Lehnert, M.; Eckart, A.; **Mouawad, N.**; Alexander, T.; Reid, M.J.; Lenzen, R.; Hartung, M.; Lacombe, F.; Rouan, D.; Gendron, E.; Rousset, G.; Lagrange, A.-M.; Brandner, W.; Ageorges, N.; Lidman, C.; Moorwood, A.F.M.; Spyromilio, J.; Hubin, N.; Menten, K.M. (2002). 'A star in a 15.2-year orbit around the supermassive black hole at the centre of the Milky Way'. *Nature*, Volume 419, Issue 6908, pp. 694-696 (2002).

Liste der nicht-Referierten Veröffentlichung

- **Mouawad, N.**; Eckart, A.; Pfalzner, S.; Moultaqa, J.; Straubmeier, C. (2004). 'Non-Keplerian Orbits of the Star S2 Around the Black Hole at the Galactic Center'. *Proceedings of the 4th Cologne-Bonn-Zermatt-Symposium 'The Dense Interstellar Medium in Galaxies'*, Edited by Pfalzner, S.; Kramer, C.; Straubmeier, C.; Heithausen, A., Springer Proceedings in Physics, vol. 91, p.287-290.

- **Mouawad, N.;** Eckart, A.; Pfalzner, S.; Schödel, R.; Moultaqa, J.; Spurzem, R., 'Weighing the Cusp at the Galactic Centre', *Astronomische Nachrichten*, Vol. 325, Supplement 1, Short Contributions Presented at the Annual Scientific Meeting of the Astronomische Gesellschaft and the Czech Astronomical Society in Prague, September 20-25, 2004., p.102
- **Mouawad, N.;** Eckart, A.; Pfalzner, S.; Moultaqa, J.; Straubmeier, C.; Spurzem, R.; Schödel, R.; Ott, T. (2003). 'Stellar Orbits at the Center of the Milky Way'. *Astronomische Nachrichten*, Supplementary Issue 1, Proceedings of the Galactic Center Workshop 2002 - The central 300 parsecs of the Milky Way., p.315-319.
- Moultaqa, J.; Eckart, A.; Viehman, T.; **Mouawad, N.;** Straubmeier, C.; Ott, T., 'Dust Embedded Sources at the Galactic Center: MIR spectroscopy and imaging in the central parsec', SF2A-2003: Semaine de l'Astrophysique Française, meeting held in Bordeaux, France, June 16-20, 2003. Eds.: F. Combes, D. Barret, T. Contini, and L. Pagani. *EdP-Sciences, Conference Series*, p. 271.
- Eckart, A.; Bertram, T.; **Mouawad, N.;** Viehmann, T.; Straubmeier, C.; Zuther, J., 'Long Range Science Perspectives for the VLTI', 2003, *Astrophysics and Space Science*, v. 286, Issue 1, p. 269-276.
- **Mouawad, N.;** Eckart, A.; Pfalzner, S.; Straubmeier, C.; Spurzem, R.; Genzel, R.; Ott, T.; Schödel, R. (2003). 'Stars Close to the Massive Black Hole at the Center of the Milky Way'. *Galaxies and Chaos*, Edited by G. Contopoulos and N. Voglis, *Lecture Notes in Physics*, vol. 626, p.302-312.
- Eckart, A.; **Mouawad, N.;** Krips, M.; Straubmeier, C.; Bertram T. (2002). 'Scientific potential for interferometric observations of the Galactic Center'. *Future Research Direction and Visions for Astronomy*. Edited by Dressler, Alan M. *Proceedings of the SPIE*, Volume 4835, pp. 12-21.

Lebenslauf

Persönliche Angabe

Name	Mouawad
Vorname	Nelly
Geburtsdatum	21. March 1978
Geburtsort	Jbeil, Libanon
Familienstand	ledig
Staatsangehörigkeit	libanesin

Schulausbildung

1981-1989	Collège de la Sainte Famille, Fanar, Libanon
1988-1995	Collège de la Sagesse, Achrafieh, Beirut, Libanon
1995	Baccalauréat

Hochschulausbildung

1996-2000	Naturwissenschaft Fakultät, University Libanaise, Fanar, Libanon
2000-2001	Université Paul Sabatier, Toulouse III, Toulouse, Frankreich
seit 2002	Doktorarbeit (I. Physikalisches Institut der Universität zu Köln) <i>Dissertation Thema: Mass Distribution at the Galactic Centre</i>

Anstellungen

2002 - 03/2005	Wissenschaftliche Mitarbeiterin (I. Physikalisches Institut der Universität Köln)
04/2005 - 06/2005	Short-term Scholar (IPAM Institut, Los Angeles, U.S.A.)

Sprachen

- Arabisch (Mutterschprache)
- Englisch (fließend in Wort und Schrift)
- Französisch (fließend in Wort und Schrift)
- Deutsch (Gute Erkenntnisse)